SYNTHESIS AND CHARACTERIZATION OF PRISTINE AND DOPED NANOCRYSTALLINE $BaWO_4$

Thesis submitted to

Mahatma Gandhi University, Kottayam

in partial fulfilment of the requirements for the award of the degree of

DOCTOR OF PHILOSOPHY IN PHYSICS

Under the Faculty of Science

by

SEENAMOL K STEPHEN

Under the supervision of

Dr. THOMAS VARGHESE

Department of Physics
Newman College, Thodupuzha

October 2021

MAHATMA GANDHI UNIVERSITY

CERTIFICATE ON PLAGIARISM CHECK

1.	Name of the Research Scholar	**SEENAMOL K STEPHEN**
2.	Title of the Thesis/Dissertation	Synthesis and Characterization of Pristine and Doped Nanocrystalline $BaWO_4$
3.	Name of the Supervisor(s)	Dr. Thomas Varghese
4.	Department/Institution/ Research Centre	Department of Physics, Newman College, Thodupuzha
5.	Similar Content (%) identified	**4% (Four)**
6.	Acceptable Maximum Limit	25%
7.	Software Used	Urkund
8.	Date of Verification	20-10-2021

**Report on plagiarism check, items with % of similarity is attached*

Checked by (with Name, Designation & Signature)

20-10-2021

Mini. G Pillai
20/10/2021

MINI G. PILLAI
Deputy Librarian-in-charge
Mahatma Gandhi University Library
P. D. Hills P.O., Kottayam - 686 560

Name & Signature of the Researcher : Seenamol K Stephen

Name & Signature of the Supervisor(s) : Dr. Thomas Varghese

Dr. THOMAS VARGHESE
RESEARCH GUIDE
DEPT. OF PHYSICS
NEWMAN COLLEGE
THODUPUZHA-685585

Name & Signature of the HoD/ HoI (Chairperson of the Doctoral Committee) :

DR. THOMSON JOSEPH
PRINCIPAL-IN-CHARGE
NEWMAN COLLEGE
THODUPUZHA

NEWMAN COLLEGE * THODUPUZHA, KERALA-685585 *

Curiginal

Document Information

Analyzed document	SEENAMOL K STEPHEN-SYNTHESIS AND CHARACTERIZATION OF PRISTINE AND DOPED NANOCRYSTALLINE BaWO4.pdf (D115800733)
Submitted	2021-10-20 07:34:00
Submitted by	Smt. Mini G. Pillai
Submitter email	library@mgu.ac.in
Similarity	4%
Analysis address	library.mgu@analysis.urkund.com

Sources included in the report

W	URL: https://www.researchgate.net/publication/299546002_Synthesis_and_morphological_transformation_of_BaWO4_crystals_Experimental_and_theoretical_Insigths Fetched: 2021-10-20 07:35:00	6
W	URL: https://www.researchgate.net/publication/344170705_Dielectric_studies_of_BaWO_4_nanoparticles_Dielectric_Studies_of_BaWO_4_Nanoparticles Fetched: 2021-10-20 07:35:00	22
W	URL: http://docplayer.net/149811914-First-order-character-of-the-displacive-structural-transition-in-bawo-4.html Fetched: 2021-10-20 07:35:00	4
W	URL: https://www.researchgate.net/publication/331308515_Synthesis_and_properties_of_BaWO4_nanocrystals_prepared_using_a_reverse_microemulsion_method Fetched: 2021-10-20 07:35:00	1
W	URL: https://link.springer.com/article/10.1039/c2pp25184a Fetched: 2021-10-20 07:35:00	3
W	URL: https://www.hindawi.com/journals/acmp/2013/409620/ Fetched: 2021-10-20 07:35:00	17
W	URL: https://en.wikipedia.org/wiki/Barium_tungstate Fetched: 2021-10-20 07:35:00	1

20-10-2021

Mini G Pilla
20/10/2021

MINI G. PILLAI
Deputy Librarian-in-charge
Mahatma Gandhi University Library
P. D. Hills P.O., Kottayam - 686 560

NEWMAN COLLEGE
Thodupuzha, Affiliated to MG university
Reaccredited with 'A' grade by NAAC

Idukki District, Kerala- 685 585
Ph :- 04862-222686, 229797

Dr. Thomas Varghese
Research guide

Email: nanoncm@gmail.com

Certificate

This is to certify that the thesis entitled **SYNTHESIS AND CHARACTERIZATION OF PRISTINE AND DOPED NANOCRYSTALLINE $BaWO_4$** *is an authentic record of the original research work carried out by* ***Ms. Seenamol K Stephen****, at the Research Department of Physics, Newman College, Thodupuzha, under my guidance in partial fulfilment of the requirements for the award of the degree of Doctor of Philosophy, under the faculty of Science of Mahatma Gandhi University, Kottayam. The work presented in this thesis has not been submitted for any other degree or diploma elsewhere. It is also certified that* ***Ms. Seenamol K Stephen*** *has fulfilled the course requirements for the Ph.D degree of the university.*

Thodupuzha
21st *October 2021*

Dr. Thomas Varghese
(Supervising Teacher)

Dr. THOMAS VARGHESE
RESEARCH GUIDE
DEPT. OF PHYSICS
NEWMAN COLLEGE
THODUPUZHA-685585

Declaration

I hereby declare that the Ph.D. thesis entitled "**Synthesis and characterization of pristine and doped nanocrystalline $BaWO_4$**" is a bonafide record of the original research work carried out by me under the supervision of Dr. Thomas Varghese, at the Department of Physics, Newman College, Thodupuzha, Kerala. This work is original and has not been submitted elsewhere as a whole or in part for the award of a degree/diploma. In keeping with the general practice of reporting scientific observations, due acknowledgement has been made wherever the work described is based on the findings of other investigators.

Thodupuzha

29th October 2021

Seenamol K Stephen

Acknowledgement

As catalysts reinforce chemical reactions there are many who added momentum to my humble efforts towards the accomplishment of my great goal. A bouquet of great gratitude is offered to those who have played remarkable roles in the fulfilment of this thesis. First and foremost, let me extend a heart of sincere gratitude to God Almighty for all the blessings bestowed upon me even at the time of stress and strain.

A profound sense of gratitude binds me to my research supervisor Dr. Thomas Varghese for his efficient guidance and continuous support during my research phase without which this mission would not have been accomplished.

I wish to acknowledge the Principal and faculty members of the Department of Physics, with a special mention to Dr. Joe Jacob, Research Coordinator and former Head of the Department of Physics and Dr. Aloysius Sabu, Head of the Department of Physics for all the supports rendered. I would like to thank the Principal and faculty members of the Department of Physics, Nirmala College, Muvattupuzha for all the facilities provided to me to fulfill my research work.

From the depth of my heart, I express my sincere gratitude to Dr. Mercy Joseph, the Principal, Dr. N Shaji, former Principal and to my colleagues Sri. Tojomon Mathew, Dr. Bindu G Nair, Dr. Sudakshina B, Dr. Sheeja T K, Dr. Babitha Mathews and other members of the staff at T. M. Jacob Memorial Government College, Manimalakunnu, Koothattukulam for all the encouragement and support given to me during my research.

I acknowledge SAIF, Kochi, SAIF, M.G University, Department of Physics, M. G. University, Department of Physics, Mangalore University, IIT Madras and Maharajas College, Ernakulam for various experimental measurements.

I am indebted to my fellow research scholars Dr. Aloysius Sabu, Dr. Priyanka K P, Dr. Sheena P A, Dr. Sreedevi A, Dr. Babitha K K, Francis Xavier P A, Hitha H, Anjali Jose, Soumya Kuriakose, and Mathew for their help, cooperation and friendship. A good round of applause is to be given to Mr. Muhammed, former student of Nirmala College, Muvattupuzha for his valuable support and cooperation

I owe my special thanks to my friend Mr. Suresh Mathew and my brother in law Mr. Mathews George for the timely help and support offered to me. Let me

appreciate the great moral support and motivation offered by my friends and neighbours for making me fortunate enough to reach my destination.

Let me express my deep sense of gratitude to my parents for their unconditional love, encouragement and support given to me during my entire life. I would like to acknowledge my siblings and other members of my family for their love and support during the crucial phase of my life. I am deeply indebted to my husband Mr. Sony Joseph and children Jophan and Ann Maria for their immense understanding and support during the period of research that helped me to complete this venture successfully. Last but not the least, let me convey my hearty gratitude to all who have dedicated themselves by contributing much towards the successful completion of my thesis.

Seenamol K Stephen

Contents

Chapter- 3

Chapter- 4

Chapter- 5

Chapter- 6

Chapter -7

PREFACE

Metal tungstates with the formula MWO_4 have attracted much attention due to their interesting structural and photoluminescence properties. These materials have found applications in scintillation counters, lasers and optical fibres . Some of the divalent transition metal tungstates have gained commercial interest in lasers and fluorescent lamps, while some others are of special importance due to their electrical conductivity and magnetic properties. In addition, these materials also find applications as catalysts and humidity sensors. Barium tungstate ($BaWO_4$) is the heaviest member of the family of the alkaline earth tungstates. Like many other ABX_4 type compounds, $BaWO_4$ crystallizes at ambient conditions in the tetragonal scheelite type structure. The $BaWO_4$ is to be extensively investigated because of its good electrical conductivity, magnetic and photoluminescence properties. As one of the most reactive alkaline earth tungstates, $BaWO_4$ based materials can play an important role in a wide variety of technological applications, such as light-emitting diodes, humidity sensors, optic filters, scintillator detectors, photocatalysts, microwave dielectrics, phosphors, and solid-state lasers.

Several studies have been reported on the synthesis and characterization of nanocrystalline $BaWO_4$. The large bandgap of $BaWO_4$ has restricted its application in diverse fields. Hence, tailoring of the bandgap is essential for modifying the properties of $BaWO_4$ for optoelectronic device applications. Literature survey indicated that the bandgap of several nanocrystalline samples can be tuned by

electron beam irradiation and by doping with suitable dopants. However, there are no reports on the effect of electron beam irradiation on the structural and optical properties of the $BaWO_4$. Furthermore, there are no reports on the effect of copper doping on the structural, optical, and magnetic properties of $BaWO_4$. Literature reports that doping with ytterbium will yield NIR photoluminescence, which has wide application. However, reports on the influence of ytterbium on the structural, optical, and magnetic properties of $BaWO_4$ are sparse. Hence, more extensive and systematic studies of pristine and doped nanocrystalline $BaWO_4$ is needed. The present study mainly focuses on the synthesis and characterization of nanocrystalline $BaWO_4$, Cu doped $BaWO_4$, and Yb doped $BaWO_4$. In addition, the effect of 8 MeV electron beam irradiation on the structural and optical properties of $BaWO_4$ is also investigated.

Structural, optical, magnetic and electrical properties of chemically synthesized nanocrystalline $BaWO_4$ samples are analysed. The effect of calcination temperature on different properties is also studied. The average crystallite sizes, surface morphology and optical bandgap values of the samples are found to change with calcination temperature. Copper and ytterbium-doped $BaWO_4$ samples are synthesized by the chemical precipitation method. Modification of the structural, optical and magnetic properties of $BaWO_4$ by doping with copper and ytterbium are also investigated. NIR photoluminescence emission is achieved with ytterbium doping. Effect of 8 MeV electron beam irradiation on the structural and optical properties of nanocrystalline $BaWO_4$ is also studied.

The work presented in this thesis comprises the analysis of the properties of pristine and doped barium tungstate. Along with that, the effect of 8 MeV electron beam irradiation on the structural and optical properties of the $BaWO_4$ sample is also studied. The research work is systematically presented in seven chapters. The structure and fundamental properties of $BaWO_4$, and a brief review on the synthesis and properties of pristine and doped $BaWO_4$ are presented in Chapter 1. Chapter 2 deals with a brief description of various characterization techniques used for the characterization of the prepared samples. The effect of calcination temperature on the structural, optical, magnetic and electrical properties of nanocrystalline $BaWO_4$ is described in Chapter 3. The modifications of the structural, optical, and magnetic properties of the $BaWO_4$ samples due to Cu and Yb doping are elucidated in Chapters 4 and 5, respectively. Chapter 6 gives a detailed discussion of the impact of 8 MeV electron beam irradiation on the structural and optical properties of nanocrystalline $BaWO_4$. The conclusions drawn based on systematic analysis are summarized in Chapter 7 and the scope for future work in this field is indicated at the end of this chapter.

Most of the results and discussion have been published/communicated in peer reviewed national/international journals.

PUBLICATIONS

1. Effect of Yb^{3+} substitution on the structural and optical properties of $Ba_{1-x}Yb_xWO_4$ nanoparticles-NIR luminescence emissions for optical communication and bioanalyses, **Seenamol K Stephen**, Thomas Varghese, **Materials Characterization** (Elsevier) 174 (2021) 110985.
2. Modifications of structural and optical properties of nanophase $BaWO_4$ phosphors: Dose dependent effect of high energy electron beam irradiation, **Seenamol K Stephen**, S Ganesh, Thomas Varghese, **Radiation Physics and Chemistry** (Elsevier) 180 (2021) 109317.
3. Structural modifications and extended spectral response of nanocrystalline $Ba_{1-x}Cu_xWO_4$ samples, **Seenamol K Stephen**, Thomas Varghese, **Materials Chemistry and Physics** (Elsevier) 258 (2021) 123901.
4. Effect of calcination on the structural, optical and magnetic properties of $BaWO_4$ nanoparticles synthesized by chemical precipitation, **Seenamol K Stephen**, Aloysius Sabu N, Priyanka K P, Thomas Varghese, **Indian Journal of Pure and Applied Physics**, 57 (2019) 14-22.
5. Dielectric studies of $BaWO_4$ nanoparticles, **Seenamol K Stephen**, C Viji, Thomas Varghese, **AIP Conference Proceedings** 2263 (2020) 060012.

PRESENTATIONS

1. "Temperature dependent dielectric and ac conductivity of nanocrystalline $BaWO_4$" **Seenamol K Stephen** and Thomas Varghese, 6th International Conference on "Nanoscience and Nanotechnology", **(ICONN 2021)**, SRM institute of Science and Technology, India, 01 – 03 February 2021.

2. "Dielectric studies of $BaWO_4$ nanoparticles", **Seenamol K Stephen** and Thomas Varghese, Rusa sponsored International Conference on "Science and Technology of Advanced Materials" (STAM20), Marathanasius College, Kothamangalam, 14 – 16 January 2020.

3. "Synthesis and characterization of $BaWO_4$ nanoparticles", **Seenamol K Stephen** and Thomas Varghese, UGC sponsored National Seminar on "Recent Trends in Nano and other Materials for Energy Efficient Devices", St. Alosius College, Edathua, 20 – 22 July 2017.

List of Tables

List of Figures

Chapter 1

INTRODUCTION AND LITERATURE REVIEW

The structure and fundamental properties of $BaWO_4$ are discussed in this chapter. Following this, a detailed review of the studies done so far on pristine and doped $BaWO_4$ is presented. The objectives and relevance of the present investigation are also summarized.

1.1 Introduction

Nanotechnology has emerged as a developing technology of the 21st century. Nanoscience and nanotechnology involve studying and working with matter on an ultra small scale. Nanoscience is a new way of thinking about building up complex materials and devices by exquisite control of the functionality of matter and its assembly at the nanometer length scale. It builds up the ability to control or manipulate the size of the particle at the atomic scale. At the nano dimension, the interactions and physics between atoms display exotic properties that they don't have at larger scales. When the particle size or the grain size in the solid matter is reduced to nanometer ranges, every property of matter shows some change enabling unique application. For instance, opaque substances become transparent, inert materials become catalysts, stable materials turn combustible solids and insulators become conductors.

The properties of nanocrystals vary with their composition, structure, phase, shape, size, and size distribution. Furthermore, the architectural control of nanosized materials with well-defined shapes is important for the success of "bottom-up" approaches towards future nanodevices [1–3]. During the past decade, inorganic nanoparticles with controllable and uniform size and shape have attracted vast attention because of their unique size and shape-dependent properties and great potential applications [4–13]. In short, control of the morphology of the nanoparticles is one of the focuses on the development of nano-techniques [10,11]. A variety of synthetic methods have also been developed for the controlled synthesis of polyhedral [14–20].

Metal oxide nanoparticles have been studied due to their novel optical, electronic, magnetic and thermal properties and their potential application as catalysts, gas sensors and photoelectronic devices. Metal tungstate nanoparticles have very interesting luminescence and structural properties. Barium tungstate ($BaWO_4$) is the heaviest member of the family of the alkaline earth tungstates. Like many other ABX_4 type compounds, $BaWO_4$ crystallizes at ambient conditions in the tetragonal scheelite type structure. The $BaWO_4$ is to be extensively investigated because of its good electrical conductivity, magnetic and photoluminescence properties [21,22]. As one of the most reactive alkaline earth tungstates, $BaWO_4$ based materials can play an important role in a wide variety of technological applications, such as light-emitting diodes, humidity sensors, optic filters, scintillator detectors, photocatalysts, microwave dielectrics, phosphors, and solid-state lasers [23,24].

This work reports the study of structural, optical, electrical, and magnetic properties of nanocrystalline barium tungstate ($BaWO_4$) synthesized by the chemical precipitation method. The effect of calcination temperatures and the

influence of 8 MeV electron beam irradiation on the properties of the synthesized $BaWO_4$ nanoparticles is also investigated. The effects of copper and ytterbium doping on the structural, optical, and magnetic properties of $BaWO_4$ are also dealt with.

1.2 Nanocrystalline $BaWO_4$

Metal tungstates with the formula MWO_4 have attracted much attention due to their interesting structural and photoluminescence properties [25–29]. These materials have found applications in scintillation counters, lasers and optical fibers [30,31]. Some of the divalent transition metal tungstates have gained commercial interest in lasers and fluorescent lamps, while some others are of special importance due to their electrical conductivity and magnetic properties. In addition, these materials also find applications as catalysts and humidity sensors [32,33]. In the MWO_4 compounds, if M^{2+} has a small ionic radius < 0.77 Å (Ni = 0.69), it will belong to the wolframite-type monoclinic structure, where the tungsten atom adopts overall six-fold coordination [34]. However, in larger bivalent cations with ionic radius > 0.99 Å (Ba=1.35), they exist in the so-called scheelite-type tetragonal structure, where the tungsten atom adopts tetrahedral coordination [35].

$BaWO_4$ crystallizes into a tetragonal scheelite structure with a space group $I4_1/a$. In the $BaWO_4$ unit cell, the Ba and W atoms have an S_4 point symmetry where the tungsten atoms are coordinated to four oxygen atoms in a tetrahedral configuration. The oxygen coordination polyhedra are slightly distorted, presenting different bonding angles (108.56º and 111.30º) between O–W–O. The barium atoms are coordinated to eight oxygen atoms localized in the corners of the tetragonal unit cell forming BaO_8 polyhedrons, and hence the site symmetry is

D_{2d} [36,37]. The site symmetries of Ba and W atoms are S_4 and T_d symmetry and the O atoms occupy the C_1 sites [38]. The crystal structure is highly ionic for the Ba^{2+} cations and tetrahedral WO_4^{2-} anions [39]. The crystal structure of tetragonal $BaWO_4$ is shown in Figure 1.1.

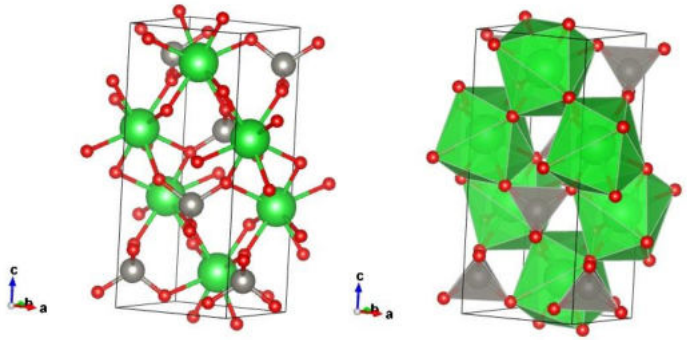

Figure 1.1 Crystal structure of tetragonal $BaWO_4$

Fundamental parameters of barium tungstate [40,41] is listed Table 1.1

Table 1.1 Fundamental properties of $BaWO_4$

Property	**Value**
Crystal system	Tetragonal
Appearance	White
Space group	$I4_1/a$
Lattice constant a	5.614 Å
Lattice constant b	12.715 Å
Density	5.04 gcm^{-3}(25 ºC), 7.26 gcm^{-3} [42]
Molecular weight	385.16 $g\text{-}mol^{-1}$
Melting point	1502 ºC [43]
Optical bandgap	5.6 eV
Dielectric constant	9 [44]

1.3. Literature Survey

MWO_4 type oxides with scheelite structure where M = Ca, Sr, Ba, Pb, and Cd have been reported to be useful for laser host materials [45], scintillators [46], oxide ion conductors [47,48], and as humidity sensors [49]. $BaWO_4$ nanoparticles were synthesized by several methods like solid-state method [50,51], co-precipitation [52], chemical precipitation [53][54], solvothermal [55], sol-gel, reverse micellar reactions [56], microwave hydrothermal [39,57,58], cyclic microwave irradiation [59], sucrose template method [35], sonochemical method [60,61], combustion [62], hydrothermal [63] and reverse microemulsion [64]. Among these methods, the solution-based chemical synthetic methods play a crucial role in the design and production of fine materials and have been successful in overcoming many of the limitations of the traditional solid-state, high-temperature methods. It can also eliminate major problems such as long diffusion paths, impurities, and agglomeration which will result in products with improved homogeneity. The chemical precipitation method is employed in this work since it is comparatively simple, less expensive and no need for any complicated equipment.

Literature reports the use of different salts such as $BaCl_2$, $Ba(NO_3)_2$, Na_2WO_4, $BaCO_3$, WO_3, etc. as precursors for the synthesis of nanocrystalline $BaWO_4$ [65–68]. The synthesis method, reaction temperature, concentration of the precursors, pH of the solution, and reaction time are the major factors influencing the particle size and morphology of the nanoparticles [66,69–71]. Liu *et al.* reported that hydrothermal treating time and surfactant concentration influence the surface morphology of the $BaWO_4$ microstructures synthesized via microemulsion mediated by the hydrothermal procedure [72]. In 2005, Zhang *et al.* synthesized bundle-like nanorod arrays of 1 − 2 μm in length and 200 − 300 nm in width, and

each nanorod has a diameter of 15 nm by solvothermal method [55]. The synthesis of penniform $BaWO_4$ nanostructures made of nanowires or nanobelts under the direction of a block copolymer in catanionic reverse micelles was reported by Shi *et al*. [65]. Zhao *et al*. fabricated various $BaWO_4$ hollow structures, including spheres, peanuts, and ellipsoids, by a precipitation reaction between $BaCl_2$ and Na_2WO_4 solutions in the presence of polymethacrylic acid (PMAA) [66]. $BaWO_4$ nanodots were synthesized by Hernandez-Sanchez *et al.* through the solution precipitation route by controlling the temperature [69]. Cavalcante *et al*. reported the synthesis of $BaWO_4$ powder with octahedral-like morphology by the co-precipitation method and processed in a domestic microwave-hydrothermal (MH) at 413 K for different times [52]. Kwan *et al*. obtained novel nanorod superstructures of $BaWO_4$ using a reversed micelle templating method [56]. Zhang *et al.* synthesized fishbone-like nanostructures by solution growth route in w/o microemulsions [73]. They found that the water content has a large influence on the size of the product, and the molar ratio between cations and anions plays an important role in the morphology of the product. The synthesis of $BaWO_4$ crystals with different morphologies such as nanosheets, nanobelts, flowerlike, quandrangled plates, and sheaves of dendrites by the facile microwave-assisted method was reported in the literature [23]. The morphologies of the samples were tuned by varying the reaction parameters, such as the concentration of PVP aqueous solutions, pH value of the starting solution, and the molar ratio of $[Ba^{2+}]/[WO_4^{2-}]$.

The crystallite size and surface morphology of the samples can be controlled by using different surfactants. Xie *et al.* successfully synthesized $BaWO_4$ crystals with different morphologies such as olive-like, flake-like, and whisker-like structure by hydrothermal route in the presence of different

surfactants [63]. Dumb bell-like $BaWO_4$ microstructures were grown by Zhang *et al.* through a surfactant-free hydrothermal route using glycerol as a co-solvent with water and as a capping agent [63]. Talebi *et al*. studied the use of different surfactants and capping agents for controlling the morphology and size of $BaWO_4$ nanoparticles [74]. The molar ratio of water to surfactant and reactant concentration has influenced the surface morphology and size of the $BaWO_4$ nanocrystals synthesized using a reverse microemulsion method [64]. The porous nature of the $BaWO_4$ powder obtained by the sucrose solution evaporation method was studied by Zawawi *et al.* [75].

Oliveira *et al*. introduced a theoretical model based on the Wulff construction that explains the possible crystal morphologies by tuning their surface chemistry, which is related to the relative stability of the faceted crystals. Both the experimental and theoretical data revealed the presence of (112), (001), and (100) facets with low values of surface energy in the $BaWO_4$ crystals [54].

There are several reports on the effect of calcination temperature on the properties of $BaWO_4$ nanoparticles synthesized by different methods. Lim *et al.* investigated changes in surface morphology and PL emission intensity of the $BaWO_4$ powders synthesized by solid-state metathetic route with the increase in calcination temperature [76]. Anicete-Santos *et al*. reported structural changes and PL emission intensity variations of the $BaWO_4$ powder upon calcination treatment [58]. An increase in particle size and PL intensity along with a change in surface morphology for the $BaWO_4$ nanoparticles prepared by the chemical precipitation method was reported by Sadiq *et al.* [53].

At normal temperature and pressure, $BaWO_4$ has a tetragonal scheelite type structure whereas on applying high pressure and temperature, it changes to

monoclinic. The monoclinic $BaWO_4$ formed at high pressure and temperature has no direct resemblance either to the scheelite or to the wolframite type [42]. Kawada *et al.* reported that in monoclinic $BaWO_4$, barium atoms are located between the densely packed two-dimensional network of WO_6 octahedra, which are connected by an edge and corner-sharing. The coordination number of the barium atoms has increased in comparison with the structure under ordinary conditions. Lacomba-Perales *et al*. observed the transition from scheelite to the $BaWO_4$-II phase (monoclinic) at a pressure of 5 GPa and at a temperature of 621 K [77]. The structural modification of $BaWO_4$ crystals synthesized by the solid-state method from tetragonal scheelite type to monoclinic fergusonite type above a pressure of 7 GPa was reported by Tan Da-Yong *et al*. [78]. They observed a continuous change in the axial parameter and pressure. They further showed that the first-order character of this phase transition stems from a coupling of large compression of soft BaO_8 polyhedrons to the small displacive distortion of rigid WO_4 tetrahedrons. Such a coupling will provide an insight into the understanding of the scheelite to fergusonite transition in other scheelite structured compounds like the molybdates, germinates and silicates. Gomis *et al.* also studied the transition of $BaWO_4$ single crystal, grown by the Czochralski method from its low-pressure tetragonal structure into a much denser monoclinic structure. Rietveld refinements of the crystal structure of the low and high-pressure phases from the quasi- hydrostatic experiments have been done by GSAS software [79].

Zhang *et al*. studied the chemical and bonding environment of the $BaWO_4$ using XPS spectra. The peaks obtained in the region at 780.2 eV (Ba $3d_{5/2}$) and 795.6 eV (Ba $3d_{3/2}$) corresponding to the Ba 3d binding energy, indicate that Ba exists in the Ba^{2+} state. The peaks at 35.6 and 37.8 eV corresponding to the W 4f state indicate that W is in its $[WO_4]^{2-}$ (W^{6+}) state. A strong oxygen 1s peak at

531.0 eV corresponds to the oxygen in its O^{2-} oxidation state was also obtained [63].

The optical properties of the $BaWO_4$ depend on the synthesis route and the degree of distortion of the crystal lattice [80]. $BaWO_4$ possesses a single absorption band corresponding to the ligand to the metal charge transfer in the region 218 − 274 nm with a band maxima occurring at 220 − 250 nm. The exact location of the maximum depends on the degree of distortion of the crystal lattice [81]. By absorbing the ultraviolet radiation, the excitation from O_{2p} to W_{t2g} in the $(WO_4)^{2-}$ group takes place [35]. Literature reports that $BaWO_4$ is a direct bandgap semiconductor, and the barium has no significant effect on the bandgap of the $BaWO_4$ sample [82]. The $BaWO_4$ has a broad blue luminescence emission due to the radiative transition of self-trapped excitons within the $(WO_4)^{2-}$ tetrahedral group [83]. Nikl *et al*. observed the excitonic luminescence of $BaWO_4$ in a wide temperature range and made the conclusions that (i) emission occurs from the lower-lying triplet state split by Jahn-Teller (JT) interaction, (ii) both triplet states affected by JT interaction give the contribution to observed emission and (iii) emission from one or both triplet states is moreover, affected by the presence of the low-symmetry local fields because the symmetry of the emitting centre is not perfectly tetrahedral [84]. Pontes *et al*. measured an optical bandgap of 5.78 eV for the $BaWO_4$ thin films fabricated by the polymeric precursor method [85]. The existence of two broad bands, one band in the blue region (around 450 nm) and another one in the green region (520−530 nm) in the photoluminescence (PL) emission of $BaWO_4$ was reported by Blistanov *et al*. [86]. According to Zhang *et al*. the exact position of the PL emission peak in $BaWO_4$ film depends on the film-forming effect and the size of the nanoparticles [21]. Lima *et al*. reported that the optical bandgap of $BaWO_4$ powders structurally disordered by high-energy

mechanical milling varied between 5.76 − 5.23 eV depending on milling time. They observed a broad PL emission in the range 500−800 nm, the intensity of which depends on the milling time. Hence they concluded that structural disorder in the lattice is an important condition to generate an intense and broad PL emission [87]. Lacomba-Perales *et al.* obtained an optical bandgap of 5.26 eV for $BaWO_4$ single crystal [88]. The bandgap of the $BaWO_4$ sample synthesized via the solid-state metathetic approach assisted by microwave energy by Parhi *et al*. is 4.8 ± 0.2 eV [89]. An increase in bandgap with calcination temperature (5.77 − 5.88 eV) for the $BaWO_4$ powder obtained through the chemical precipitation method was reported by Sadiq *et al*. [53]. However, Khademolhoseini *et al*. obtained a bandgap of 3.2 eV for the $BaWO_4$ nanoparticles prepared via a sonochemical route [61].

Tyagi *et al*. investigated the photoluminescence of $BaWO_4$ single crystals grown by the Czochralski technique in the temperature range of 77 – 300 K. A UV emission band was observed at room temperature, which completely quenched on vacuum annealing. The blue emission corresponding to the radiative transitions within the $(WO_4)^{2-}$ existed for all samples [90]. Zhang *et al*. observed PL emission peaks at 387 and 426 nm in the $BaWO_4$ microstructures [63]. Cavalcante *et al*. reported that the optical bandgap of $BaWO_4$ powder synthesized by microwave hydrothermal method varied (4.4 − 3.84 eV) with processing time. A green PL emission due to the distortions into the WO_4 tetrahedral group was reported in the literature [39]. Anicete-Santos *et al.* reported that the disorder at a short range of Ba atoms is responsible for the obtained green photoluminescence emission of $BaWO_4$ powders synthesized via the polymeric precursor method [58]. Phuruangrat *et al.*, Shen *et al*. and Lim *et al*. observed blue luminescence for the $BaWO_4$ powders synthesized using cyclic microwave irradiation

[59,70,76]. The emission peak and intensity of PL emission varied with reaction time and preparation temperature [70,76]. Lim *et al*. explained the shoulder peaks observed in the PL spectrum as due to the Jahn-Teller splitting effect and the Frenkel defect [91]. Wu *et al*. found that the PL intensity of $BaWO_4$ obtained via microwave synthesis can be varied by using different surfactants [92].

Cerny *et al*. [93] studied the stimulated Raman scattering (SRS) of 1.06-μm, 50-ps pulses in $BaWO_4$ and KGW ($KGd(WO_4)_2$) crystals. Raman shift of 925 cm^{-1} was observed in $BaWO_4$, the most promising material due to a high value of spectroscopic peak intensity and integral intensity. They proposed $BaWO_4$ (50% efficiency) as a promising candidate for exploitation in all the solid-state Raman Laser systems in a wide range of pumping radiation wavelengths with pulses of picosecond to nanosecond duration. Thermal and mechanical properties of the $BaWO_4$ crystal grown by the Czochralski method were studied by Ge *et al*. [43]. The density of the crystal decreased linearly with an increase in temperature and found that the prepared crystal had good thermal conductivity properties. Measurement of microhardness of the crystal revealed that it was a soft material that can be easily processed and polished.

Basiev *et al.* [94] reported that $BaWO_4$ crystals can be used as an efficient source for both picosecond and nanosecond time scale Raman lasing. Raman lasers based on $BaWO_4$ and $Ba(NO_3)_2$ Raman crystals were developed and investigated. Different Stockes shifted components were obtained with the longest wavelength of about 2.2 μm with an efficiency of up to 10%. They studied the stimulated Raman scattering in the mid IR range (2.31 − 2.75 − 3.7 μm), in a $BaWO_4$ crystal under 1.9 and 1.56 μm pumping. The first Stokes component (2.31 μm), and fourth Stokes components up to 2.75 and 3.7 μm were obtained in a $BaWO_4$ crystal under 1.9 and 1.56 μm pumping, respectively [95]. Lasers in this

spectral range have applications in medicine, air communication lines, and lidar. After the investigation on the UV and IR absorption in $BaWO_4$ crystals, Zverev *et al*. reported that barium tungstate crystals could work efficiently in Raman lasers in visible and near IR (264 − 5300 nm) spectral regions [96].

Zhang *et al.* studied the electronic structures, dielectric function and absorption spectrum for the perfect $BaWO_4$ crystal and $BaWO_4$ crystal containing barium vacancy (V_{Ba}^{2-}) using density functional theory. The results indicated that the optical properties of the $BaWO_4$ crystal exhibit anisotropy and its optical symmetry coincides with the lattice structure geometry of the $BaWO_4$ crystal. The origin of the 370 nm absorption band might be related to the barium vacancy [97].

No detailed reports are found on the magnetic properties of the $BaWO_4$ samples. From VSM studies, Khademolhoseini *et al*. [61] and Talebi *et al*. [74] reported that $BaWO_4$ samples were ferromagnetic with a saturation magnetization of 0.007 $emugm^{-1}$.

The temperature dependence of the dielectric properties of $BaWO_4$ powders sintered at 810 ºC was studied by Vidya *et al.* They found that the dielectric constant is almost discernible with temperature in the measured range. The loss factor has a value of 1.56×10^{-3} at room temperature, which decreases with an increase in temperature. At 5 MHz frequency, the dielectric constant has a value of 9 and 8.5 at room temperature and 250 ºC respectively [62]. They also proposed the use of this $BaWO_4$ material in LTCC applications [62]. Krzmanc *et al*. reported that $BaWO_4$ ceramics synthesized via solid-state method has a constant value of 9 for the dielectric constant in the temperature range 800 − 1100 ºC at a frequency of 11 GHz [44].

There are many reports on $BaWO_4$ as a promising material for photocatalytic degradation of organic dyes present in water under UV light irradiation. The photocatalytic activity of the samples depends on the solution pH, the concentration of $BaWO_4$ nanoparticles, and the initial dye concentration. The photocatalytic activity of $BaWO_4$ particles synthesized by the sonochemical method was tested in methylene blue and rhodamine B and found that complete sorption of the dye was taken within $10 - 15$ min [60]. Sadiq *et al.*, Khademolhoseini *et al*., and Talebi *et al*. also reported $BaWO_4$ catalyst for the degradation of rhodamine B [53] and methyl orange [61,74]. Vijay *et al.* reported the photodegradation of Azure B using $BaWO_4$ as a catalyst. The rate of degradation was maximum at a pH of 7.3 [98].

Doping is an effective method for improving the surface morphology and optical properties of $BaWO_4$ samples [99]. Several reports are available on the studies of the rare earth doped $BaWO_4$ nanoparticles. But no studies reported on the synthesis and properties of Cu doped $BaWO_4$. Theoretical and experimental investigations proved that doping with Cu improves the photocatalytic activity of TiO_2 [100,101]. Blue luminescence was produced by doping with Cu in ZnS microstructures [102]. It is also reported that among various metallic doping elements, Cu doping can reduce the bandgap of the material, which modifies the absorption in the visible region and the photocatalysis in mesoporous TiO_2 [103].

Rare earth activated tungstate luminescent materials have outstanding photo-stabilities, large Stokes/anti-Stokes shifts, long luminescence life times, and sharp band emissions [26]. A detailed literature survey based on that property is given below.

Various luminescence emission can be obtained by doping $BaWO_4$ material with Eu^{3+}, Tb^{3+} and Tm^{3+} ions [104–109]. Jinsheng *et al*. reported that doping of $BaWO_4$ with Pr^{3+} ions would yield deep red emission [110]. The peaks due to f-f transition in the blue region of Pr^{3+} in Pr^{3+} doped $BaWO_4$ were investigated by Cavalcante *et al*. [111]. Studies on the Dy^{3+} doped $BaWO_4$ sample show that several emission lines can be obtained from the sample corresponding to the f-f transition in Dy^{3+} [112–114]. Photoluminescence emission in the NIR region can be achieved by doping with rare earth elements Nd^{3+}, Er^{3+} and Yb^{3+}. A prominent emission band around 977 nm was observed by Hou *et al.* for $BaWO_4$: Yb samples, which have potential application in telecommunication and laser emission [115].

Chao *et al*. reported that $BaWO_4$:Yb^{3+}/Tm^{3+} nanocrystals showed four photoluminescence emission lines at 454, 475, 647, and 790 nm with an excitation at 980 nm [116]. The emission intensity was maximum for 1 mol% Tb^{3+}, above that emission intensity decreases. Here Yb^{3+} acts as a sensibilization center. There are several reports that Ce^{3+} and Ce^{4+} doping can contribute to the intensity of blue luminescence emission in $BaWO_4$ samples [117–120].

In recent years, electron beam irradiation effects of nanoparticles became an important area of research because beam irradiation can modify the structural, optical, and electrical properties of the nanoparticles [121–128]. Beam irradiation can cause intrinsic defects in the sample in a controlled manner and results in re-growth and crystallization of the materials. The changes in material properties occur due to the inherent defects or charge carries produced during electron beam irradiation. Hence this is a promising technique for the modification of the structural, optical, and electrical properties of the nanomaterials [129–136].

1.4 Relevance of the Present Study

Several studies have been reported on the synthesis and characterization of nanocrystalline $BaWO_4$. The large bandgap of $BaWO_4$ has restricted its application in diverse fields. Hence, tailoring of the bandgap is essential for modifying the properties of $BaWO_4$ for optoelectronic device applications. Literature survey indicated that the bandgap of several nanocrystalline samples can be tuned by electron beam irradiation and by doping with suitable dopants. However, there are no reports on the effect of electron beam irradiation on the structural and optical properties of the $BaWO_4$. Furthermore, there are no reports on the effect of copper doping on the structural, optical, and magnetic properties of $BaWO_4$. Literature reports that doping with ytterbium will yield NIR photoluminescence, which has wide application. However, reports on the influence of ytterbium on the structural, optical, and magnetic properties of $BaWO_4$ are sparse. Hence more extensive and systematic studies of pristine and doped nanocrystalline $BaWO_4$ is needed. The present study mainly focuses on the synthesis and characterization of nanocrystalline $BaWO_4$, Cu doped $BaWO_4$, and Yb doped $BaWO_4$. In addition, the effect of 8 MeV electron beam irradiation on the structural and optical properties of $BaWO_4$ is also investigated.

1.5 Objectives of the Study

- Synthesis of pure and nanocrystalline $BaWO_4$ powder by chemical precipitation method.
- Investigation on the structural, optical, magnetic and electrical properties of the synthesized nanocrystalline $BaWO_4$.
- Study of the effect of calcination temperature on the structural, optical, magnetic and electric properties $BaWO_4$.

- ❖ Study of the effect of copper doping on the structural, optical and magnetic properties of nanocrystalline $BaWO_4$.
- ❖ Study of the effect of ytterbium doping on the structural, optical and magnetic properties of nanocrystalline $BaWO_4$.
- ❖ Study of the effect of 8MeV electron beam irradiation on the structural and optical properties of the nanocrystalline $BaWO_4$.

References

[1] A.P. Alivisatos, Perspectives on the physical chemistry of semiconductor nanocrystals, J. Phys. Chem. 100 (1996) 13226–13239.

[2] X. Peng , L. Manna, W. Yang, J. Wickham, E. Scher, A. Kadavanich, A.P. Alivisatos, Shape control of CdSe nanocrystals, Nature. 404 (2000) 59–61.

[3] X. Duan , Y. Huang, Y. Cui, J. Wang, C.M. Lieber, Indium phosphide nanowires as building blocks for nanoscale electronic and optoelectronic devices, Nature. 409 (2001) 66–69.

[4] V.F. Puntes , K.M. Krishnan, A.P. Alivisatos, Colloidal nanocrystal shape and size control: the case of cobalt, Science. 291 (2001) 2115–2117.

[5] F. Kim, J.H. Song, P. Yang, Photochemical synthesis of gold nanorods, J. Am. Chem. Soc. 124 (2002) 14316–14317.

[6] A.M. Morales, C.M. Lieber, A laser ablation method for the synthesis of crystalline semiconductor nanowires, Science 279 (1998) 208–211.

[7] J. Hu, T.W. Odom, C.M. Lieber, Chemistry and physics in one dimension: synthesis and properties of nanowires and nanotubes, Acc. Chem. Res. 32 (1999) 435–445.

[8] M.A. El-Sayed, Some interesting properties of metals confined in time and nanometer space of different shapes, Acc. Chem. Res. 34 (2001) 257–264.

[9] N.R. Jana, Z.L. Wang, T.K. Sau, T. Pal, Seed-mediated growth method to prepare cubic copper nanoparticles, Curtrent Sci. 79 (2000) 1367–1369.

[10] Y. Sun, Y. Xia, Shape-controlled synthesis of gold and silver nanoparticles, Science. 298 (2002) 2176–2179.

[11] L. Gou, C.J. Murphy, Solution-phase synthesis of Cu_2O nanocubes, Nano Lett. 12 (2003) 231–234.

[12] A. Chow, D. Toomre, W. Garrett, I. Mellman, Dendritic cell maturation triggers retrograde MHC class II transport from lysosomes to the plasma membrane, Nature. 418 (2002) 988–994.

[13] D. Kuang, A. Xu , Y. Fang, H. Liu, C. Frommen, D. Fenske, Surfactant-assisted growth of novel PbS dendritic nanostructures via facile hydrothermal process, Adv. Mater. 15 (2003) 1747–1750.

[14] T. Okutsu, K. Nakamura, H. Haneda, H. Hiratsuka, Laser-induced crystal growth and morphology control of benzopinacol produced from benzophenone in ethanol/water mixed solution, Cryst. Growth Des. 4 (2004) 113–115.

[15] A. Bigi, B. Bracci B, S. Panzavolta, M. Iliescu, M. Plouet-Richard, J. Werckmann, D. Cam, Morphological and structural modifications of octacalcium phosphate induced by poly-L-aspartate, Cryst. Growth Des. 4 (2004) 141–146.

[16] T. Jung, W.S. Kim, C.K. Choi, Effect of nonstoichiometry on reaction

crystallization of calcium carbonate in a couette− Taylor reactor, Cryst. Growth Des. 4 (2004) 491–495.

[17] N. Imanaka, T. Masui, Y.W. Kim, First electrochemical growth of δ-Al_2O_3 single crystal, Cryst. Growth Des. 4 (2004) 663–665.

[18] Q.S. Wu, D.M. Sun, H.J. Liu, Y.P. Ding, Abnormal polymorph conversion of calcium carbonate and nano-self-assembly of vaterite by a supported liquid membrane system, Cryst. Growth Des. 4 (2004) 717–720.

[19] Y. Ni, H. Liu, F. Wang, Y. Liang, J. Hong, X. Ma, Z. Xu, Shape controllable preparation of PbS crystals by a simple aqueous phase route, Cryst. Growth Des. 4 (2004) 759–764.

[20] J. Yang, L. Qi, D. Zhang, J. Ma, H. Cheng, Dextran-controlled crystallization of silver microcrystals with novel morphologies, Cryst. Growth Des. 4 (2004) 1371–1375.

[21] G. Zhang, R. Jia, Q. Wu, Preparation, structural and optical properties of AWO_4 (A = Ca, Ba, Sr) nanofilms, Mater. Sci. Eng. B Solid-State Mater. Adv. Technol. 128 (2006) 254–259.

[22] B. Xie, Y. Wu, Y. Jiang, F. Li, J. Wu, S. Yuan, W. Yu, Y. Qian, Shape-controlled synthesis of $BaWO_4$ crystals under different surfactants, J. Cryst. Growth. 235 (2002) 283–286.

[23] Z. Luo, H. Li, J. Xia, W. Zhu, J. Guo, B. Zhang, Controlled synthesis of different morphologies of $BaWO_4$ crystals via a surfactant-assisted method, J. Cryst. Growth. 300 (2007) 523–529.

[24] T. Thongtem, A. Phuruangrat, S. Thongtem, Characterization of $MeWO_4$

(Me = Ba, Sr and Ca) nanocrystallines prepared by sonochemical method, Appl. Surf. Sci. 254 (2008) 7581–7585.

[25] B.G. Wang, E.W. Shi, W.Z. Zhong, Z.W. Yin, Relationship between the orientations of tetrahedral $[WO_4]^{2-}$ in tungstate crystals and their morphology, J Inorg Mate. 13 (1998) 648–654.

[26] C. Koepke, A.J. Wojtowicz, A. Lempicki, Excited-state absorption in excimer-pumped $CaWO_4$ crystals, J Lumin. 54 (1993) 345–355.

[27] B. M. Sinelnikov, E.V. Sokolenko, V. Zvekov, The nature of green luminescence centers in scheelite, Inorg Mater. 32 (1996) 999–1001.

[28] T.G. Cooper, N.H. Leeuw, A combined ab initio and atomistic simulation study of the surface and interfacial structures and energies of hydrated scheelite: Introducing a $CaWO_4$ potential model, Surf.Sci. 531 (2003) 159–179.

[29] W.S. Cho, M. Yashima, M. Kakihana, A. Kudo, T. Sakata, M. Yoshimura, Room--temperature preparation of the highly crystallized luminescent $CaWO_4$ film by an electrochemical method, Appl Phys Lett. 66 (1995) 1027–1029.

[30] A. Kuzmin, J. Purans, Local atomic and electronic structure of tungsten ions in AWO_4 crystals of scheelite and wolframite types, Rad. Meas. (2001) 583–586.

[31] B. Grobelna, B. Lipowska, A. M. Klonkowski, Energy transfer in calcium tungstate doped with Eu(III) or Tb(III) ions incorporated into silica xerogel, J Alloy. Compd. 419 (2006) 191–196.

[32] J. Tamaki, T. Fujii, K. Fujimori, N. Miura, N. Yamazoe, Application of metal tungstate-carbonate composite to nitrogen oxides sensor operative at elevated temperature, Sensors Actuators B. 25 (1995) 396–399.

[33] D.L. Stern, R.K. Grasselli, Propane oxydehydrogenation over metal tungstates, J Catal. 167 (1997) 570–572.

[34] S. H. Yu, B. Liu, M.S. Mo, J.H. Huang, X.M. Li, Y.T. Qian, General synthesis of single-crystal tungstate nanorods/nanowires: A facile low temperature solution approach, Adv Funct Mater. 13 (2002) 639–647.

[35] S.M. Zawawi, R. Yahya, A. Hassan, H.E. Mahmud, M.N. Daud, Structural and optical characterization of metal tungstates (MWO_4; M=Ni, Ba, Bi) synthesized by a sucrose-templated method, Chem. Cent. J. 7 (2013) 1–10.

[36] Vishwamittar, S.P. Puri, Investigation of the crystal field in rare-earth doped scheelites, J. Chem. Phys. 61 (1974) 3720–3727.

[37] J.T. Hoard, J.V. Silverton, Stereochemistry of discrete eight-coördination. I. Basic analysis, Inorg. Chem. 2 (1963) 235–242.

[38] P. Goel, M.K. Gupta, R. Mittal, S. Rols, S.N. Achary, A.K. Tyagi, S.L. Chaplot, Inelastic neutron scattering studies of phonon spectra, and simulations of pressure-induced amorphization in tungstates AWO_4 (A=Ba, Sr, Ca, and Pb), Phys. Rev. B - Condens. Matter Mater. Phys. 91 (2015) 1–8.

[39] L.S. Cavalcante, J.C. Sczancoski, J.W.M. Espinosa, J.A. Varela, P.S. Pizani, E. Longo, Photoluminescent behavior of $BaWO_4$ powders processed in microwave-hydrothermal, J. Alloys Compd. 474 (2009) 195–200.

[40] P. Number, I. Area, A. Taluka, Barium tungstate, (2021) 1–8.

[41] D.L. Perry, Handbook of Inorganic Compounds (2nd ed.), CRC Press, Taylor and Francis Group, 2011.

[42] I. Kawada, K. Kato, T. Fujita, $BaWO_4$-II (A High-Pressure Form), Acta Crystallogr. Sect. B. 30442 (1974) 2069–2071.

[43] W.W. Ge, H.J. Wang, J.Y. Wang, J.H. Liu, X.G. Xu, X.B. Hu, M.H. Jiang, D.G. Ran, S.Q. Sun, H.R. Xia, R.I. Boughton, Thermal and mechanical properties of $BaWO_4$ crystal, J. Appl. Phys. 98 (2005) 013542.

[44] M.M. Kržmanc, M. Logar, B. Budič, D. Suvorov, Dielectric and microstructural study of the $SrWO_4$, $BaWO_4$, and $CaWO_4$ scheelite ceramics, J. Am. Ceram. Soc. 94 (2011) 2464–2472.

[45] W. Chen, Y. Inagawa, T. Omatsu, M. Tateda, N. Takeuchi, Y. Usuki, Diode-pumped, self-stimulating, passively Q-switched Nd^{3+}: $PbWO_4$ Raman laser, Opt. Commun. 194 (2001) 401–407.

[46] S. Takai, K. Sugiura, T. Esaka, Ionic conduction properties of $Pb_{1-x}M_xWO_{4+\delta}$ (M = Pr, Tb), Mater Res Bull. 34 (1999) 193–202.

[47] V. Nagirnyi, E. Feldbach, L. Jönsson, M. Kirm, A. Lushchik, C. Lushchik, L.L. Nagornaya, V.D. Ryzhikov, F. Savikhin, G. Svensson, Excitonic and recombination processes in $CaWO_4$ and $CdWO_4$ scintillators under synchrotron irradiation, Radiat. Meas. 29 (1998) 247–250.

[48] T. Esaka, Ionic conduction in substituted scheelite-type oxides, Solid State Ionics. 136 (2000) 1–9.

[49] G. Zhang, S. Yang, Z. Li, L. Zhang, W. Zhou, H. Zhang, H. Shen, Y. Wang, Synthesis and photoluminescence properties of aqueous $CdWO_4$ quantum dots with WO_{66}− luminescence center, Appl. Surf. Sci. 257 (2010) 302–305.

[50] S. Nishigaki, S. Yano, H. Kato, T. Hirai, T. Nanomura, $BaO\text{-}TiO_2\text{-}WO_3$ microwave ceramics and crystalline $BaWO_4$, Commun. Am. Ceram. Soc. 17 (1988) 0–6.

[51] G.K. Sahu, S. Behera, Investigation of optical and structural properties of scheelite-type barium tungstate ceramic, Int. J. Manag. Technol. Eng. 8 (2018) 2314–2320.

[52] L.S. Cavalcante, J.C. Sczancoski, L.F. Lima, J.W.M. Espinosa, P.S. Pizani, J.A. Varela, E. Longo, Synthesis, characterization, anisotropic growth and photoluminescence of $BaWO_4$, Cryst. Growth Des. 9 (2009) 1002–1012.

[53] M. Mohamed Jaffer Sadiq, A. Samson Nesaraj, Soft chemical synthesis and characterization of $BaWO_4$ nanoparticles for photocatalytic removal of Rhodamine B present in water sample, J. Nanostructure Chem. 5 (2015) 45–54.

[54] M.C. Oliveira, L. Gracia, I.C. Nogueira, M.F. Do Carmo Gurgel, J.M.R. Mercury, E. Longo, J. Andrés, Synthesis and morphological transformation of $BaWO_4$ crystals: Experimental and theoretical insights, Ceram. Int. 42 (2016) 10913–10921.

[55] C. Zhang, E. Shen, E. Wang, Z. Kang, L. Gao, C. Hu, L. Xu, One-step solvothermal synthesis of high ordered $BaWO_4$ and $BaMoO_4$ nanostructures, Mater. Chem. Phys. 96 (2006) 240–243.

[56] S. Kwan, F. Kim, J. Akana, P. Yang, Synthesis and assembly of $BaWO_4$ nanorods, Chem. Commun. (2001) 447–448.

[57] M.V.S. Lima, L.S. Cavalcante, J.C. Sczancoski, C. Nogueira, E. Longo and J. A. Varela, Influence of ethylene glycol on the morphology and photoluminescence of $BaWO_4$ powders processed in, microwave hydrothermal, 1012 (2009) 13560.

[58] M. Anicete-Santos, F.C. Picon, C.N. Alves, P.S. Pizani, J.A. Varela, E. Longo, The role of short-range disorder in $BaWO_4$ crystals in the intense green photoluminescence, J. Phys. Chem. C. 115 (2011) 12180–12186.

[59] A. Phuruangrat, T. Thongtem, S. Thongtem, Barium molybdate and barium tungstate nanocrystals synthesized by a cyclic microwave irradiation, J. Phys. Chem. Solids. 70 (2009) 955–959.

[60] A. Singh, D.P. Dutta, J. Ramkumar, K. Bhattacharya, A.K. Tyagi, M.H. Fulekar, Serendipitous discovery of super adsorbent properties of sonochemically synthesized nano $BaWO_4$, RSC Adv. 3 (2013) 22580–22590.

[61] S. Khademolhoseini, S. Ali Zarkar, Preparation and characterization of barium tungstate nanoparticles via a new simple surfactant-free route, J. Mater. Sci. Mater. Electron. 27 (2016) 9605–9609.

[62] S. Vidya, S. Solomon, J.K. Thomas, Synthesis, characterization, and low temperature sintering of nanostructured $BaWO_4$ for optical and LTCC applications, Adv. Condens. Matter Phys. 2013 (2013) 1–11.

[63] L. Zhang, J. Sen Dai, L. Lian, Y. Liu, Dumbbell-like $BaWO_4$ microstructures: Surfactant-free hydrothermal synthesis, growth mechanism and photoluminescence property, Superlattices Microstruct. 54 (2013) 87–95.

[64] G. Zha, N. Hu, M. Jiang, X. Zeng, H. Hou, Synthesis and properties of $BaWO_4$ nanocrystals prepared using a reverse microemulsion method, Appl. Phys. A Mater. Sci. Process. 125 (2019) 1–6.

[65] H. Shi, X. Wang, N. Zhao, L. Qi, J. Ma, Growth mechanism of penniform $BaWO_4$ nanostructures in catanionic reverse micelles involving polymers, J. Phys. Chem. B. 110 (2006) 748–753.

[66] M. Pedro, A. Fernando, Synthesis of $BaWO_4$ hollow structures, Cryst. Growth Des. 6 (2006) 6–9.

[67] R. Wang, C. Liu, J. Zeng, K.W. Li, H. Wang, Fabrication and morphology control of $BaWO_4$ thin films by microwave assisted chemical bath deposition, J. Solid State Chem. 182 (2009) 677–684.

[68] L.A. Al-Hajji, M.A. Hasan, M.I. Zaki, Kinetics of formation of barium tungstate in equimolar powder mixture of $BaCO_3$ and WO_3: Thermogravimetric and spectroscopic studies, J. Therm. Anal. Calorim. 100 (2010) 43–49.

[69] B.A. Hernandez-Sanchez, T.J. Boyle, H.D. Pratt, M.A. Rodriguez, L.N. Brewer, D.R. Dunphy, Morphological and phase controlled tungsten based nanoparticles: Synthesis and characterization of scheelite, wolframite, and oxide nanomaterials, Chem. Mater. 20 (2008) 6643–6656.

[70] Y. Shen, W. Li, T. Li, Microwave-assisted synthesis of $BaWO_4$ nanoparticles and its photoluminescence properties, Mater. Lett. 65 (2011) 2956–2958.

[71] S.M. Pourmortazavi, M. Taghdiri, N. Samimi, M. Rahimi-Nasrabadi, Eggshell bioactive membrane assisted synthesis of barium tungstate nanoparticles, Mater. Lett. 121 (2014) 5–7.

[72] Y. Liu, Y. Chu, Surfactant-assisted synthesis of single crystal $BaWO_4$ octahedral microparticles, Mater. Chem. Phys. 92 (2005) 59–63.

[73] X. Zhang, Y. Xie, F. Xu, X. Tian, Growth of $BaWO_4$ fishbone-like nanostructures in w/o microemulsion, J. Colloid Interface Sci. 274 (2004) 118–121.

[74] R. Talebi, Synthesis and characterization of $BaWO_4$ nanoparticles with the aid of different surfactants and their photocatalyst properties, J. Mater. Sci. Mater. Electron. 28 (2017) 6782–6787.

[75] S.M.M. Zawawi, R. Yahya, A. Hassan, M.N. Daud, Preparation and characterisation of tungstate scheelite structured nanoparticles, Mater. Res. Innov. 15 (2011) 97–100.

[76] C.S. Lim, Solid-state metathetic synthesis of $BaMO_4$ (M = W, Mo) assisted by microwave irradiation, J. Ceram. Process. Res. 12 (2011) 544–548.

[77] R. Lacomba-Perales, D. Martinez-García, D. Errandonea, Y. Le Godec, J. Philippe, G. Le Marchand, J.C. Chervin, A. Polian, A. Múñoz, J. López-Solano, Experimental and theoretical investigation of the stability of the monoclinic $BaWO_4$-II phase at high pressure and high temperature, Phys. Rev. B - Condens. Matter Mater. Phys. 81 (2010) 1–10.

[78] D.Y. Tan, W.S. Xiao, W. Zhou, M. Chen, X.L. Xiong, M.S. Song, First-order character of the displacive structural transition in $BaWO_4$, Chinese Phys. B. 21 (2012) 1–9.

[79] O. Gomis, J.A. Sans, R. Lacomba-Perales, D. Errandonea, Y. Meng, J.C. Chervin, A. Polian, Complex high-pressure polymorphism of barium tungstate, Phys. Rev. B - Condens. Matter Mater. Phys. 86 (2012) 54121-1-54121-10.

[80] D. Sivaganesh, S. Saravanakumar, V. Sivakumar, R. Sangeetha, L.J. Berchmans, K.S.S. Ali, A.M. Alshehri, Effect of preparation techniques on $BaWO_4$: structural, morphological, optical and electron density distribution analysis, J. Mater. Sci. Mater. Electron. 32 (2021) 1466–75.

[81] E.I. Ross-Medgaarden, I.E. Wachs, Structural determination of bulk and surface tungsten oxides with UV-vis diffuse reflectance spectroscopy and raman spectroscopy, J. Phys. Chem. C. 111 (2007) 15089–15099.

[82] W.M. Yen', S. Shionoya, H. Yamamoto, eds., Fundamentals of Phosphors, CRC Press, Taylor and Francis Group, 2007.

[83] G. Blasse, Classical phosphors: A Pandora's box, J. Lumin. 72–74 (1997) 129–134.

[84] M. Nikl, P. Bohacek, E. Mihokova, M. Kobayashi, M. Ishii, Y. Usuki, V. Babin, A. Stolovich, S. Zazubovich, M. Bacci, Excitonic emission of scheelite tungstates AWO_4 (A = Pb, Ca, Ba, Sr), J. Lumin. 87 (2000) 1136–1139.

[85] F.M. Pontes, M.A.M.A. Maurera, A.G. Souza, E. Longo, E.R. Leite, R. Magnani, M.A.C. Machado, P.S. Pizani, J.A. Varela, Preparation, structural and optical characterization of $BaWO_4$ and $PbWO_4$ thin films prepared by a chemical route, J. Eur. Ceram. Soc. 23 (2003) 3001–3007.

[86] A.A. Blistanov, B.I. Zadneprovskiĭ, M.A. Ivanov, V. V. Kochurikhin, V.S. Petrakov, I.O. Yakimova, Luminescence of crystals of divalent tungstates, Crystallogr. Reports. 50 (2005) 284–290.

[87] R.C. Lima, M. Anicete-Santos, E. Orhan, M.A.M.A. Maurera, A.G. Souza, P.S. Pizani, E.R. Leite, J.A. Varela, E. Longo, Photoluminescent property of mechanically milled $BaWO_4$ powder, J. Lumin. 126 (2007) 741–746.

[88] R. Lacomba-Perales, J. Ruiz-Fuertes, D. Errandonea, D. Martínez-García, A. Segura, Optical absorption of divalent metal tungstates: Correlation between the band-gap energy and the cation ionic radius, Epl. 83 (2008) 1–16.

[89] P. Parhi, T.N. Karthik, V. Manivannan, Synthesis and characterization of metal tungstates by novel solid-state metathetic approach, J. Alloys Compd. 465 (2008) 380–386.

[90] M. Tyagi, Sangeeta, S.C. Sabharwal, Luminescence properties of $BaWO_4$ single crystal, J. Lumin. 128 (2008) 1528–1532.

[91] C.S. Lim, Cyclic microwave synthesis and photoluminescence of barium tungstate particles assisted by a solid-state metathetic reaction, Asian J. Chem. 25 (2013) 63–66.

[92] D. Wu, S. Luo, S. Yang, X. Liao, Microwave synthesis and photoluminescence properties of $BaWO_4$ of homogeneous double cone structure, J. Mater. Sci. Chem. Eng. 05 (2017) 64–69.

[93] P. Cerny, H. Jelinkova, M. Miyagi, T.T. Basiev, P.G. Zverev, Efficient picosecond Raman lasers on $BaWO_4$ and $KGd(WO_4)_2$ tungstate crystals emitting in 1.15 to 1.18μm spectral region, Solid State Lasers XI. 4630 (2002) 108–118.

[94] T.T. Basiev, M.E. Doroshenko, V. V. Osiko, S.E. Sverchkov, B.I. Galagan, New mid IR (1.5-2.2 μm) Raman lasers based on barium tungstate and barium nitrate crystals, Laser Phys. Lett. 2 (2005) 237–238.

[95] T.T. Basiev, M.N. Basieva, M.E. Doroshenko, V. V. Fedorov, V. V. Osiko, S.B. Mirov, Stimulated Raman scattering in mid IR spectral range 2.31-2.75-3.7 μm in $BaWO_4$ crystal under 1.9 and 1.56 μm pumping, Laser Phys. Lett. 3 (2006) 17–20.

[96] P.G. Zverev, L.I. Ivleva, Optical properties of barium and strontium tungstate Raman crystals, Work. Proc. - Int. Work. Nonlinear Photonics, NLP 2011. (2011) 1–2.

[97] H. Zhang, T. Liu, Q. Zhang, X. Wang, X. Guo, M. Song, J. Yin, First-principles study on electronic structures and absorption spectra for $BaWO_4$ crystal containing barium vacancy, Nucl. Instruments Methods Phys. Res. Sect. B Beam Interact. with Mater. Atoms. 267 (2009) 1056–1060.

[98] A. Vijay, S. Nihalani, S. Bhardwaj, Measurement of kinetic parameters: Use of novel nano sized photocatalyst $BaWO_4$ for degradation of Azure B, Int. J. Chem. Sci. Appl. 5 (2014) 2278–6015.

[99] N.V. Pillai, R. Vinodkumar, V. Ganesan, P. Koshy, V.P.M. Pillai, Effect of ZnO doping on the structural and optical properties of $BaWO_4$ thin films prepared using pulsed laser ablation technique, Pramana - J. Phys. 75 (2010) 1157–1161.

[100] M.H.N. Assadi, D.A.H. Hanaor, The effects of copper doping on photocatalytic activity at (101) planes of anatase TiO_2 : A theoretical study, Appl. Surf. Sci. 387 (2016) 682–689.

[101] L.S. Yoong, F.K. Chong, B.K. Dutta, Development of copper-doped TiO_2 photocatalyst for hydrogen production under visible light, Energy. 34 (2009) 1652–1661.

[102] N. Nguyen Van, Photoluminescence emission of Cu doped ZnS microstructures synthesized by thermal evaporation, VNU J. Sci. Math. - Phys. 34 (2018) 1–7.

[103] Y. Wang, W. Duan, B. Liu, X. Chen, F. Yang, J. Guo, The effects of doping copper and mesoporous structure on photocatalytic properties of TiO_2, J. Nanomater. 2014 (2014) 1–7.

[104] H.L. Li, Z.L. Wang, J.H. Hao, Red, green and blue low-voltage cathodoluminescence of rare-earth doped $BaWO_4$ phosphors , IOP Conf. Ser. Mater. Sci. Eng. 1 (2009) 012010.

[105] P. Jena, S.K. Gupta, N.K. Verma, A.K. Singh, R.M. Kadam, Energy transfer dynamics and time resolved photoluminescence in $BaWO_4:Eu^{3+}$ nanophosphors synthesized by mechanical activation, New J. Chem. 41 (2017) 8947–8958.

[106] W. Deng, F. Chun, W. Li, H. Su, B. Zhang, M. Xie, H. Zhang, X. Chu, L. Jin, C. Luo, W. Yang, Structural and optical investigations of quasi-single crystal Eu^{3+}-doped $BaWO_4$ thin films, Langmuir. 34 (2018) 8499–8507.

[107] J. Liao, B. Qiu, H. Wen, W. You, Y. Xiao, Synthesis and optimum luminescence of monodispersed spheres for $BaWO_4$-based green phosphors with doping of Tb^{3+}, J. Lumin. 130 (2010) 762–766.

[108] H. Ramanantoanina, L. Merzoud, J.T. Muya, H. Chermette, C. Daul, Electronic structure and photoluminescence properties of $Eu(\eta^9\text{-}C_9H_9)_2$, J. Phys. Chem. A. 124 (2020) 152–164.

[109] Y. Shi, J. Shi, C. Dong, Refinement and luminescent properties of $BaWO_4$: xSm^{3+} yellow phosphor by a low temperature molten salt method, Opt. Mater. (Amst). 84 (2018) 396–403.

[110] J. Liao, H. You, S. Zhang, J. Jiang, B. Qiu, H. Huang, H. Wen, Synthesis and luminescence properties of $BaWO_4:Pr^{3+}$ microcrystal, J. Rare Earths. 29 (2011) 623–627.

[111] L.S. Cavalcante, F.M.C. Batista, M.A.P. Almeida, A.C. Rabelo, I.C. Nogueira, N.C. Batista, J.A. Varela, M.R.M.C. Santos, E. Longo, M. Siu Li, Structural refinement, growth process, photoluminescence and photocatalytic properties of $(Ba_{1-x}Pr_{2x/3})WO_4$ crystals synthesized by the coprecipitation method, RSC Adv. 2 (2012) 6438–6454.

[112] A.K. Ambast, A.K. Kunti, S. Som, S.K. Sharma, Near-white-emitting phosphors based on tungstate for phosphor-converted light-emitting diodes, Appl. Opt. 52 (2013) 8424–8431.

[113] G. Jia, D.B. Dong, J.Y. Liu, Q.Y. Kang, C.M. Zhang, Well-defined $BaWO_4:Dy^{3+}$ luminescent materials: Hydrothermal synthesis and luminescence properties, Adv. Mater. Res. 998–999 (2014) 128–131.

[114] P. Hu, W. Zhang, Z. Hu, Z. Feng, L. Ma, X. Zhang, X. Sheng, J. Luo, Luminescence properties of phosphate phosphor: Barium tungstate doped with Dy, J. Mater. Sci. Chem. Eng. 04 (2016) 37–44.

[115] S. Hou, Y. Xing, H. Ding, X. Liu, B. Liu, X. Sun, Facile synthesis and photoluminescence properties of dumbbell-like Ln-doped $BaWO_4$ (Ln = Nd, Er, Yb) microstructures, Mater. Lett. 64 (2010) 1503–1505.

[116] C. He, K. Yang, L. Liu, Z. Si, Preparation and luminescence properties of $BaWO_4:Yb^{3+}/Tm^{3+}$ nano-crystal, J. Rare Earths. 31 (2013) 790–794.

[117] K. V. Dabre, S.J. Dhoble, J. Lochab, Synthesis and luminescence properties of Ce^{3+} doped MWO_4 (M=Ca, Sr and Ba) microcrystalline phosphors, J. Lumin. 149 (2014) 348–352.

[118] W.L. Feng, C.Y. Tao, K. Wang, Synthesis and photoluminescence of tetravalent cerium-doped alkaline-earth-metal tungstate phosphors by a co-precipitation method, Spectrosc. Lett. 48 (2015) 381–385.

[119] D. Wlodarczyk, L.I. Bulyk, M. Berkowski, M. Glowacki, K.M. Kosyl, S.M. Kaczmarek, Z. Kowalski, A. Wittlin, H. Przybylinska, Y. Zhydachevskyy, A. Suchocki, High-pressure low temperature optical

studies of $BaWO_4$:Ce,Na crystals, Inorg. Chem. 58 (2019) 5617–5629.

[120] S.M. Kaczmarek, G. Leniec, T. Bodziony, H. Fuks, Z. Kowalski, W. Drozdowski, M. Berkowski, M. Głowacki, M.E. Witkowski, M. Makowski, $BaWO_4$:Ce single crystals codoped with Na ions, Crystals. 9 (2019) 1–11.

[121] J. Jun, J.C. Kim, J.H. Shin, K.W. Lee, Y.S. Baek, Effect of electron beam irradiation on CO_2 reforming of methane over Ni/Al_2O_3 catalysts, Radiat. Phys. Chem. 71 (2004) 1095–1101.

[122] D. Teweldebrhan, A.A. Balandin, Modification of graphene properties due to electron-beam irradiation, Appl. Phys. Lett. 94 (2009) 94–97.

[123] K. Hareesh, G. Sanjeev, 8 MeV Electron induced changes in structural and thermal properties of Lexan Polycarbonate, Mater. Sci. Appl. 02 (2011) 1682–1687.

[124] K.P. Priyanka, N. Aloysius Sabu, A.T. Sunny, P.A. Sheena, T. Varghese, Effect of electron beam irradiation on optical properties of manganese tungstate nanoparticles, J. Nanotechnol. 2013 (2013) 1–7.

[125] E.B. Yakimov, Low energy electron irradiation effect on optical and electrical properties of InGaN/GaN multiple quantum well structures, Int. J. Nanoparticles. 6 (2013) 191–200.

[126] S. Chethan Pai, M.P. Joshi, S. Raj Mohan, T.S. Dhami, J. Khatei, K.S. Koteshwar Rao, L.M. Kukreja, G. Sanjeev, Effect of electron beam irradiation on photoluminescence properties of thioglycolic acid (TGA) capped CdTe nanoparticles, Adv. Mater. Lett. 4 (2013) 454–457.

[127] K. Jeon, S.W. Shin, J. Jo, M.S. Kim, J.C. Shin, C. Jeong, J.H. Lim, J. Song, J. Heo, J.H. Kim, Effects of electron-beam irradiation on structural, electrical, and optical properties of amorphous indium gallium zinc oxide thin films, Curr. Appl. Phys. 14 (2014) 1591–1595.

[128] M.J. Jung, M.S. Park, Y.S. Lee, Effects of E-beam irradiation on the chemical, physical, and electrochemical properties of activated carbons for electric double-layer capacitors, J. Nanomater. 2015 (2015) 1–8.

[129] E.B. Yakimov, P.S. Vergeles, A.Y. Polyakov, D.W. Jeon, I.H. Lee, Low energy electron beam irradiation effect on optical properties of nanopillar MQW InGaN/GaN structures, AIP Conf. Proc. 1583 (2014) 268–271.

[130] J. Andres, E. Longo, A.F. Gouveia, L. Gracia, M.C. Oliveira, In situ formation of metal nanoparticles through electron beam irradiation: Modeling real materials from first-principles calculations, J. Mater. Sci. Eng. 07 (2018) 1000461.

[131] B. Christopher, R. Thomas, A. Rao, G.S. Okram, V.C. Petwal, V.P. Verma, J. Dwivedi, A systematic study on effect of electron beam irradiation on electrical properties and thermopower of $RE_{0.8}Sr_{0.2}CoO_3$ (RE=La, Pr) cobaltites, Phys. B Condens. Matter. 552 (2019) 170–177.

[132] K.K. Babitha, K.P. Priyanka, A. Sreedevi, S. Ganesh, T. Varghese, Effect of 8 MeV electron beam irradiation on the structural and optical properties of CeO_2 nanoparticles, Mater. Charact. 98 (2014) 222–227.

[133] P.A. Sheena, K.P. Priyanka, N. Aloysius Sabu, S. Ganesh, T. Varghese, Effect of electron beam irradiation on the structure and optical properties of nickel oxide nanocubes, Bull. Mater. Sci. 38 (2015) 825–830.

[134] N. Aloysius Sabu, K.P. Priyanka, S. Ganesh, T. Varghese, Modifications in the structural and optical properties of nanocrystalline $CaWO_4$ induced by 8 MeV electron beam irradiation, Radiat. Phys. Chem. 123 (2016) 1–5.

[135] A. Sreedevi, K.P. Priyanka, K.K. Babitha, S. Ganesh, T. Varghese, Influence of electron beam irradiation on structural and optical properties of α-Ag_2WO_4 nanoparticles, Micron. 88 (2016) 1-6.

[136] N. Aloysius Sabu, X. Francis, S. Ganesh, T. Varghese, Effect of 8 MeV electron beam irradiation on the structural, optical and electrical properties of a PANI-$MnWO_4$ nanocomposite, Eur. Phys. J. Plus. 134 (2019)1–10.

Chapter 2

CHARACTERIZATION TECHNIQUES

This chapter mainly focuses on the theory behind the characterization techniques used for the investigation of the different properties of the prepared samples. Thermogravimetric Analysis is employed to study the thermal stability of the sample. The structural characterization techniques include X-ray Diffraction, Scanning Electron Microscopy, Energy Dispersive X-ray Spectroscopy, High Resolution Transmission Electron microscopy, Fourier Transform Infrared Spectroscopy, and Raman Spectroscopy. The optical properties of the samples are analyzed using UV-visible and Photoluminescence Spectroscopic methods. Vibrating Sample Magnetometer is used to investigate the magnetic properties of the samples. Electrical studies are carried out using AC conductivity and dielectric measurements.

2.1. Introduction

The proper analysis of different functional properties of the synthesized nanocrystalline materials by employing various characterization techniques is essential to explore their applications in a variety of fields. A clear picture of the unique properties of the material can be obtained from the collective use of various techniques by probing structural, optical, electrical, and magnetic properties. In the present research work, properties of pristine, doped and electron beam irradiated nanocrystalline $BaWO_4$ are investigated using different techniques. The results are conferred in the following chapters, and this section briefly describes the details of the toolbox for characterizing the synthesized $BaWO_4$ samples.

The thermal stability of $BaWO_4$ samples is studied by thermogravimetric (TG) and differential thermal (DT) analysis. The structural characterization of the $BaWO_4$ samples is done by powder X-ray diffraction (XRD), scanning electron microscopy (SEM), transmission electron microscopy (TEM), Fourier transform infrared (FTIR), and Raman spectroscopy. The composition of the prepared samples is estimated using energy dispersive X-ray analysis (EDX). Optical studies are carried out by UV-visible and photoluminescence (PL) spectroscopy, and electrical studies are carried out by dielectric measurements. The magnetic properties of the synthesized samples are explored by vibrating sample magnetometry (VSM).

2.2. Method of Synthesis

In the present work, pristine and doped $BaWO_4$ nanoparticles are synthesized by the chemical precipitation method. The detailed procedures for the synthesis of the $BaWO_4$ samples are elucidated in the corresponding chapters.

2.3. Thermal Analysis

A series of techniques are available for measuring the temperature dependence of the physical properties of the substances. Here we adopted the thermogravimetric analysis (TGA) and differential thermal analysis (DTA) for this purpose. Thermogravimetric analysis of the sample determines the weight changes of a sample, whereas differential thermal analysis measures the changes in temperature between a sample and a reference as a function of temperature or time. Differential thermogravimetry (DTG) is usually conferred as the derivative weight of the sample with temperature and it gives the most prominent temperature at which a thermal event occurs. All these measurements are primarily used to predict their thermal stability against temperature [1]. Different thermal properties like heat capacities, glass transition temperature, melting, and degradation of macromolecules can be explored by TGA and DTA [2]. In the present work, TG/DT analysis of the sample is carried out using a Perkin Elmer, STA 6000 instrument within a temperature range of 30 − 700 ºC at a heating rate of 20 ºC /min and accuracy of < ± 0.5 ºC.

2.4. Structural Characterization

The structural characterization of the samples is important as it helps to understand the internal structure and morphology of the material at different angles. Different analytical tools used in the present work are XRD, SEM, TEM, EDX, FTIR, and Raman spectroscopy.

2.4.1 Powder X-ray Diffraction Analysis

X-ray diffraction is a powerful non-destructive technique for the characterization of crystalline materials. It provides information on the structure

of the materials, their phase composition, preferred crystal orientations (texture), and other structural parameters, such as average grain size, crystallinity, strain, and crystal defects. In XRD analysis, the regular array of atoms in a crystal can act as a three-dimensional diffraction grating for producing a diffraction pattern. The diffraction pattern is obtained by the superposition of a monochromatic beam of X-rays scattered at specific angles from each set of lattice planes in a sample, which is governed by Bragg's law,

$$2d_{(hkl)}sin\theta = n\lambda \qquad (2.1)$$

Where *d(hkl)* is the inter-planar spacing for the given Miller indices (hkl), 2θ the angle of diffraction or Bragg angle, n the order of diffraction and λ the wavelength of light used [3]. The peak intensities are the characteristics of the distribution of atoms within the crystal lattice. Consequently, the X-ray diffraction pattern is the blotch of periodic atomic arrangements in a given material. The structure and phase identification of the sample is done by matching the peak positions and intensities of the XRD pattern to those in the JCPDS (Joint Committee on Powder Diffraction Standards) database.

The lattice spacing (d) is calculated from the 2θ values of the peaks using the equation (2.1). The lattice parameters are estimated from the lattice spacing of the prominent XRD pattern by using the equation [3],

$$\frac{1}{d^2_{(hkl)}} = \frac{h^2}{a^2} + \frac{k^2}{b^2} + \frac{l^2}{c^2} \qquad (2.2)$$

where *d(hkl)* is the spacing between the planes corresponding to Miller indices h, k, l, and a, b, c are the lattice constants. For a tetragonal structure a=b≠c, hence the above equation becomes,

$$\frac{1}{d^2_{(hkl)}} = \frac{h^2+k^2}{a^2} + \frac{l^2}{c^2} \qquad (2.3)$$

The average crystallite sizes of the samples are estimated using the Scherrer equation [4]

$$D = \frac{k\lambda}{\beta cos\theta} \qquad (2.4)$$

where k (= 0.89) is the crystallite shape factor, λ is the wavelength of the light used, β is the full width at half maximum (FWHM).

The crystallite size and micro-strain on peak broadening of nanoparticles are studied using Williamson-Hall (W-H) analysis, [5] given by,

$$\beta cos\theta = \frac{0.89\lambda}{D} + 4\varepsilon sin\theta \qquad (2.5)$$

where ε is the micro-strain. The variation of 4sinθ against βcosθ is plotted for the nanoparticle samples. From the linear fit to the data, the crystallite size is approximated from the y-intercept and the strain ε from the slope of the fit.

2.4.2 Scanning Electron Microscopy

Scanning electron microscopy is one of the most versatile techniques used for the surface characterization of the samples. Topographic studies, microstructure, chemical analysis, and elemental mapping analysis of a given sample can be obtained using a scanning electron microscope. A JEOL Model JSM-6390LA scanning electron microscope, operating at 20 kV with a resolution of 3 nm was used for obtaining surface micrographs of the $BaWO_4$ samples. It has a specific sample holder where the stub should be fixed containing the sample on the surface [6]. Carbon tape is used for sticking the sample to the stub. A small amount of $BaWO_4$ sample is dispersed in ethanol. A drop of suspension is placed on the carbon tape attached to the stub. It is kept for about 5 to 10 minutes under

the infrared lamp for drying before scanning. After that, the sample-covering stub is fixed in the sample holder and put in the sample-holding chamber or specimen chamber for recording the micrograph.

2.4.3 Energy Dispersive X-Ray Spectroscopy

Energy dispersive X-ray analysis is used to identify the elemental composition of materials through the emitted characteristic X-rays with the principle that each element produces a unique pattern of X-ray lines. This technique is usually used in conjunction with SEM or TEM and is widely used to characterize the microstructural composition and elemental distribution of the sample under study. EDX analysis is performed on a SEM system equipped with EDX attachment. The OXFORD XMX N EDX attachment with JEOL Model JSM-6390LA scanning electron microscope was used for the EDX study of the $BaWO_4$ samples.

2.4.4 Transmission Electron Microscopy

Transmission Electron Microscopy is one of the most powerful techniques in materials science used to characterize the micro and nanostructure of the materials with high resolution. Information about the particle shape, size distribution, crystallinity and interparticle interaction can be obtained from the high magnification imaging produced by the TEM. The TEM in bright field image mode is usually used for producing real space micrographs. The lattice arrangements within crystalline materials can also be visualized by high resolution transmission electron microscopic (HRTEM) images. By analyzing HRTEM images, it is possible to find lattice spacing, orientation and defects of crystalline materials. In addition, a selected area electron diffraction (SAED) pattern can be obtained for a single nanostructure by operating TEM in diffracted mode.

Identification of different crystal planes can be done by analyzing a SAED image [7].

For TEM studies, the $BaWO_4$ powder sample was dispersed in ethanol using an ultrasonic bath. Then the solution was dropped on a copper grid coated with carbon film. For the imaging process, the copper grid containing the sample was placed on a holder after drying. TEM images of the samples were recorded using a JEOL JEM 2100 accelerated by a 200 kV transmission electron microscope with a resolution of 0.23 nm. Further analysis was done by using Image J software. Figure 2.1 shows the photograph of the JEOL model JEM-2100 transmission electron microscope.

Figure 2.1 JEOL model JEM-2100 transmission electron microscope

2.4.5 Fourier Transform Infrared Spectroscopy

FTIR spectroscopy is an indispensable tool in nanomaterial research, which is capable of exploring the material to understand the vibrational motion of atoms and molecules, by identifying the functional groups present in it. The principle is that each molecule only absorbs IR light of certain frequencies based on the characteristic of the molecule. FTIR spectra are recorded in terms of percent transmittance (%T) mode against wavenumber ($1/\lambda$) cm^{-1}. From the characteristic peaks observed in the spectra, different functional groups present in the material can be identified. The FTIR spectra of nanocrystalline $BaWO_4$ samples were measured between 4000 and 400 cm^{-1} using Thermo Nicolet Avtar 370 with a DTGS detector having a resolution of 4 cm^{-1}. Figure 2.2 shows the schematic diagram of the FTIR spectrometer.

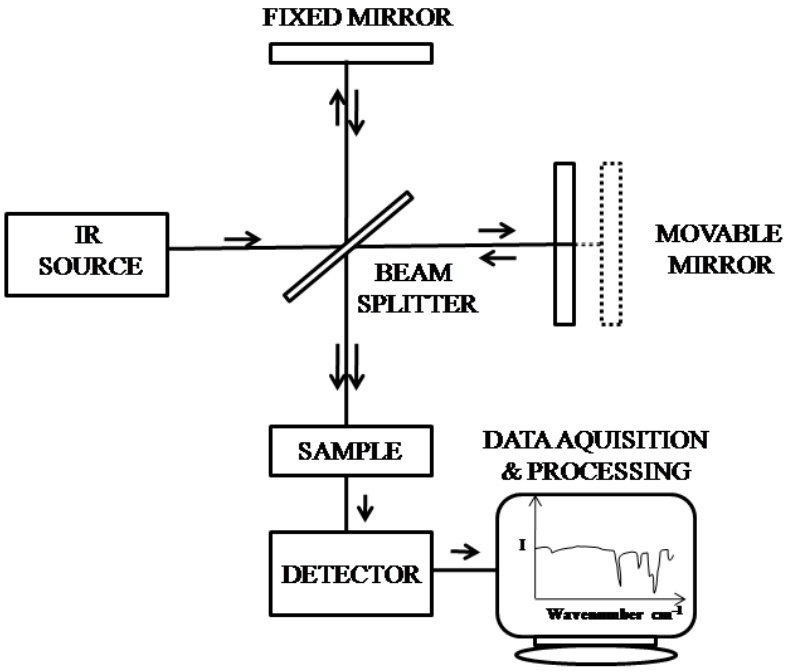

Figure 2.2 Schematic diagram of the FTIR spectrometer

2.4.6 Raman Spectroscopy

Raman spectroscopy is considered to be a complementary technique to IR spectroscopy. A vibration is Raman active only if it changes the polarizability of the molecule. The vibrational, rotational, and other low frequency modes of a system can be investigated by Raman spectroscopy. It is based on inelastic scattering of monochromatic light, usually from a laser. The Raman shift produced is equal to the vibrational level that is involved. Thus, a better understanding of the structural properties of a material can be obtained by examining its Raman spectrum [8]. For the synthesized samples, Raman spectra at room temperature were recorded using a Bruker Raman Spectrometer (RFS-27, using Nd-YAG laser, λ = 1064 nm, operating in the spectral range of 50 − 4000 cm^{-1}).

2.5 Optical Spectroscopic Analysis

Optical spectroscopy generally deals with light-matter interactions, particularly the absorption or scattering of electromagnetic radiation by molecules. The synthesized nanomaterials were optically characterized by UV-visible absorption spectroscopy and photoluminescence spectroscopy.

2.5.1 UV-visible Spectroscopy

Ultraviolet-visible spectroscopy is an efficient tool to get complete information about the optical properties of a given material. A classical semiconductor exhibits nominal optical absorption for photons with energy less than the bandgap and high absorption for photons with energy greater than the bandgap [9]. Here, radiation from the UV to visible range (λ = 200 − 800 nm) is applied to the sample under study. Absorption of UV or visible light

electromagnetic radiation causes electrons to move from lower energy levels to higher energy levels. As a result, there is a sharp increase in absorption at an energy close to the bandgap that manifests itself as an absorption edge (or reflection threshold) in the UV-visible absorption spectrum [10]. The energy absorbed by a material depends on the chemical composition of its constituent species. A reduction in particle size of the sample can lead to the shifting of the absorption edge. The shifting of absorption edge to higher wavelength is known as redshift (Bathochromic shift) whereas towards smaller wavelength is called blueshift (hypsochromic shift).

From Tauc relation [11,12], the direct band gap (Eg) of samples is determined by fitting absorption data to the direct transition equation,

$$\alpha h\nu = E_d\,(h\nu - E_g)^n \qquad (2.6)$$

where α is the optical absorption coefficient, hν the photon energy, Eg the direct bandgap and E_d a constant. Here, 'n' is a constant and n = 1/2 for direct allowed, n = 3/2 for direct forbidden, n = 2 for allowed indirect transition and n = 3 for indirect forbidden transition. The bandgap of the samples can be measured by plotting $(\alpha h\nu)^{1/n}$ as a function of $h\nu$ and extrapolating the linear portion of the curve to absorption equal to zero.

UV-visible absorption spectra of the samples were formulated from reflectance measurements by Kubelka-Munk transformation using a Shimadzu UV–visible spectrophotometer UV 2600 model. For the measurement, the sample holder carrying the powder samples were placed at the entrance port of the integrating sphere. $BaSO_4$ was used as the standard reference material for the calibration of the absorbance scale.

2.5.2 Photoluminescence Spectroscopy

Photoluminescence spectroscopy is a non-destructive technique that is used to study the physical and chemical properties of a given material by using photons to induce excited electronic states (photo-excitation of electrons into permissible excited states). The excess energy is released in the form of optical emission by radiative or non-radiative process and is the difference between the excited and equilibrium states of transition. Qualitative and quantitative information about the chemical composition, structure, impurities, different intrinsic properties, surface defects, and traps produced can be understood by using the PL spectrum of a material. The energy corresponding to the emission peaks is given by,

$$E = h\nu = \frac{hc}{\lambda} \text{ eV} \qquad (2.7)$$

where λ is the wavelength in nm corresponding to the emission peak.

Photoluminescence spectra were measured at room temperature by a Horiba Scientific-Fluoromax 3 spectrophotometer using a 150 W ozone-free xenon arc lamp as the source with a spectral accuracy of 0.5 nm. Figure 2.3 shows the schematic diagram of a photoluminescence spectrophotometer.

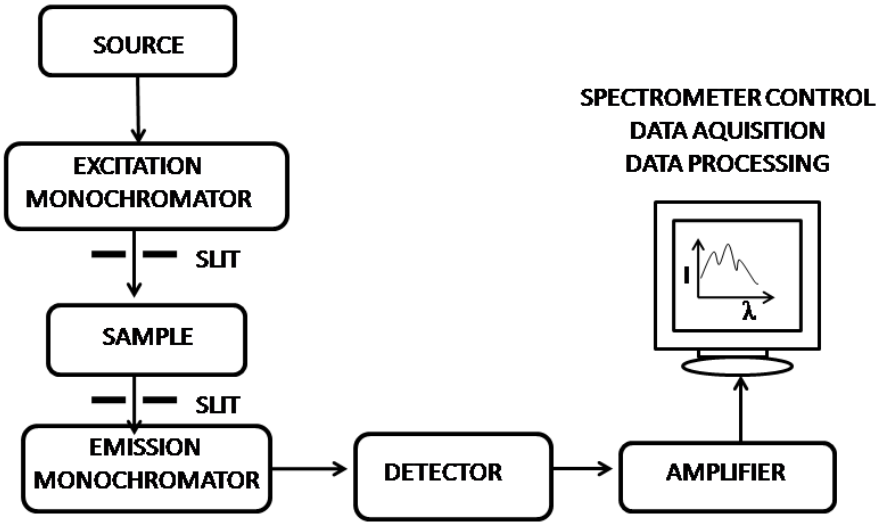

Figure 2.3 Schematic diagram of a PL spectrophotometer

CIE Chromaticity Diagram

The CIE 1931 XYZ colour space was created by the International Commission on Illumination (Commission Internationale de l'Eclairage - abbreviated CIE). The CIE colour space contains both brightness and colour and is based on the colour sensitivity and perception of human eyes. It appears as a curved triangle that contains the full range of visible colours and serves as a standard reference against which, many other colour spaces are defined. In this system, the XYZ tristimulus values can describe any visible colour. The chromaticity of a colour is specified by parameters x and y, which are projective coordinates, and the colours of the chromaticity diagram occupy a region of the real projective plane. Evidently, the diagram uses only two dimensions, which are x and y selected from x, y, and z, where:

$$x = \frac{(X+Y+Z)}{X} \qquad (2.8)$$

$$y = \frac{(X+Y+Z)}{Y} \quad (2.9)$$

$$z = \frac{(X+Y+Z)}{Z} \quad (2.10)$$

$$\text{and } x + y + z = 1 \quad (2.11)$$

In Figure 2.4, white colour surrounds the centre point which has coordinates at about (0.333, 0.333). Also, the x and y axes both range from 0 to 0.8 of chromaticity coordinate values. By drawing a line from the white point through the (x, y) point of the colour space till it coincides, the curve yields the dominant wavelength, λ_D.

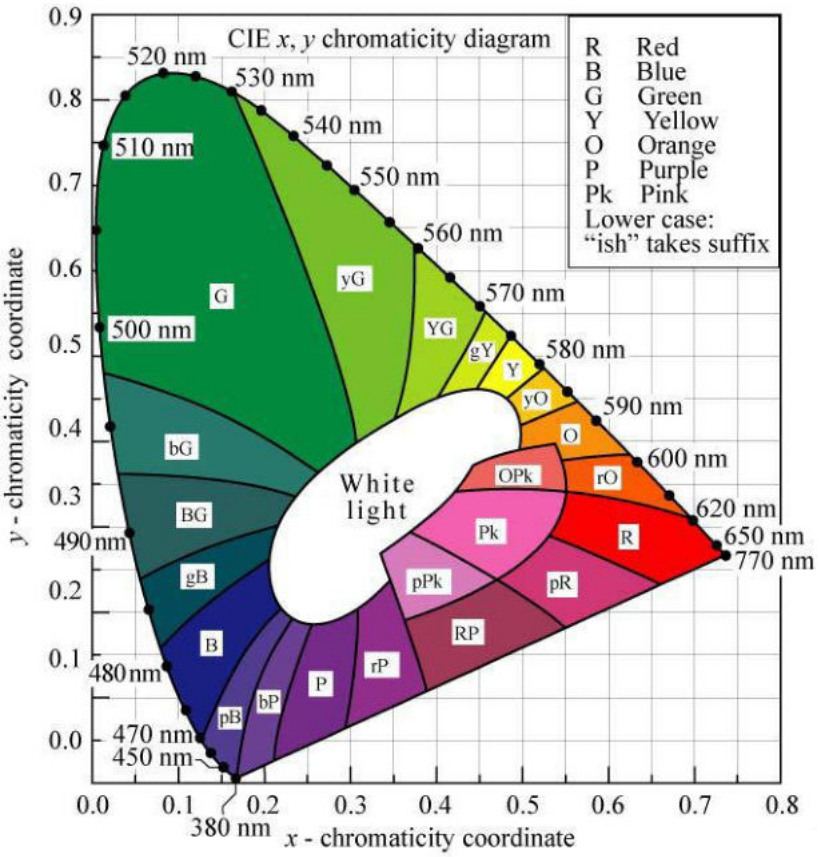

Figure 2.4 1931 CIE chromaticity diagram [13]

2.6 Electrical Studies

To study the electrical properties of the nanocrystalline $BaWO_4$ samples, the nanoparticles were consolidated in the form of cylindrical pellets of diameter 13 mm and thickness 1.2 mm by applying a pressure of ~ 5 tons using a hydraulic press. The pellets prepared were then sintered at 950 ºC.

Dielectric and AC Conductivity Studies

Dielectric measurements as a function of frequency were measured at various selected temperatures. Both the faces of the pellets were coated with a silver paste to ensure conductivity, thereby forming a parallel plate capacitor geometry with the material as the dielectric medium. The capacitance of such a parallel plate capacitor is given by,

$$C = \frac{\varepsilon_0 \varepsilon' A}{d} \qquad (2.12)$$

where A and d are the area and thickness of the pellet, respectively, ε_0 is the permittivity of free space and ε' is the dielectric permittivity of the given sample. Thus, the dielectric permittivity of the samples is calculated using the relation,

$$\varepsilon' = \frac{Cd}{A\varepsilon_0} \qquad (2.13)$$

The loss tangent (tanδ) can be directly obtained from the experimental data. AC conductivity (σ_{ac}) of the sample can be evaluated from the data of dielectric constant (ε′) and loss tangent (tanδ) using the relation,

$$\sigma_{ac} = \varepsilon' \varepsilon_0 \, \omega \, tan\delta \qquad (2.14)$$

where ω is the angular frequency (ω = 2πf, f is the frequency of the applied electric field).

Electrical conductivity is contributed by the migration of charges under the action of an electric field. Conductivity is found to be an increasing function of frequency in the case of hopping conduction and is a decreasing function of

frequency in the case of band conduction. Then the total conductivity (depends on absolute temperature T) can be considered as the sum of both hopping and band conduction. This can be expressed as,

$$\sigma_T = \sigma(T) + \sigma(\omega, T) \quad (2.15)$$

The first term corresponds to band conduction and is found to be frequency independent. Generally, this is taken as dc conductivity (σ_{dc}). Whereas, the second term depends on the frequency and is considered to be the conduction due to hopping [14]. This stands for ac conductivity (σ_{ac}). The variation of σ_{ac} can be expressed by the empirical power law as described by Jonscher and referred to as universal dynamic response as shown below [15,16]

$$\sigma(\omega, T) = \sigma_{ac} = A\omega^n \quad (2.16)$$

Here, $\omega = 2\pi f$ is the angular frequency of the applied electric field, A is a constant and n is the frequency exponent. The constants A and n depend on both temperature and compositions. The frequency exponent n varies between zero and unity. The value of n can be determined by measuring the slope of the log-log plot between σ_{ac} and ω.

Dielectric and ac conductivity measurements were carried out using an impedance analyzer (Wayne Kerr H-6500B model) in conjunction with a portable furnace and temperature controller (±1 ^{o}C). Usually by using impedance analyzers, one measures capacitance C(ω) of the cell filled with the given dielectric and the loss tangent. The basic measurement accuracies for capacitance and loss tangent values are ±0.05% and ±0.0005% respectively. The temperature, frequency, and compositional dependence of dielectric permittivity, loss tangent, and ac conductivity were investigated for all the samples. The photo image of the Wayne Kerr impedance analyzer (6500B) used in the present work is shown in Figure 2.5.

Figure 2.5 Wayne Kerr impedance analyzer (6500B)

2.7 Vibrating Sample Magnetometry

Vibrating sample magnetometer, based on Faraday's law, according to which an emf is induced in a conductor by a time varying magnetic flux is used for the magnetic studies of the samples [17]. The change in the magnetic field can be determined by measuring the electric field.

Figure 2.6 shows the schematic diagram of the VSM arrangement. The magnetic sample is placed in a steady magnetic field produced by a pair of electromagnets. The vibration of the sample with respect to the stationary pick up coils induces a voltage in the pick-up coils, which is proportional to the magnetic moment of the sample. The induced voltage is measured using a lock-in amplifier. The magnetic moment of the sample can be estimated by feeding the signals from the pick-up coils and the reference signal from the sample holder.

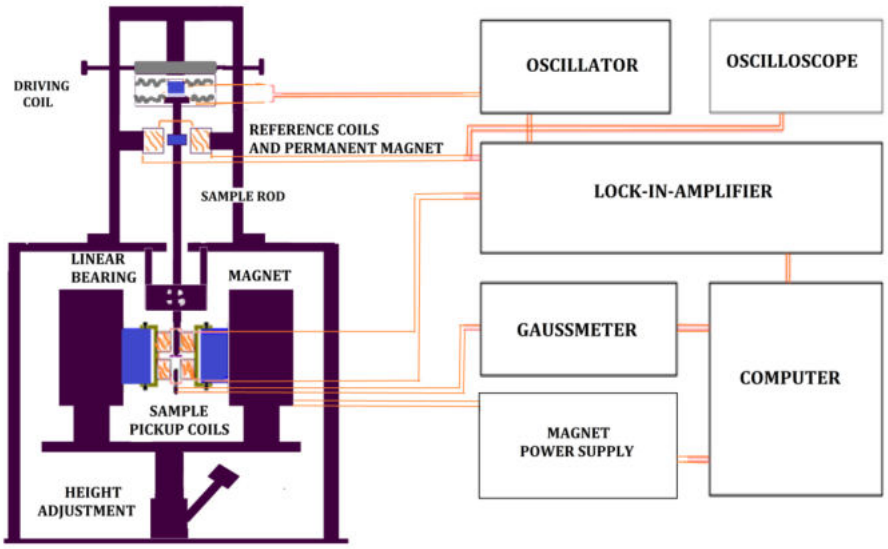

Figure 2.6 Schematic arrangement of VSM

The magnetic measurement of the $BaWO_4$ nanocrystal samples was done at room temperature using Lakeshore VSM 7410 with a maximum field of 15 kOe.

2.8 Electron beam irradiation

The powder sample is exposed to different doses of an electron beam (EB) from a variable energy Microtron. The properties of the bare and electron irradiated samples are compared to draw important conclusions on the effects of electron beam irradiation.

In this investigation, powder samples were taken in polythene covers and irradiated at different electron doses using an 8 MeV variable energy Microtron facility at the Mangalore University, Mangalagangotri, India. This Microtron has a maximum pulse current of 50 mA and a pulse rate of 50 Hz. An image of this Microtron is shown in Figure 2.7.

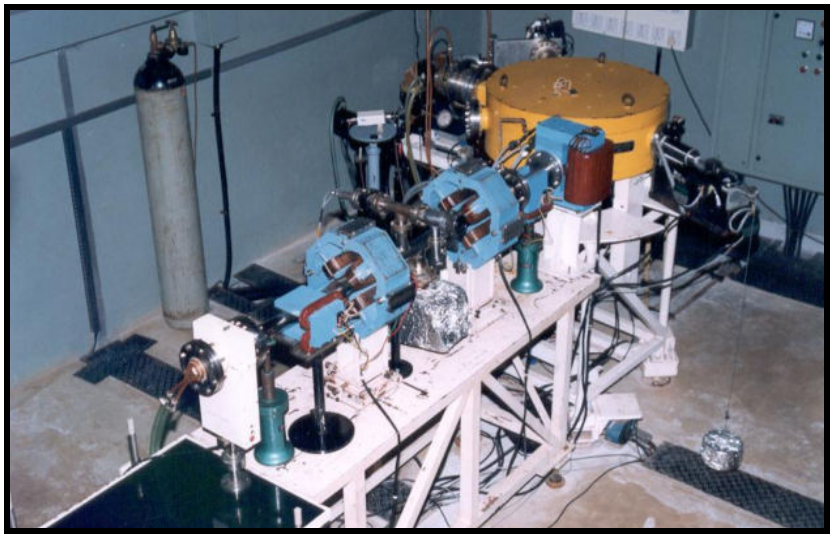

Figure 2.7 8 MeV Microtron at Mangalore University

The samples are exposed to the electron beam at a distance of 30 cm from the exit port. The dose is uniform over an area of 8×8 cm^2, as determined by the dosimetry.

References

[1] A.W. Coats, J.P. Redfern, Thermogravimetric analysis. A review, Analyst, 88 (1963) 906-924.

[2] R. Bud. D.J. Warner, Instruments of science: An historical encyclopedia., Taylor & Francis, 1998.

[3] B.D. Cullity, Elements of X Ray diffraction, Addison-Wesley, Reading, 1967.

[4] T. Varghese, K.M. Balakrishna, Nanotechnology: An introduction to synthesis, properties and applications of nanomaterials, Atlantic Publishers, 2011.

[5] G.K. Williamson, W.H. Hall, X-Ray broadening from filed aluminium and wolfram, Acta Metall. 1 (1953) 22–31.

[6] K. Akhtar, S.A. Khan, S.B. Khan, A.M. Asiri, Scaning Electron Microscopy: Principle and Applications in Nanomaterials Characterization In: S. Sharma, Handbook of Materials Characterization, Springer, 2018.

[7] M. Born, E. Wolf, A. Bhatia, P. Clemmow, D. Gabor, A. Stokes, W. Wilcock, Principles of Optics: Electromagnetic Theory of Propagation, Interference and Diffraction of Light, 7th ed., Cambridge University Press, 1999.

[8] F. Marabelli, P. Wachter, Covalent insulator CeO_2: Optical reflectivity measurements, Phys. Rev. B. 36 (1987) 1238–1243.

[9] H. Wang, P.K. Chu, Surface Characterization of Biomaterials, Elsevier, 2013.

[10] S.H. Mohamed, M. El-Hagary, A.S. Radwan, Preparation and characterization of mixed iron-titanium oxide nanostructure, Indian J. Phys. 87 (2013) 223–228.

[11] J. Tauc, Amorphous and liquid semiconductors, Springer, 1974.

[12] J. Tauc, A. Menth, States in the gap, J. Non. Cryst. Solids. 8–10 (1972) 569–585.

[13] S. Gage, Optoelectronics Applications manual, McGraw Hill, 1977.

[14] M.A. El Hiti, AC electrical conductivity of Ni - Mg ferrites, J. Phys. D Appl. Phys. 29 (1996) 501–505.

[15] A.K. Jonscher, Dielectric relaxation in solids, J. Phys. D Appl. Phys. 32 (1999) R57.

[16] B.M. Greenhoe, M.K. Hassan, J.S. Wiggins, K.A. Mauritz, Universal power law behavior of the AC conductivity versus frequency of agglomerate morphologies in conductive carbon nanotube-reinforced epoxy networks, J. Polym. Sci. Part B Polym. Phys. 54 (2016) 1918–1923.

[17] B.D. Cullity, C.D. Graham, Introduction to Magnetic Materials, 2nd ed., Wiley, 2011.

Chapter 3

EFFECT OF CALCINATION TEMPERATURE ON THE PROPERTIES OF NANOCRYSTALLINE $BaWO_4$

The synthesis of nanocrystalline $BaWO_4$ by chemical precipitation method and the effect of calcination temperature on the structural, optical, magnetic and electrical properties of the synthesized sample are discussed in this chapter.

3.1 Introduction

Nanocrystalline barium tungstate has widespread attention due to its novel structural, electrical, optical, and magnetic properties. To explore the potential of $BaWO_4$, a deeper insight into its structure and properties are needed. A systematic and detailed analysis of the effect of calcination temperature on the structural, optical, magnetic, and electrical properties of the nanocrystalline $BaWO_4$ samples synthesized by the chemical precipitation method is discussed in this chapter.

The thermal stability of the synthesized sample is investigated using thermogravimetric and differential thermal analysis. The structural characterization of the $BaWO_4$ samples is done using X-ray diffraction, Scanning electron microscopy, Transmission electron microscopy, Fourier transform infrared spectroscopy and Raman spectroscopy. The quantitative compositional

information is obtained from energy dispersive X-ray analysis. The optical properties of the $BaWO_4$ samples are studied using UV-visible and photoluminescence spectroscopic methods. The magnetic behaviour of the sample is investigated using a vibrating sample magnetometer. The electrical property of the sample is elucidated by the dielectric and AC conductivity measurements.

3.2 Synthesis of nanocrystalline $BaWO_4$

Barium nitrate $Ba(NO_3)_2$ (99%, Merk) and sodium tungstate ($Na_2WO_4.2H_2O$) (98%, Merk) are used without further purification for the synthesis of pristine $BaWO_4$. Nanocrystalline $BaWO_4$ powder samples are successfully prepared by direct chemical precipitation method without using any surfactant, templates, or catalyst.

0.1 M solutions of barium nitrate and sodium tungstate are prepared by dissolving the desired quantity of them in distilled water. The Na_2WO_4 solution is added to $Ba(NO_3)_2$ solution drop by drop by stirring continuously. The solution is stirred well for about 30 min by using a magnetic stirrer at room temperature. The white precipitate is allowed to settle down for 3 h and is collected by the decantation of the supernatant liquid. The obtained precipitate is washed well with distilled water several times to remove the unreacted reagents and sodium nitrate formed. The product is dried in a hot air oven at 80 ºC for about 24 h. The dried sample is pulverized well in order to get fine powder samples. The obtained powder samples are calcined at 400, 550, and 700 $^{\circ}$C for 3 h in a muffle furnace [1]. The $BaWO_4$ samples calcined at 400, 550, and 700 ºC are denoted as **S1**, **S2,** and **S3**, respectively. A schematic representation of the synthesis of nanocrystalline $BaWO_4$ is shown in Figure 3.1.

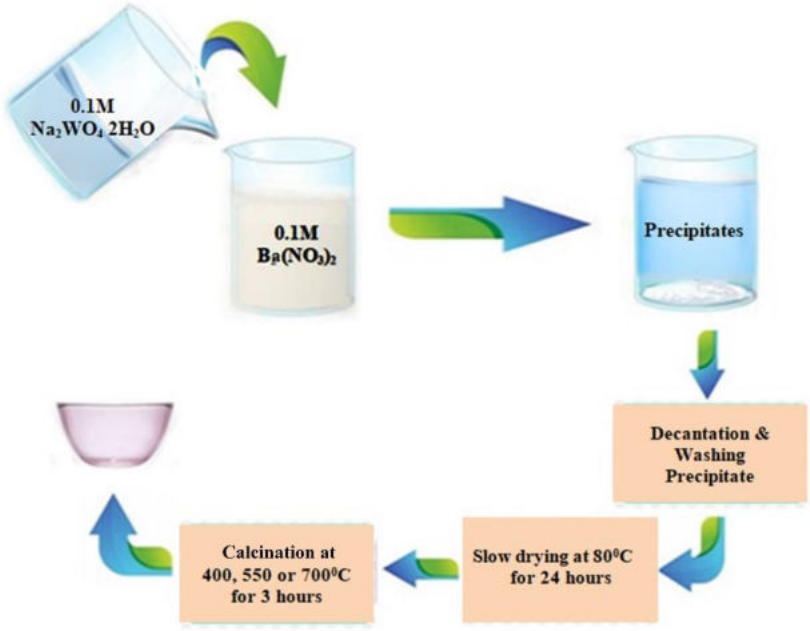

Figure 3.1 The scheme of preparation of nanocrystalline $BaWO_4$

3.3 Results and Discussion

3.3.1 Thermal Analysis

The selection of suitable calcination temperatures is done from the thermal analysis of the synthesized $BaWO_4$ powder. Figure 3.2 shows the thermal decomposition results of the precursor from the ambient temperature to 700 ℃ using both the TG and DTG curves. A 1% weight loss occurs in the temperature range from 10 to 310 ℃. This is due to the loss of surface water on the particles, and the combustion of minor impurities present in the sample. DTA curve is an exothermic curve, and it confirms the combustion of the minor impurities present in the sample. Since the TG curve remains almost constant above 310 ℃, temperatures 400, 550, and 700 ℃ are selected as the calcination temperatures.

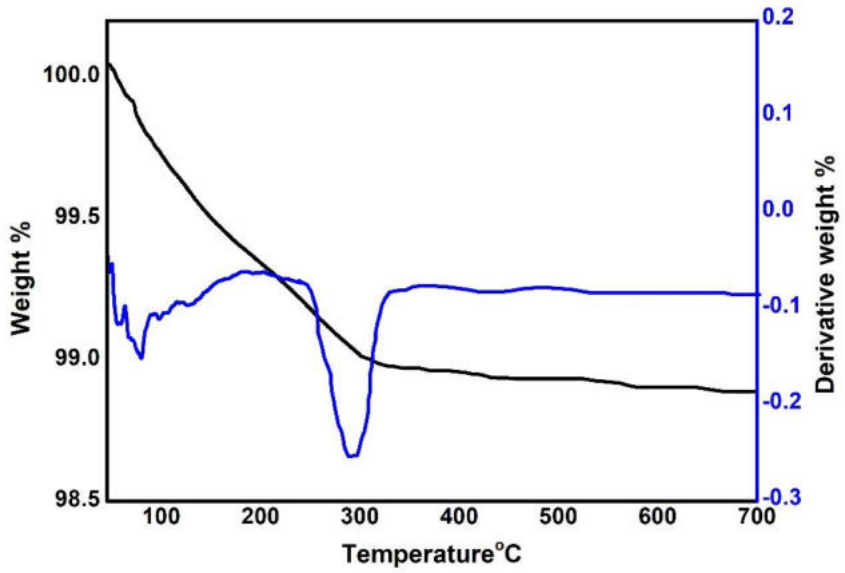

Figure 3.2 TG/DTG curves of $BaWO_4$ samples

3.3.2 Structural Characterization

The structural characterization of the synthesized $BaWO_4$ powder is carried out by following the procedure described in *Section 2.4*.

3.3.2.1 Powder XRD Analysis

The phase purity, crystallinity and structure of the $BaWO_4$ powder samples are examined using the XRD technique. Figure 3.3 shows the XRD patterns of the samples calcined at different temperatures collected using Brucker D8 Advance X-ray diffractometer ((λ=1.5406 Å, step size=0.02º and step time 29.1s) with CuKα radiation in 2θ range from 10 to 80º. Well defined diffraction peaks with preferential orientation along the plane (112) are observed for all the samples, confirming their crystalline nature. The peaks corresponding to (101), (112),

(004), (200), (211), (204), (220), (116), (132), (224), (400), (208), (316), (413), (404), (240), (228), and (110) planes can be indexed to the body-centred tetrahedral scheelite structure (space group $I4_1/a$) of $BaWO_4$. The pattern agrees well with the JCPDS file No. 72-0746 of $BaWO_4$. No additional peaks are observed, confirming the purity of the obtained product.

Figure 3.3 shows that the full width at half maximum (FWHM) of the diffraction peaks of the samples gradually decreases with the increase in calcination temperature. This is because, at higher calcination temperature, the formed crystallites are large, which can be attributed to the thermally promoted crystallite growth [2]. The average crystallite sizes of the samples are calculated from the line broadening of the diffraction peaks using Scherrer equation [3,4]. The average crystallite size and the microstrain of the samples were also analysed using Williamson-Hall method (Figure 3.4) [5]. The cell parameters of the samples are calculated using the plane spacing equation for tetragonal structure group [6] from the XRD data. The average crystallite size and the cell parameters are displayed in Table 3.1.

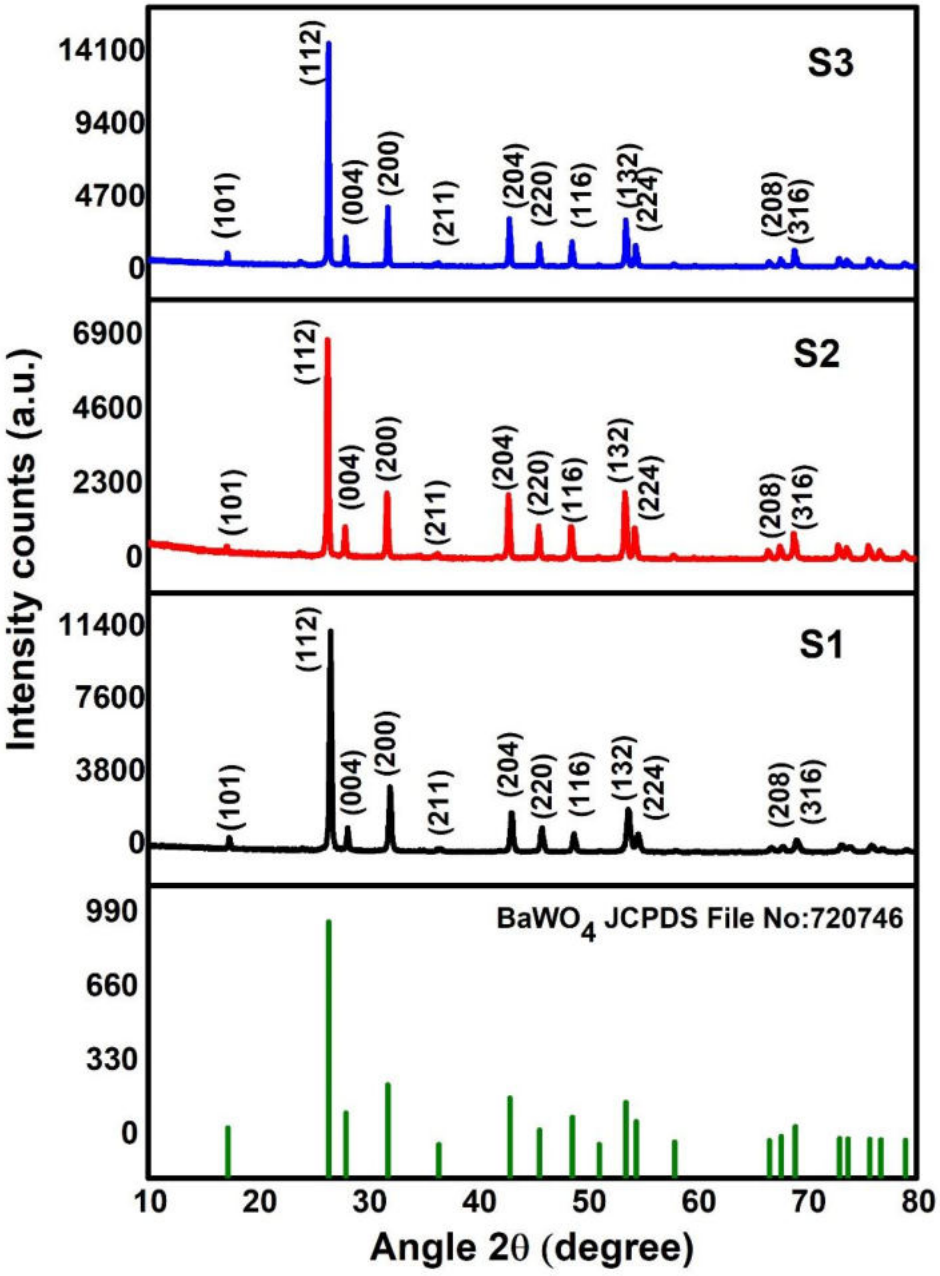

Figure 3.3 XRD patterns of $BaWO_4$ samples

Table 3.1 Geometric parameters of $BaWO_4$ samples

Sample	a = b (Å)	c (Å)	Unit cell volume ($Å^3$)	Crystallite size (nm)		Micro-Strain $\times10^{-3}$
				Scherrer method	W-H method	
S1	5.589	12.658	395.45	13.15	14.56	0.149
S2	5.652	12.757	403.58	13.38	14.83	0.113
S3	5.616	12.731	401.52	19.17	19.05	0.109

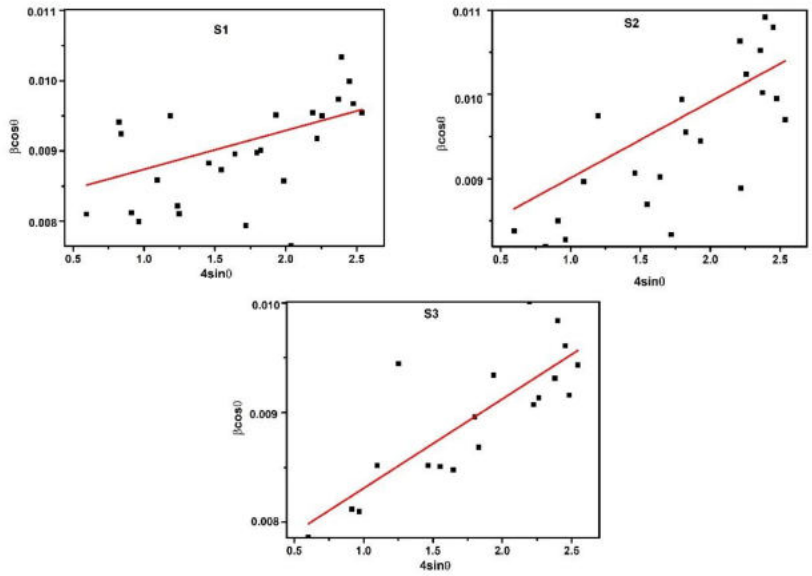

Figure 3.4 Williamson-Hall plots of $BaWO_4$ samples

Rietveld refinement of the samples is also done to investigate the effect of calcination temperature on the structural parameters of the $BaWO_4$ lattice (Figure 3.5). Double Voigt is used for profile fitting. All the refinement results indicated that the samples have a pure scheelite-type tetragonal phase with space group $I4_1/a$ (88) and point group symmetry C^6_{4h}. Refined parameters of the $BaWO_4$ samples are shown in Table 3.2.

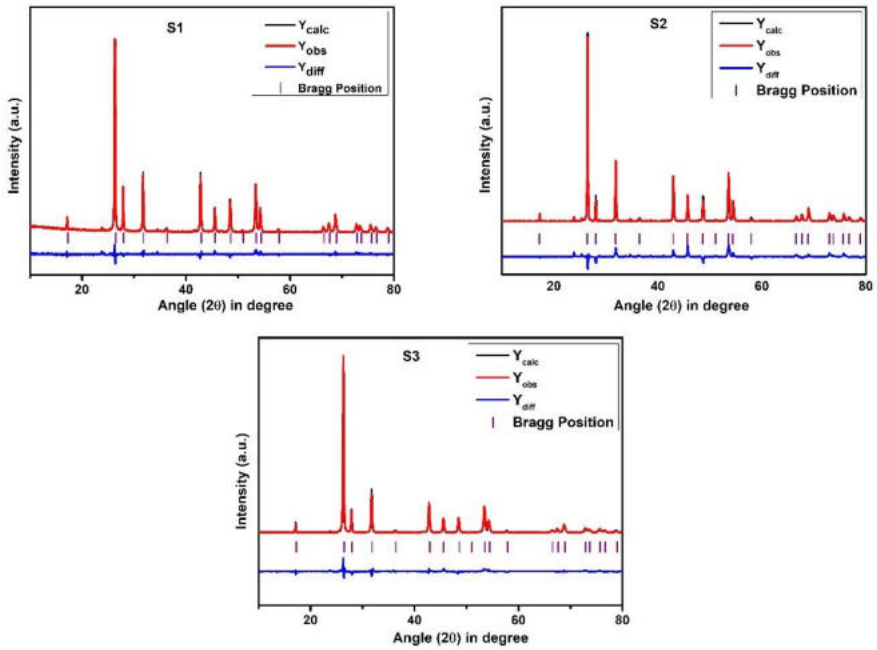

Figure 3.5 Observed, calculated and the difference XRD patterns of $BaWO_4$ Samples

Table 3.2 Structural parameters and refined data of the $BaWO_4$ samples

$BaWO_4$ Sample	Atoms	x	y	z	a=b	c	Unit cell volume	R_{wp}	R_p	R_e	GOF
S1	Ba	0.0000	0.2500	0.6250	5.6213	12.7414	402.62	9.71	7.38	6.66	1.45
	W	0.0000	0.2500	0.1250							
	O	0.1259	0.0056	0.2097							
S2	Ba	0.0000	0.2500	0.6250	5.6372	12.7635	405.59	9.67	7.54	6.32	1.53
	W	0.0000	0.2500	0.1250							
	O	0.1240	0.0142	0.2086							
S3	Ba	0.0000	0.2500	0.6250	5.6264	12.7464	403.50	9.21	6.94	6.42	1.43
	W	0.0000	0.2500	0.1250							
	O	0.1157	0.0121	0.2186							

3.3.2.2 SEM and EDX Analysis

Figure 3.6 depicts the SEM images of the $BaWO_4$ samples calcined at different temperatures. The SEM micrograph represents the topography and surface morphology of the highly agglomerated $BaWO_4$ particles with voids. The morphology of the samples changes with the calcination temperature. Different structures such as bipyramidal, corn-like and flower-like structures are seen in the SEM images. The sample **S1** appears to have a spongy nature with granular like morphology. However, samples **S2** and **S3** exhibit popcorn and flower-like structure respectively. As the calcination temperature increases, the surface becomes smooth and the agglomeration increases, and hence the particle size increases. The obtained microstructures of $BaWO_4$ samples are not in uniform size and shape.

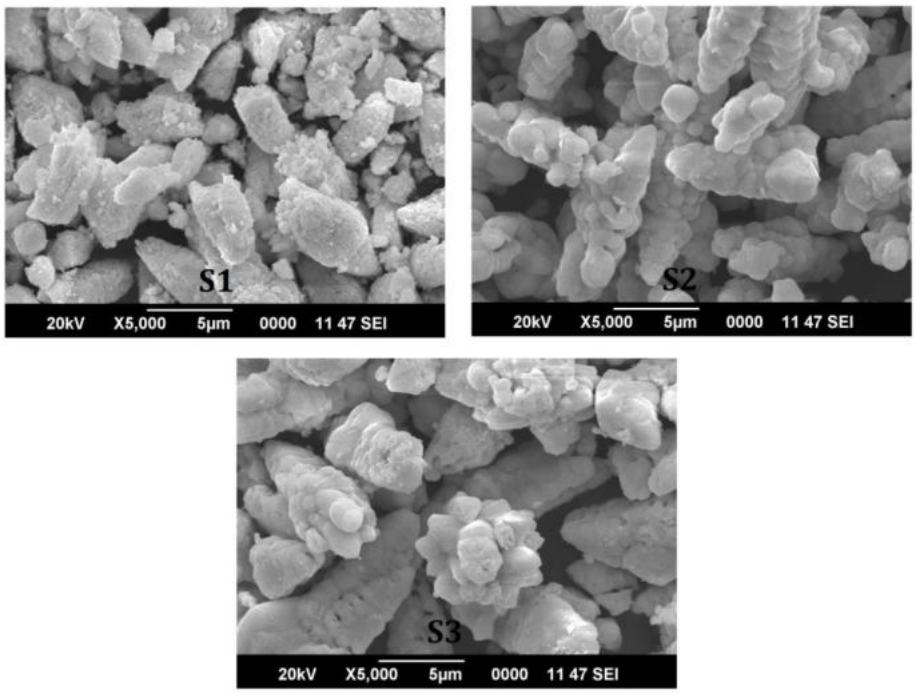

Figure3.6 SEM images of $BaWO_4$ samples

EDX is an analytical technique for the elemental analysis or chemical characterization of the as-prepared samples. The EDX spectrum of the $BaWO_4$ samples are is shown in Figure 3.7. The spectrum clearly shows the co-existence of barium, tungsten and oxygen in the samples in stoichiometric ratios. The average mass and atomic percentages of the sample taken from different regions are presented in Table 3.3.

Table 3.3 Elemental composition of $BaWO_4$ sample

Sample	El	AN	Series	Mass% [wt%]	Atom [at.%]
S1	W	74	L-series	51.03	16.53
	Ba	56	L-series	30.05	13.03
	O	8	K-series	18.92	70.43
S2	W	74	L-series	49.63	15.48
	Ba	56	L-series	30.31	12.66
	O	8	K-series	20.06	71.87
S3	W	74	L-series	49.18	15.43
	Ba	56	L-series	30.96	13.00
	O	8	K-series	19.85	71.57

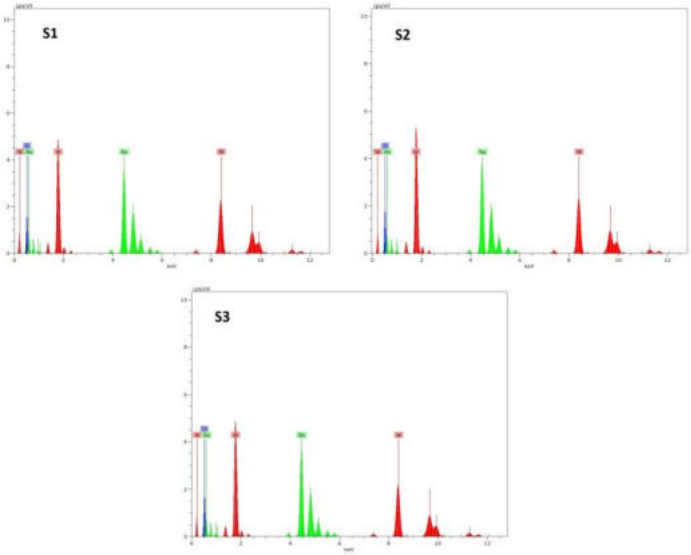

Figure 3.7 EDX pattern of $BaWO_4$ samples

3.3.2.3 TEM Analysis

TEM bright field image and SAED patterns of the $BaWO_4$ samples are recorded for analyzing the morphology and size of the synthesized products. Figure 3.8 shows the TEM bright field images, HRTEM images and the selected area electron diffraction patterns of the $BaWO_4$ samples. It can be seen that the particles have an almost spherical or oval shape and are found to be agglomerated. The interplanar distances measured from HRTEM images match with planes (200), (213) and (211) respectively for the samples **S1**, **S2**, and **S3**. Strong bright spots can be seen in the SAED pattern, which represent the crystalline nature of the samples. The electrons reflected and diffracted from the different crystallographic planes of the unit cells of $BaWO_4$ produce these bright spots [7]. The ring pattern observed in the SAED pattern indicates the polycrystalline nature of the sample.

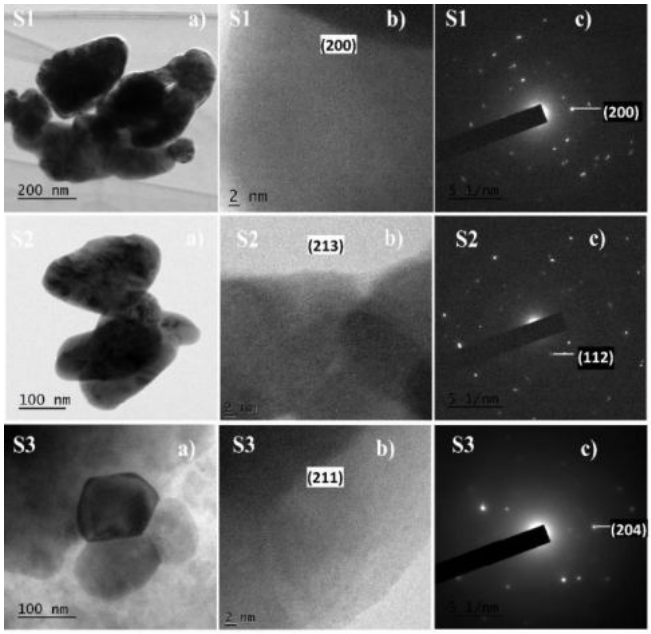

Figure 3.8 a) TEM bright field images b) HRTEM images c) SAED patterns of the $BaWO_4$ samples

3.3.2.4 FTIR Analysis

FTIR spectra of the $BaWO_4$ samples in the transmitted mode are recorded at room temperature to confirm the phase formation and purity of the samples, and are shown in Figure 3.9.

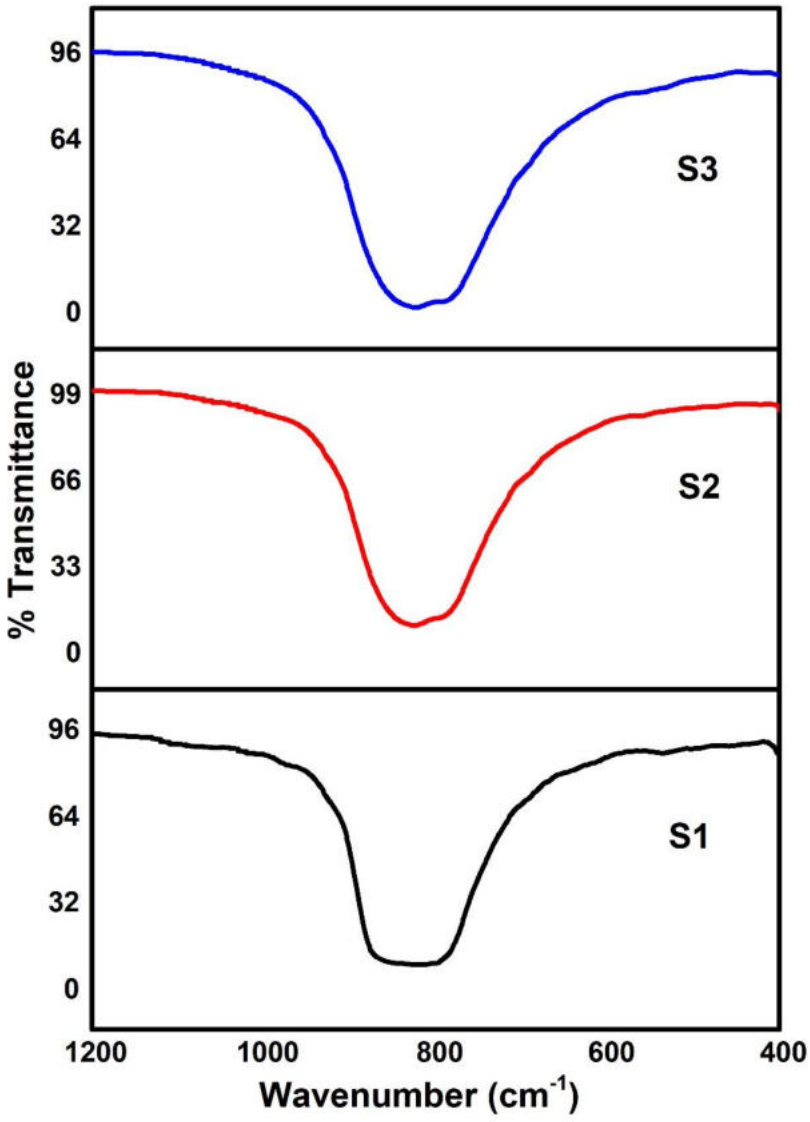

Figure 3.9 FTIR spectra of $BaWO_4$ samples

Since $BaWO_4$ has tetrahedral symmetry only, F2(ν3,ν4) modes are infrared active. The absorption peak at 403 cm^{-1} can be assigned to F2(ν4) vibration which represents the bending vibration of W-O. The broad intense peak centred around 820 cm^{-1} corresponds to the antisymmetric stretching vibration F2(ν3) originating from the W-O in the WO_4^{2-} tetrahedron [8]. Like PXRD studies, FTIR analysis also confirms the tetragonal structure of $BaWO_4$ lattice and the absence of any secondary phase.

3.3.2.5 Raman Analysis

Raman spectroscopy is an important tool in obtaining the structural information of the $BaWO_4$ samples. The Raman spectra verify the rotational, vibrational and other low-frequency modes of the system. From group theory, there are 26 vibrations for the scheelite tetragonal $BaWO_4$, which is represented by the equation [9],

$$\Gamma = (3Ag+3Bu) + (5Bg+5Au) + (5Eg+5Eu) \qquad (3.1)$$

where all the A_g, B_g, and E_g modes, are Raman active, which arise from the same motion of the scheelite $BaWO_4$. Both A and B modes are non-degenerate, whereas E modes are doubly degenerate. The subscript *g* for even and *u* for odd parity indicate the parity under inversion in centrosymmetric crystals. In scheelites, the even pair of members (g) is Raman active, 4Au and $4E_u$ modes are IR active, the remaining $1A_u$ and $1E_u$ modes are acoustic, and the $3B_u$ are silent modes [10,11]. The expected 13 zone centred Raman active modes are given by the equation [12,13],

$$\Gamma = 3A_g + 5B_g + 5E_g \qquad (3.2)$$

According to the literature, out of the 13 Raman active phonons, 7 are internal modes, in which the centre of mass is stationary and the vibrations are confined in the $[WO_4]^{2-}$ tetrahedron with cubic point symmetry T_d and six are external modes consisting of two rotational modes and four translational modes [12,13]. The lattice phonons from the external mode of vibration consist of the motion of the Ba^{2+} cation and the rigid $[WO_4]^{2-}$ molecular units.

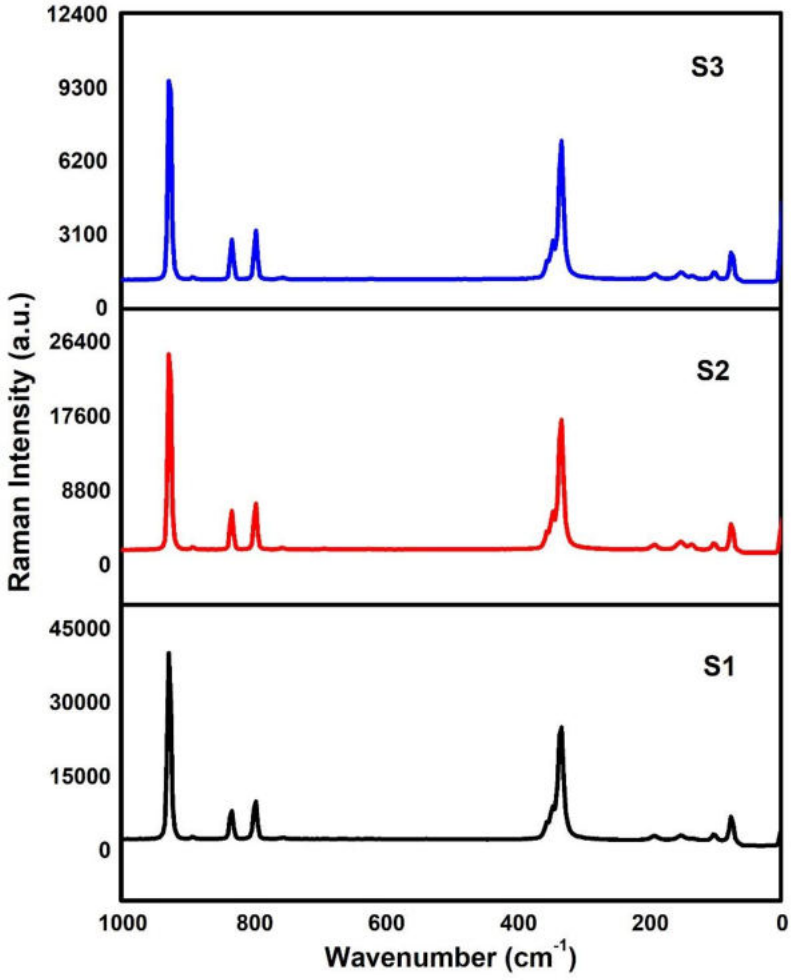

Figure 3.10 Raman spectra of $BaWO_4$ samples

Raman spectra of the $BaWO_4$ samples **S1**, **S2,** and **S3** are shown in Figure 3.10. Of the 13 expected Raman modes, 10 modes are observed. The theoretical and experimental modes observed are shown in Table 3.4.

Table 3.4 Comparison of Raman active modes of $BaWO_4$ samples with literature values

Peak/ mode	Value of ω in cm^{-1}						
	Theoretical [12]	Present values			Ref. [14]	Ref. [15]	Ref. [16]
		S1	**S2**	**S3**			
T(Bg)	55	-	-	-	-	63	62
T(Eg)	81	75.08	75.01	75.08	-	75	74
T(Eg)	110	101.73	101.32	101.29	-	102	104
T(Bg)	145	150.60	151.08	151.93	-	133	132
R(Ag)	149	-	-	-		150	150
R(Eg)	209	191.47	191.97	191.47	272	191	191
ν2(Ag)	328	332.30	332.39	332.30	330	331	-
ν2(Bg)	329	332.30	332.39	332.30	-	333	332
ν4((Bg)	339	345.62	344.83	346.07	-	345	345
ν4(Eg)	348	354.95	354.43	354.51	-	355	353
ν3(Eg)	797	796.09	796.13	796.09	797	794	796
ν3(Bg)	823	831.63	832.25	831.63	829	831	830
ν1(Ag)	928	928.03	927.34	927.59	924	925	925

In the table, ν_1, ν_2, ν_3, ν_4 represent the internal mode of vibrations, R and T represent the rotational and translational mode of vibrations respectively. The internal modes with a frequency above 300 cm^{-1} are due to the high frequency stretching vibrations $\nu_1(A_g)$, $\nu_3(B_g)$, and $\nu_3(E_g)$; the medium frequency bending vibrations $\nu_2(A_g)$ and $\nu_2(B_g)$, and $\nu_4(B_g)$ and $\nu_4(E_g)$. It is found that maximum shift is observed for Raman vibration modes for sample **S2** which has the highest unit cell volume, and the experimental values observed are in agreement with the reported values. These results indicate that the methods employed here are

suitable to produce $BaWO_4$ materials with a reasonable degree of short-range order. The intensity and width of the Raman modes decrease as the calcination temperature increases. This may be due to the change in the surface morphology of the samples.

3.3.3 Optical Properties

UV-visible absorption spectroscopy and photoluminescence spectroscopy are the techniques used to explore the optical properties of the synthesized $BaWO_4$ samples. Optical analyses are carried out by following the procedure given in *Section 2.5.*

3.3.3.1 UV-visible Analysis

Diffuse reflectance spectra of the $BaWO_4$ powder samples is taken to study the optical absorption properties of the prepared samples. The optical absorption coefficient is obtained by using the Kubelka-Munk transformation equation. The optical absorption spectra of the samples is shown in Figure 3.11. The optical absorption spectra are observed in the ultraviolet region (220 nm) corresponding to the ligand to metal charge transfer transition inside the WO_4^{2-} anion [17]. By absorbing the ultraviolet radiation, the excitation from O_{2p} to W_{t2g} in the $(WO_4)^{2-}$ group takes place. Because of the strong interactions between the hole on the oxygen and the electron on the tungsten, they remain together as an exciton in the excited state [17]. The absorption peaks corresponding to the samples **S1**, **S2**, and **S3** are at 220, 224 and 223 nm respectively, which are close to the reported value of 223 nm [14]. The small redshift observed with the increase in calcination temperature is due to the variation in particle size upon calcination.

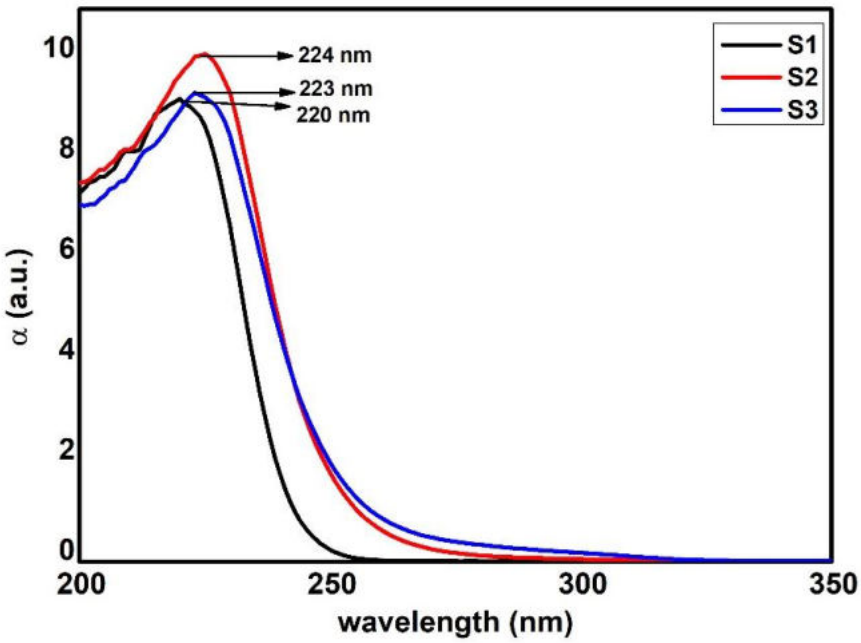

Figure 3.11 Optical absorption spectra of $BaWO_4$ samples

The $BaWO_4$ is a direct bandgap semiconductor material [18]. The optical bandgap of the $BaWO_4$ samples is estimated by taking n = 2 in the Tauc relation as discussed in section 2.5.1. Figure 3.12 shows the $(\alpha hv)^2$ versus hv graphs (Tauc plots) of the samples **S1**, **S2,** and **S3**. The optical bandgap values obtained for the samples **S1**, **S2**, and **S3** are 5.25, 5.14, and 5.13 eV respectively. The bandgap of the samples is found to be slightly greater than the reported value of 4.6 eV [19]. The results show a slight decrease in the bandgap with the increase in calcination temperature.

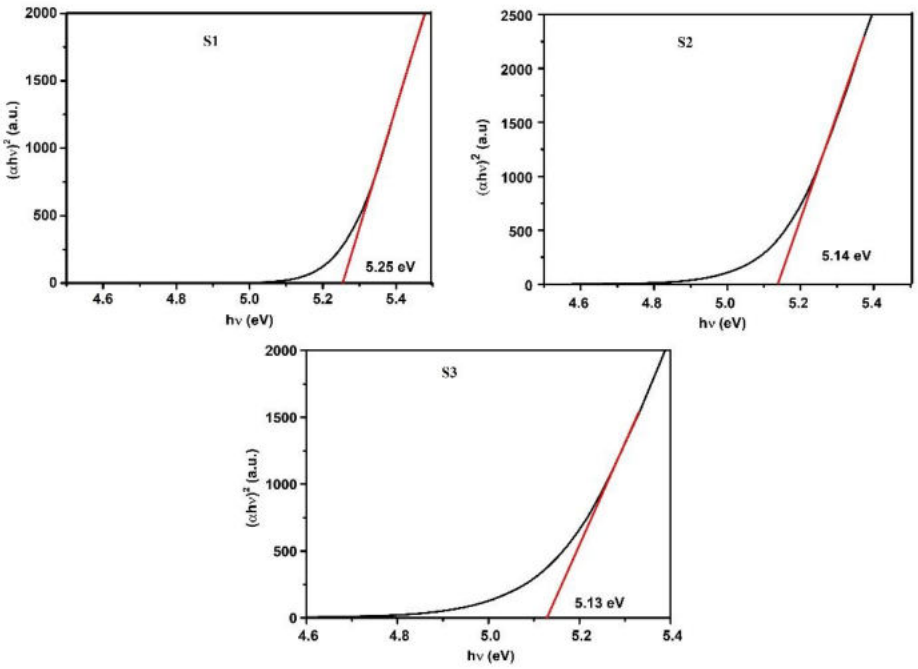

Figure 3.12 Tauc plots of $BaWO_4$ samples

3.3.3.2 Photoluminescence Studies

PL emission spectra of the $BaWO_4$ samples at room temperature are measured at an excitation wavelength of 350 nm. Figure 3.13 shows the photoluminescence emission spectra of the $BaWO_4$ samples. All the spectra show a broad feature, which extends from 370 to 600 nm with peaks at 435 nm. The broad photoluminescence spectra of the $BaWO_4$ samples indicates that the emission involves a multiphonon process [20]. In WO_4 tetrahedron, hybridization between W5d and O2p orbitals is indicated as covalent bonding between the ions. The PL emission is due to the de-excitation of self-trapped excitons of the $[WO_4]^{2-}$ [21]. The broad emission peaks correspond to the transition from the degenerate $^3T_1$ ($4d/5d^0$ – $W^{6+}/2p^6$- O^{2-} state) excited state to the $^1A_1$ ($4d/5d^1$ - $W^{5+}/2p^5$- O^- state) ground state [7,22]. The splitting of $^3T_1$ is due to the lowering

of crystal field symmetry from T_d and due to the inclusion of spin-orbit interaction. The transition $^3T_1$ to $^1A_1$ is spin forbidden, but it is made allowed by the spin-orbit interaction [18]. The splitting of energy levels of WO_4^{2-} in $BaWO_4$ is schematically depicted in Figure 3.14. The corresponding absorption transition is not observed in the excitation spectrum due to the strong spin selection rule [23]. The tail of the luminescence spectrum extends to the green region which may be due to the lattice distortions or the oxygen vacancy present in the samples [19]. The PL intensity of the $BaWO_4$ sample is found to change with an increase in calcination temperature. The variation in particle size with an increase in the calcination temperature may be the reason for the change in the intensity of the photoluminescence spectra [24].

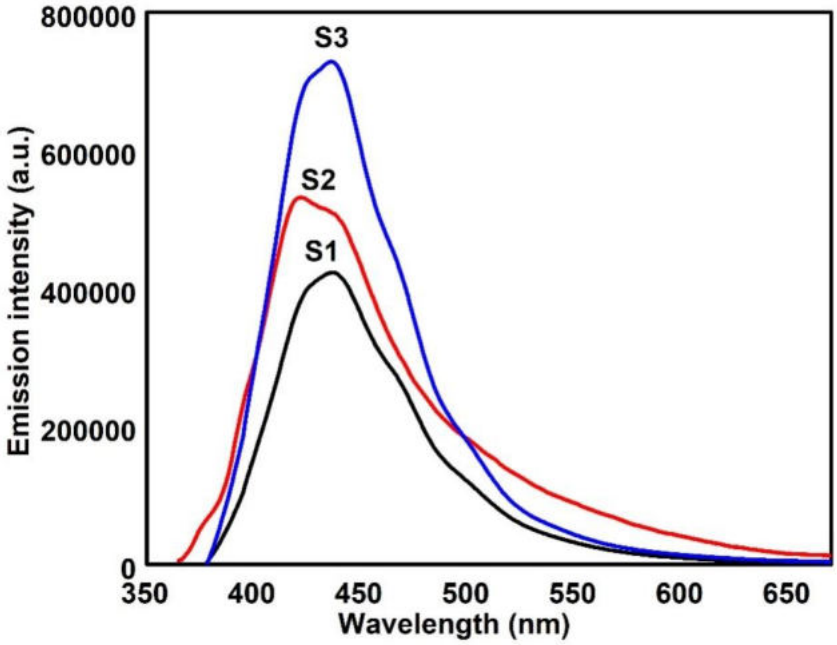

Figure 3.13 Photoluminescence spectra of $BaWO_4$ samples

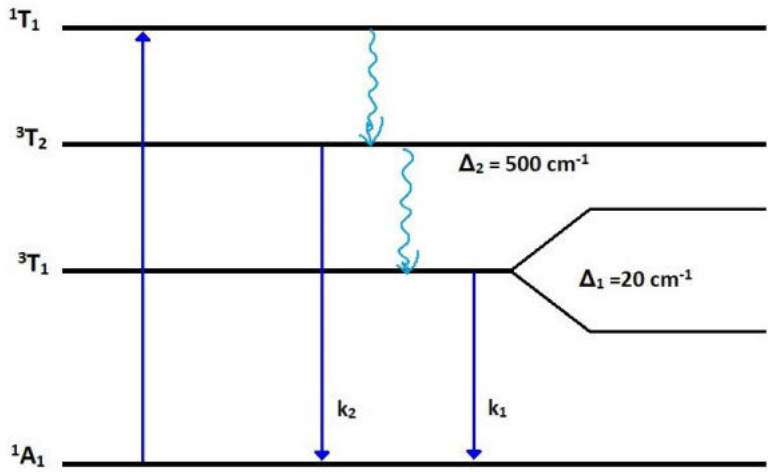

Figure 3.14 Schematic diagram of the splitting of energy levels of WO_4^{2-} in $BaWO_4$

The CIE chromaticity coordinate graph of the $BaWO_4$ samples are plotted, which serves as a standard reference against which many other colour spaces are defined. The chromaticity of a colour is indicated by projection coordinates **x** and **y** or the position of colour in the diagram is called the chromaticity point of the colour [25]. The CIE chromaticity coordinates of the $BaWO_4$ samples under an excitation wavelength of 350 nm are measured as shown in Table 3.5. Figure 3.15 shows the CIE chromaticity diagram for the samples **S1**, **S2** and **S3**. The chromaticity coordinates of the sample **S1** lies within the phosphor triangle and that of **S2** and **S3** lies in the corner of the phosphor triangle. The chromaticity coordinates of all the samples indicate unique blue emission with varying intensity. The sample **S1** gives light blue emission while **S2** and **S3** give dark-blue emission. The results of the PL and CIE chromaticity studies suggest that $BaWO_4$ nanophosphors can be used to construct near-ultraviolet (UV) light excited blue light emitting diodes (LEDs). In short, we can tune the optical absorption and emission properties of the $BaWO_4$ samples by varying the calcination temperature.

Table 3.5 CIE chromaticity coordinates of the $BaWO_4$ samples

Sample	CIE coordinates	
	x	y
S_1	0.1911	0.1813
S_2	0.1605	0.1186
S_3	0.1601	0.1054

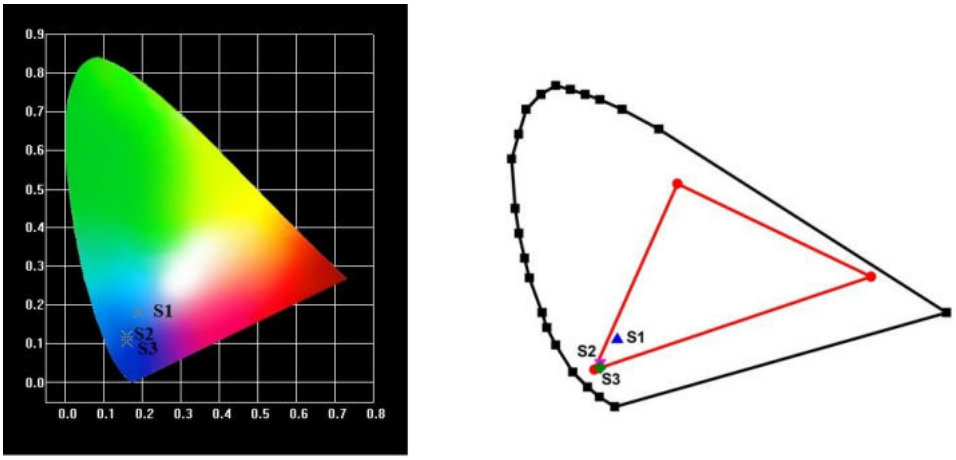

Figure 3.15 CIE chromaticity diagrams of $BaWO_4$ samples

3.3.4 Magnetic Properties

The magnetic properties of the samples are studied using VSM measurements, and the hysteresis curve for the samples is shown in Figure 3.16. It can be seen from Figure 3.16 that all the calcined samples show ferromagnetic behaviour. Also, the saturation magnetization values are low. The results agree with the reported values in the literature [26]. Interestingly, the magnetic parameters such as ferromagnetic behaviour, saturation magnetization, and the coercivity of the samples vary with the calcination temperature. The variation of coercivity, saturation magnetization, retentivity, and squareness ratio (R) of the samples is given in Table 3.6.

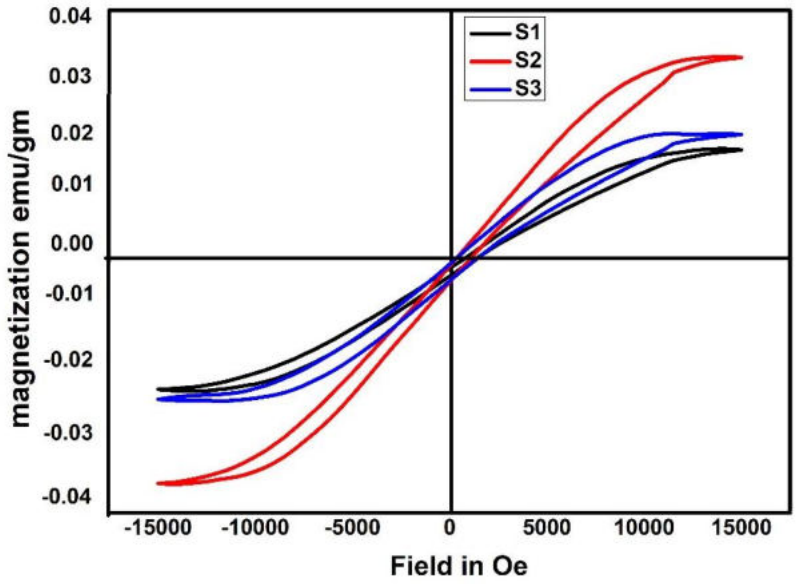

Figure 3.16 M H loop of the $BaWO_4$ samples

Table 3.6 Comparison of magnetic properties of $BaWO_4$ samples

Sample	Saturation magnetization(Ms) emu/gm	Coercivity Oe	Retentivity (Mr) emu/gm	Squareness ratio R=Mr/Ms
S1	25.776×10^{-3}	52.583	0.539×10^{-3}	0.0211
S2	36.183×10^{-3}	66.163	1.455×10^{-3}	0.0402
S3	26.265×10^{-3}	70.404	1.388×10^{-3}	0.0528

The saturation magnetization is maximum for sample **S2** which has the highest value of lattice parameters. Interestingly, the changes in saturation magnetization and retentivity are in accordance with the changes in lattice parameters of the sample with calcination temperature. The saturation magnetization is found to be maximum for the sample with maximum unit cell volume [27]. The coercivity and the squareness ratio R are found to increase with

an increase in calcination temperature. As the calcination temperature increases, the size of the particles increases. So we can conclude that these are single domain particles [28]. As the particle size increases, the coercivity of the single domain particle increases progressively because the magnetic moment of the individual particle increases and the magnetic anisotropy energy increases. Hence, a stronger field is required for reversal.

3.3.5 Dielectric Studies

The dielectric response of the samples is studied in the frequency range of 100 Hz to 1 MHz at selected temperatures.

3.3.5.1 Dielectric Constant

The dielectric constant (ε') of a material is a measure of the storage capacity of electrostatic energy. The electronic, ionic, orientational and interfacial polarization will contribute to the total dielectric constant [29]. Electronic polarization occurs due to the displacement of valence electrons from the nucleus, which appears up to a frequency of 10^{16} Hz. The ionic polarization, due to the separation of positive and negative ions with each other, is effective up to a frequency of 10^{13} Hz. The presence of permanent dipoles in the sample is the source of orientational or dipolar polarization. These dipoles tend to align in the direction of the applied external field, and this polarization is effective up to a frequency of 10^{10} Hz. However, the contribution of dipolar polarization decreases with an increase in frequency since it takes more time to orient in the direction of the field than ionic and electronic polarization [30]. Nanomaterials have about 10^{19} interfaces/cm^2, much abundant than their bulk counterpart. Such interfaces of a large-volume fraction are compact under high pressure of 7.5 Gpa, result in a large number of defects such as microporosities, vacancy clusters, and dangling

bonds. These defects can cause the formation of space charge distribution in the interfaces. As these space charges move towards the electrodes under an external electric field, they are trapped by the defect centres, forming diploes [31] resulting in space charge polarization. The contribution of space charge polarization extends only up to 10^3 Hz.

The dielectric constant ε' of the samples calcined at different temperatures are plotted against frequency in the temperature range of 303 to 423 K is shown in Figure 3.17. For all the three samples, it is found that ε' has a high value at very low frequencies, and it decreases exponentially with an increase in frequency. The dielectric constant remains constant at high frequencies giving rise to a plateau. The high value of the dielectric constant at low frequency is due to the space-charge polarization present at the grain boundaries which result in the generation of a potential barrier, and hence the accumulation of charges at the grain boundary [32]. The dielectric dispersion or rapid decrease of dielectric constant with an increase in frequency is due to the Maxwell-Wagner-type effect (MW) [33]. Another reason for decrease in the dielectric constant is the decrease in the dipolar polarization with an increase in frequency. As the frequency increased, the dipole rotation cannot follow the oscillating field or the oscillation of the dipoles begins to lag behind the oscillating field. On further increase in the frequency of the field, the dipoles cannot follow the field and the orientation will be stopped completely [34]. From Figure 3.17, it is clear that the value of ε' for the sample **S3** is 6.2 at a higher frequency which is slightly greater than that of the samples **S1** and **S2**. It is also discernible with temperature.

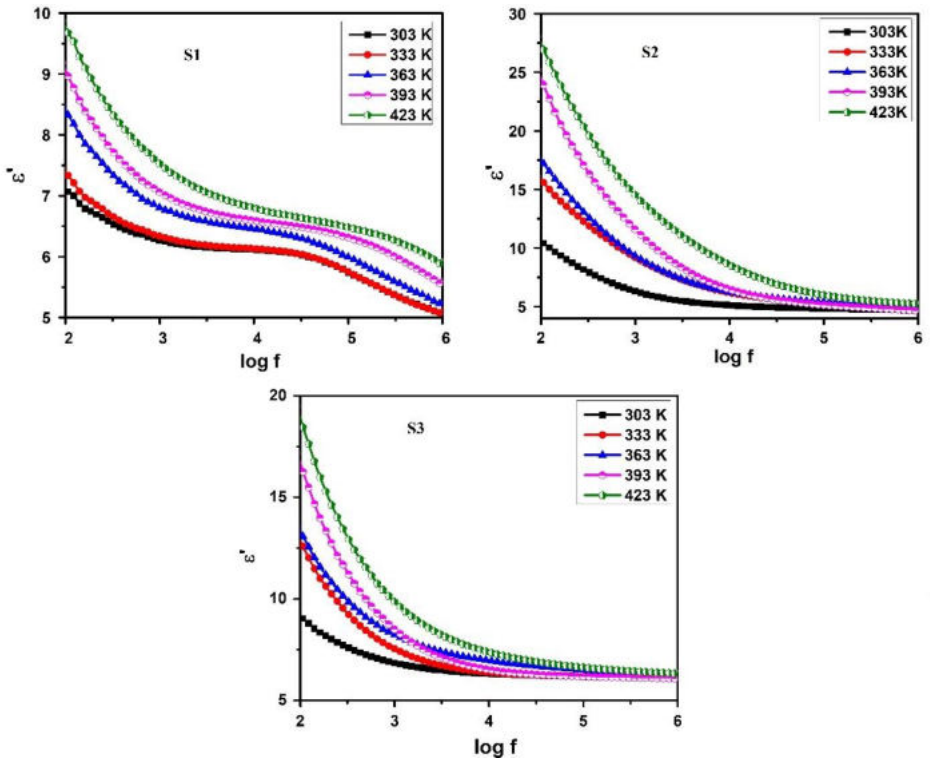

Figure 3.17 The frequency response of the dielectric constant of $BaWO_4$ samples at various temperatures

The variation of ε' with the temperature at different frequencies for the samples **S1**, **S2** and **S3** is shown in Figure 3.18. A linear dependence of ε' with temperature is observed for all the samples. The molecular dipoles remain frozen at low temperature and the free rotation of the dipoles increases with an increase in temperature. Thus more and more dipoles may get aligned at high temperature [35], increasing orientational polarization. It may be the reason for the increase of ε' with temperature. At 1 MHz the value of ε' changes with temperature from 5.15 to 5.89 for the sample **S1**, 4.76 to 5.31 for **S2,** and 6.17 to 6.41 for **S3.** The high and steady value of ε' of $BaWO_4$ samples calcined at 700 °C make it suitable for replacing silicon dioxide (SiO_2) in field-effect transistors (FET).

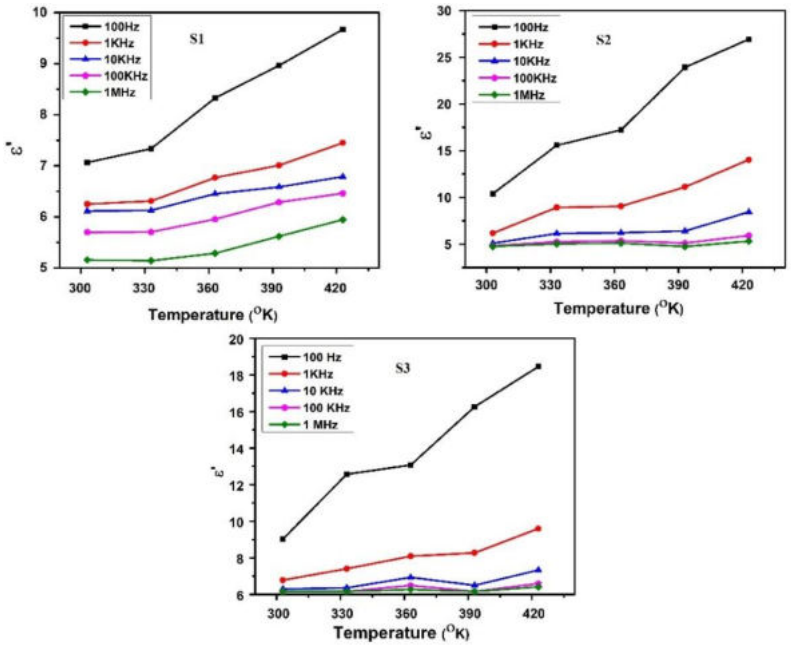

Figure 3.18 The variation of dielectric constant of $BaWO_4$ with temperature

3.3.5.2 Frequency and Temperature Dependence of Dielectric Loss

Dielectric loss ε" is a measure of energy losses to move ions when the polarity of the electric field turns rapidly, which is a material property and does not depend on the geometry of the capacitor [36]. The alteration of ε" against frequency at various temperatures for the $BaWO_4$ samples is shown in Figure 3.19. It is found that ε" decreases with an increase in frequency and increases with an increase in temperature. At low frequencies, the high value of the dielectric loss is due to the free charge motion [37] or the migration of ions within the material. At medium frequencies, ion jump, conduction loss of ion migration, and ions polarization loss will contribute to the dielectric loss. But at higher frequencies, the dielectric loss is purely due to the ion vibrations, and hence ε" is steady at high frequencies [38]. The frequency dependence of ε" is given by the relation,

$$\varepsilon'' = A_1 \omega^m \qquad (3.3)$$

where A_1 is a constant and m is the slope of the curve obtained. The low and steady value of ε' and ε'' at high frequencies put forward that the prepared $BaWO_4$ sample possesses enhanced optical quality with lesser defect, hence suitable for nonlinear optical materials applications [39].

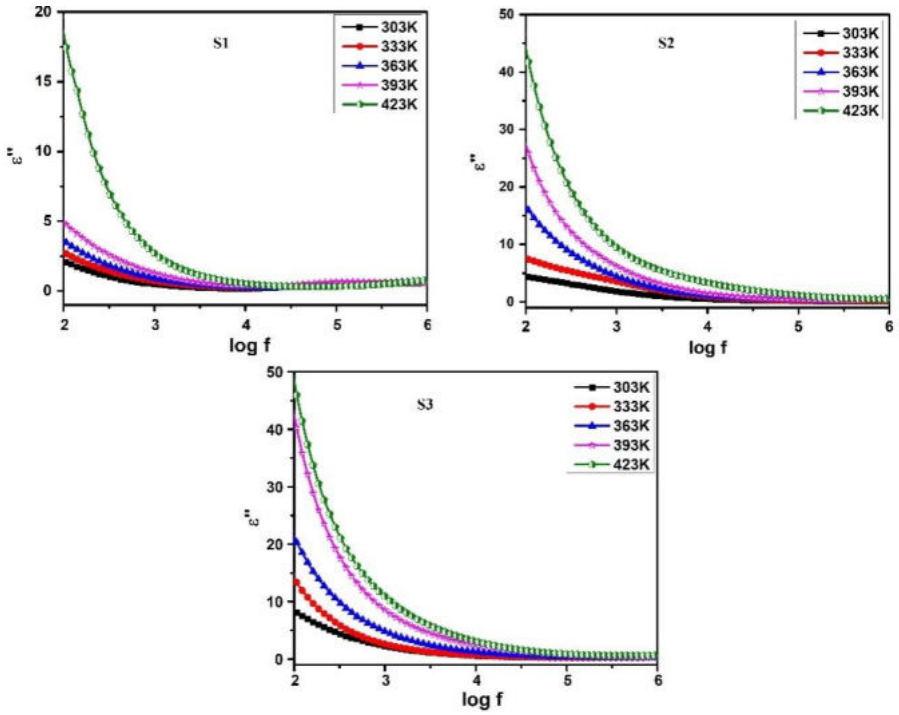

Figure 3.19 Variation of ε'' against frequency of the $BaWO_4$ samples at different temperatures

3.3.5.3 Dissipation Factor

The dissipation factor or loss tangent tanδ of the samples at different temperatures are plotted against frequency is shown in Figure 3.20. The dissipation factor of a dielectric is the rate of loss of electromagnetic energy, or it

is a measure of how well a material can absorb electromagnetic energy. As shown in Figure 3.20, the value of tanδ for the $BaWO_4$ samples decreases rapidly at low frequencies and attain steady values at high frequencies. At high frequencies, the charge carriers existing in the material can migrate through some distances under the influence of the external field, reducing the absorption current. But at low frequencies, such charge carriers are blocked at the electrodes, resulting in a space charge region, which leads to a substantial increase in the value of tanδ [40]. At low frequencies, more energy is required for electron hopping due to space charge polarization as a result of high energy loss. While at higher frequencies, the energy required for electron hopping is low, hence the low value of tanδ.

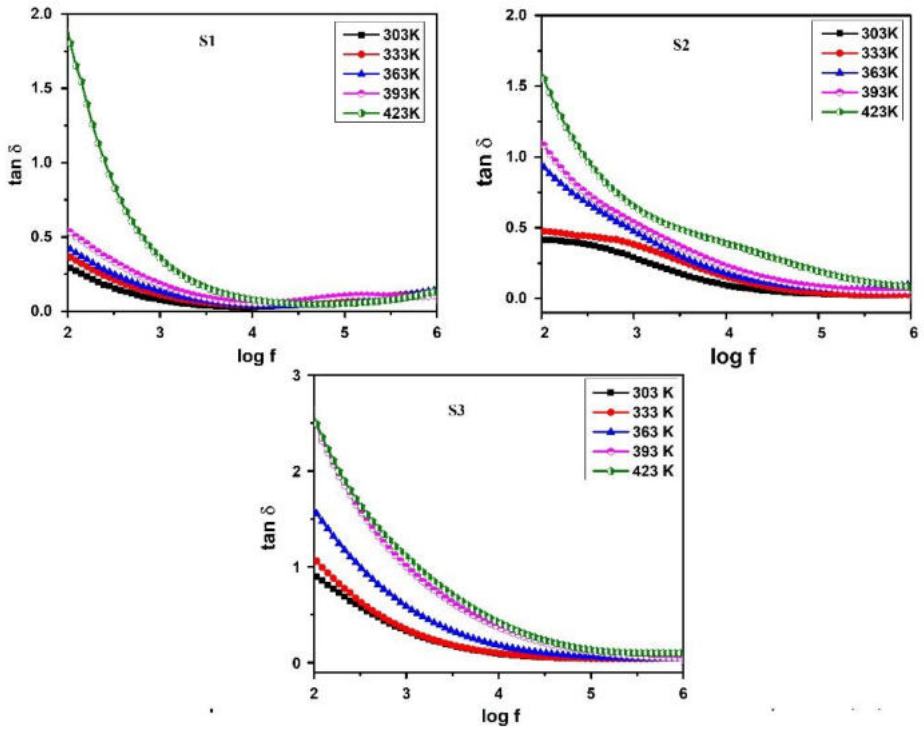

Figure 3.20 Frequency response of the dissipation factor tanδ for the $BaWO_4$ samples

It can be seen from Figure 3.20 that the value of the dissipation factor increases with an increase in the temperature of the samples. However, there is only a slight variation in the dissipation factor in the mega frequency range. The variation of tanδ with frequency is found to be almost in a similar manner for all temperatures. The low and steady value of dissipation factor and an almost steady value of the dielectric constant of $BaWO_4$ samples over a wide range of frequencies suggest their suitability in low-temperature co-fired ceramic (LTCC) applications [41].

3.3.5.4 AC Conductivity

The frequency variation studies are carried out to understand the electrical homogeneity of the material by recognizing the relaxation mechanism as well as the nature of electrical conduction. The AC conductivity of the samples plotted against frequency for various temperatures is shown in Figure 3.21. At low frequencies, AC conductivity is very low. At high frequencies, a sharp increase in AC conductivity is observed with frequency. A slight increase in ac conductivity is also observed with temperature.

The variation of AC conductivity with frequency can be explained by Jonscher's power law [42]

$$\sigma_{ac}(\omega) = \sigma_0 + A\omega^s \qquad (3.4)$$

where σ_0 is the frequency-independent conductivity (which is related to DC conductivity), A is the temperature-dependent pre-exponential factor and ***s*** is the frequency exponent ($0 \leq s \leq 1$), which characterizes the low-frequency region corresponding to translational ion hopping.

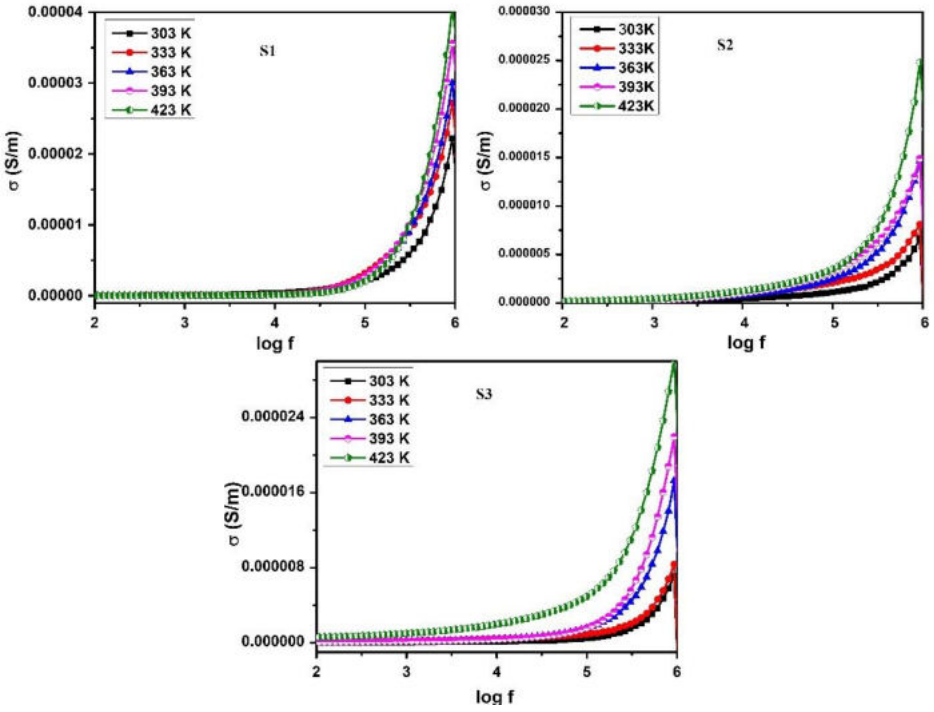

Figure 3.21 Variation of AC conductivity of the $BaWO_4$ samples against frequency

The conduction mechanism is based on the creation of energetic free electrons, ions, and free radicals, and on electronic hoping [43]. At low frequencies, AC conductivity is very low and almost steady, which stands for (σ_0), and as the frequency increases, the conductivity also increases obeying Jonscher's power law. The accumulation of charge carriers at the electrode interface reduces the electrical conductivity at low frequencies [44]. There is random diffusion of charge carriers at high frequencies by virtue of which the conductivity increases. The cross-over from the frequency-independent region to the frequency-dependent region indicates the transition from long-range hoping to short-range ionic motion [42]. At high frequencies, there is a linear increase in the AC conductivity suggesting the long rage drift of ions [37] or polaron hopping as the

source of ion conduction [45]. There is an easy transition of charge carriers from the valence band to the conduction band with the rise in temperature, resulting in an increased conductivity [46]. The value of ***s*** is estimated from the slope of the logσ versus logω line. The obtained values of ***s*** are less than unity (ranges between 0.35 and 0.45) which complies with the correlated barrier hopping model.

3.4 Conclusion

- Nanocrystalline $BaWO_4$ powder samples are successfully prepared by direct chemical precipitation method without using any surfactant, templates, or catalyst.
- $BaWO_4$ powder samples are found to be thermally stable above 340 ºC.
- Structural characterization confirms the crystalline nature and scheelite tetrahedral structure of the synthesized $BaWO_4$ with a space group $I4_1/a$.
- Effect of calcination on the structural, optical, magnetic, and electrical properties of the synthesized sample is studied.
- The average crystallite sizes of the samples are found to increase with the increase in calcination temperature, by thermally promoted crystalline growth.
- The surface morphology of $BaWO_4$ samples changes with the calcination temperature.
- From TEM images, it is confirmed that the particles are approximately spherical.

- UV-Visible absorption spectra show an absorption peak in the ultraviolet region. The optical bandgap values of the $BaWO_4$ samples are found to decrease with the increase in calcination temperature.

- A broad PL emission is observed in the blue region corresponding to the transition from the degenerate $^3T_1$ excited state to the $^1A_1$ ground state of the $(WO_4)^{2-}$ tetrahedral group. The PL spectra and CIE chromaticity diagram confirm blue emission for $BaWO_4$ nanocrystalline phosphors.

- The nanocrystalline $BaWO_4$ samples possess ferromagnetic behaviour at room temperature and found that there is an anomalous variation of magnetic properties with calcination temperature.

- The dielectric studies show that the dielectric constant, loss tangent, and AC conductivity of the $BaWO_4$ sample change with the increase in calcination temperature. These properties are also frequency and temperature dependent.

- The low and steady value of the dissipation factor and an almost steady value of the dielectric constant suggest the suitability of $BaWO_4$ in LTCC applications.

References

[1] S.K. Stephen, N. Aloysius Sabu, K.P. Priyanka, T. Varghese, Effect of calcination on the structural, optical and magnetic properties of $BaWO_4$ nanoparticles synthesized by chemical precipitation, Indian J. Pure Appl. Phys. 57 (2019) 14–22.

[2] K.P. Priyanka, K.K. Babitha, A. Sreedevi, X. Sheena, E.M. Mohammed, T. Varghese, Chemical synthesis, structural characterization and electrical studies of nanoceria for CMOS applications, J. Electroceramics. 32 (2014) 361–368.

[3] B.D. Cullity, Elements of X ray Diffraction, Addison-Wesley Publishing Company inc, 1978.

[4] C.R. Indulal, G.S. Kumar, A. V. Vaidyan, R. Raveendran, Characterization , dielectric and optical studies of cerium molybdo tungstate nanoparticles, 48 (2010) 893–898.

[5] G.K. Williamson, W.H. Hall, X-Ray broadening from filed aluminium and tungsten, Acta Metall. 1 (1953) 22–31.

[6] C. Suryanarayana, M.G. Norton, X-ray diffraction : A Practical Approach, Plenum Press, 1998.

[7] A. Phuruangrat, T. Thongtem, S. Thongtem, Barium molybdate and barium tungstate nanocrystals synthesized by a cyclic microwave irradiation, J. Phys. Chem. Solids. 70 (2009) 955–959.

[8] H. Shi, X. Wang, N. Zhao, L. Qi, J. Ma, Growth mechanism of penniform $BaWO_4$ nanostructures in catanionic reverse micelles involving polymers, J. Phys. Chem. B. 110 (2006) 748–753.

[9] D.L. Rousseau, R.P. Bauman, S.P.S. Porto, Normal mode determination in crystals.pdf, J. Raman Spectrosc. 10 (1981) 0377–0486.

[10] T. Thongtem, A. Phuruangrat, S. Thongtem, Characterization of $MeWO_4$ (Me = Ba, Sr and Ca) nanocrystallines prepared by sonochemical method,

Appl. Surf. Sci. 254 (2008) 7581–7585.

[11] A. Phuruangrat, T. Thongtem, S. Thongtem, Cyclic microwave-assisted synthesis and characterization of nano-crystalline alkaline earth metal tungstates, J. Ceram. Soc. Japan. 116 (2008) 605–609.

[12] F.J. Manjón, D. Errandonea, N. Garro, J. Pellicer-Porres, P. Rodríguez-Hernández, S. Radescu, J. López-Solano, A. Mujica, A. Muñoz, Lattice dynamics study of scheelite tungstates under high pressure I. $BaWO_4$, Phys. Rev. B - Condens. Matter Mater. Phys. 74 (2006) 1–17.

[13] T.T. Basiev, A.A. Sobol, Y.K. Voronko, P.G. Zverev, Spontaneous Raman spectroscopy of tungstate and molybdate crystals for Raman lasers, Opt. Mater. (Amst). 15 (2000) 205–216.

[14] S.M.M. Zawawi, R. Yahya, A. Hassan, H.N.M.E. Mahmud, M.N. Daud, Structural and optical characterization of metal tungstates (MWO_4; M=Ni, Ba, Bi) synthesized by a sucrose-templated method, Chem. Cent. J. 7 (2013) 1.

[15] L.S. Cavalcante, J.C. Sczancoski, L.F. Lima, J.W.M. Espinosa, P.S. Pizani, J.A. Varela, E. Longo, Synthesis, characterization, anisotropic growth and photoluminescence of $BaWO_4$, Cryst. Growth Des. 9 (2009) 1002–1012.

[16] S. Desgreniers, S. Jandl, C. Carlone, Temperature dependence of the Raman active phonons in $CaWO_4$, $SrWO_4$ and $BaWO_4$, J. Phys. Chem. Solids. 45 (1984) 1105–1109.

[17] S.M.M. Zawawi, R. Yahya, A. Hassan, M.N. Daud, Preparation and characterisation of tungstate scheelite structured nanoparticles, Mater. Res.

Innov. 15 (2011) 97–100.

[18] W.M. Yen', S. Shionoya, H. Yamamoto, eds., Fundamentals of Phosphors, CRC Press, Taylor and Francis Group, 2007.

[19] S. Vidya, S. Solomon, J.K. Thomas, Synthesis, characterization, and low temperature sintering of nanostructured $BaWO_4$ for optical and LTCC applications, Adv. Condens. Matter Phys. 2013 (2013) 1-8.

[20] G.K. Sahu, S. Behera, Investigation of optical and structural properties of scheelite-type barium tungstate ceramic, Int. J. Manag. Technol. Eng. 8 (2018) 2314–2320.

[21] A. Phuruangrat, T. Thongtem, S. Thongtem, Synthesis, characterisation and photoluminescence of nanocrystalline calcium tungstate, J. Exp. Nanosci. 5 (2010) 263–270.

[22] G. Benoît, J. Véronique, A. Arnaud, G. Alain, Luminescence properties of tungstates and molybdates phosphors: Illustration on $ALn(MO_4)_2$ compounds (A = alikaline cation, Ln = lanthanides, M = W, Mo), Solid State Sci. 13 (2011) 460–467.

[23] S. Shionoya, W. M. Yen, H. Yamamoto, Phosphor Handbook, CRC Press, Taylor and Francis Group, 2007.

[24] W.N. Wang, W. Widiyastuti, T. Ogi, I.W. Lenggoro, K. Okuyama, Correlations between crystallite/particle size and photoluminescence properties of submicrometer phosphors, Chem. Mater. 19 (2007) 1723–1730.

[25] N. Kohei, S. Suekokanaya, Color Vision, in: S. Shionoya, W. M. Yen, H. Yamamoto (Eds.), Phosphor Handb., CRC Press, Taylor and Francis Group, 2007.

[26] S. Khademolhoseini, S. Ali Zarkar, Preparation and characterization of barium tungstate nanoparticles via a new simple surfactant-free route, J. Mater. Sci. Mater. Electron. 27 (2016) 9605–9609.

[27] J. Anghel, A. Thurber, D.A. Tenne, C.B. Hanna, A. Punnoose, Correlation between saturation magnetization, bandgap, and lattice volume of transition metal (M=Cr, Mn, Fe, Co, or Ni) doped $Zn_{1-x}M_xO$ nanoparticles, J. Appl. Phys. 107 (2010) 09E314..

[28] G. Rowlands, The variation of coercivity with particle size, J. Phys. D. Appl. Phys. 9 (1976) 1267–1269.

[29] H. Dhaouadi, O. Ghodbane, F. Hosni, F. Touati, Mn_3O_4 Nanoparticles: Synthesis, characterization, and dielectric properties, ISRN Spectrosc. 2012 (2012) 1–8.

[30] N. Shukla, H.P. Pathak, V. Rao, D.K. Dwivedi, A . C . conductivity and dielectric properties of $Se_{90}Cd_6Sb_4$ glassy alloy, Chalcogenide Lett. 13 (2016) 177–185.

[31] A.S. Lanje, S.J. Sharma, R.B. Pode, R.S. Ningthoujam, Dielectric study of Tin oxide nanoparticles at low temperature, Sch. Res. Libr. 2 (2011) 373–383.

[32] C. Rayssi, S. El Kossi, J. Dhahri, K. Khirouni, Frequency and temperature-dependence of dielectric permittivity and electric modulus studies of the

solid solution $Ca_{0.85}Er_{0.1}Ti_{1-x}Co_{4x/3}O_3$ ($0 \leq x \leq 0.1$), RSC Adv. 8 (2018) 17139–17150.

[33] Z. Kukula et al, Dielectric and magnetic permittivities of three new ceramic tungstates $MPr_2W_2O_{10}$ (M = Cd, Co, Mn), Philos. Mag. 92 (2012) 4167–4181.

[34] N. Aloysius, M.S. Rintu, E.M. Muhammed, T. Varghese, Dielectric studies of nanocrystalline calcium tungstate, Nanosyst. Physics, Chem. Math. (2016) 599–603.

[35] V.S. Yadav, D.K. Sahu, Y. Singh, M. Kumar, D.C. Dhubkarya, Frequency and temperature dependence of dielectric properties of Pure Poly Vinylidene Fluoride (PVDF) thin films, AIP Conf. Proc. 1285 (2010) 267–278.

[36] N.H. Ahmad, M.I.N. Isa, Ionic conductivity and electrical properties of carboxymethyl cellulose - NH_4Cl solid polymer electrolytes, J. Eng. Sci. Technol. 11 (2016) 839–847.

[37] D.K. Pradhan, R.N.P. Choudhary, B.K. Samantaray, Studies of dielectric relaxation and AC conductivity behavior of plasticized polymer nanocomposite electrolytes, Int. J. Electrochem. Sci. 3 (2008) 597–608.

[38] N.A. Hegab, A.E. Bekheet, M.A. Afifi, L.A. Wahab, H.A. Shehata, Effect of Cd addition on the AC conductivity and dielectric properties of $Ge_{70}Te_{30}$ films, J. Ovonic Res. 3 (2007) 71–82.

[39] N. Shukla, V. Rao, D.K. Dwivedi, Dielectric relaxation studies in $Se_{90}Cd_8Sb_2$ glassy alloy, AIP Conf. Proc. 1728 (2016).

[40] N. Shukla, D.K. Dwivedi, Dielectric relaxation and AC conductivity studies of $Se_{90}Cd_{10-x}In_x$ glassy alloys, J. Asian Ceram. Soc. 4 (2016) 178–184.

[41] M.T. Sebastian, R. Ubic, H. Jantunen, Low-loss dielectric ceramic materials and their properties, Int. Mater. Rev. 60 (2015) 392–412.

[42] B.K. Barick, K.K. Mishra, A.K. Arora, R.N.P. Choudhary, D.K. Pradhan, Impedance and Raman spectroscopic studies of $(Na_{0.5}Bi_{0.5})TiO_3$, J. Phys. D. Appl. Phys. 44 (2011)1-10.

[43] S. Fares, Frequency dependence of the electrical conductivity and dielectric constants of polycarbonate (Makrofol-E) film under the effects of γ-radiation, Nat. Sci. 03 (2011) 1034–1039.

[44] S.K. Satpathy, N.K. Mohanty, A.K. Behera, B. Behera, Dielectric and electrical properties of $0.5(BiGd_{0.05}Fe_{0.95}O_3)$-$0.5(PbZrO_3)$ composite, Mater. Sci. Pol. 32 (2014) 59–65.

[45] S. Sharma, R. Singh, A. Geetika, Ac conductivity and dielectric properties of manganese doped layered $Na_{1.89}Li_{0.10}K_{0.01}Ti_3O_7$ ceramics, Int. J. Mod. Phys. B. 28 (2014) 1–19.

[46] K.K. Babitha, K.P. Priyanka, A. Sreedevi, B. Abraham, J.K. Thomas, T. Varghese, Studies on the structural, optical and electrical properties of CeO_2/SnPc nanocomposite for electronic applications, J. Mater. Sci. Mater. Electron. 28 (2017) 1115–1123.

Chapter 4

EFFECT OF COPPER DOPING ON THE PROPERTIES OF NANOCRYSTALLINE $BaWO_4$

This chapter focuses on the modification in the structural, optical and magnetic properties of nanocrystalline $BaWO_4$ by copper doping. 1, 3 and 5 mol % of copper doped $BaWO_4$ samples are synthesized by chemical precipitation method and characterized using various characterization techniques.

4.1 Introduction

In material science, there is an increasing interest in finding new materials with attractive photoluminescence properties for the development of optoelectronic devices or a material with high photocatalytic activities for the degradation of organic dyes produced by the industries. Doping is the primary technique used for the modification of properties of nanostructured materials to obtain new materials of technological importance. $BaWO_4$ is an excellent host material for designing solid-state lasers emitting radiations in a specific region because of its stimulated Raman scattering (SRS) properties and has applications

in fields such as medical treatment, spectroscopy, and up-conversion lasers [1,2]. Among various metallic doping elements, Cu doping is a way to improve visible-light absorption [3]. No studies have been reported on the effect of Cu doping in $BaWO_4$ lattice. A systematic and detailed investigation on the structural, optical and magnetic properties of Cu doped nanocrystalline $BaWO_4$ is presented here. Interestingly, Cu doping resulted in dramatic changes in the structural, morphological, optical, and magnetic properties of $BaWO_4$.

4.2 Synthesis of Copper Doped $BaWO_4$

Analytical grade chemicals, barium nitrate ($Ba(NO_3)_2$) (99%, Merk), copper(II) nitrate ($Cu(NO_3)_2.3H_2O$) (98%, Merk), and sodium tungstate ($Na_2WO_4.2H_2O$) (98%, Merk) were used as received without further purification for the synthesis of Cu doped $BaWO_4$ samples. 1, 3, and 5 mol % Cu doped nanocrystalline $BaWO_4$ samples were prepared by the chemical precipitation method. Initially, 0.1 M solutions of barium nitrate and copper nitrate were mixed in the desired ratios (1, 3, and 5% copper nitrate). Then, 0.1 M solution of sodium tungstate was slowly added to the mixture by continuously stirring at room temperature for half an hour using a magnetic stirrer apparatus. Distilled water was used as the medium of preparation. The obtained precipitate was washed with abundant distilled water until the pH of the medium containing the precipitate becomes 7 and dried for 24 h in a hot air oven at 80 $^{\circ}$C. The dried powder was pulverized well and calcined at 400 $^{\circ}$C for 3 h in a muffle furnace [4]. $BaWO_4$ samples doped with 1, 3, and 5 mol % of Cu are denoted as **Cu1**, **Cu3** and **Cu5** respectively. **S1** represents the pristine $BaWO_4$ sample. Synthesis of the pristine sample **S1** is described in Chapter 3.

4.3 Results and Discussion

The structural, optical and magnetic characterizations of the pristine and Cu doped $BaWO_4$ samples are done using various techniques as described in *Chapter 2*.

4.3.1 Structural Characterization

The structural characterizations of the synthesized samples are done using powder X-ray diffraction, Fourier transform infrared spectroscopy, Raman spectroscopy, scanning electron microscopy, transmission electron microscopy, and energy dispersive X-ray analysis by following the procedure described in *Section 2.4.*

4.3.1.1 Powder XRD Analysis

The synthesized products are structurally characterized by X-ray diffraction using Brucker AXS D8 Advance X-ray diffractometer (λ = 1.5406 Å, step size = 0.01º) with CuKα radiation in 2θ range from 10 to 80º, operating voltage 40 kV and current 35 mA. The powder XRD patterns of pristine and Cu doped $BaWO_4$ samples are shown in Figure 4.1. All the diffraction peaks indicate that these samples crystallize in a scheelite type tetragonal structure with space group $I4_1/a$. The well-defined sharp diffraction peaks indicate the purity and crystallinity of the samples, and it agrees well with the JCPDS Card no. 72-0746 of $BaWO_4$. No glimpse of any extra-phase is observed in the doped samples, which may be due to the lower loading of the dopants. Lattice parameters of the pristine and Cu doped $BaWO_4$ samples are calculated using the plane spacing equation for tetragonal structure [5], and the crystallite size of the particles is estimated using the Scherrer equation as described in *Section 2.4.1.*

The crystallite size and lattice strain of the pristine and Cu doped $BaWO_4$ samples are estimated using the Williamson–Hall (W-H) method [6] as described in *Section 2.4.1.* W-H plots for the pristine and Cu doped $BaWO_4$ samples are shown in Figure 4.2. The obtained lattice parameters, unit cell volume, micro-strain, and crystallite size of the pristine and Cu doped $BaWO_4$ samples are itemized in Table 4.1. The (hkl) values of the protruding peaks are marked on the XRD patterns. Rietveld refinements of the samples are done using TOPAS. The double-Voigt method is used for peak profile fitting. All refinement results indicated that the pristine and Cu doped $BaWO_4$ samples displayed a pure scheelite-type tetragonal phase with space group $I4_1/a$. The structure parameters obtained from the Rietveld refinement of the XRD data are presented in Table 4.2, and the refinement outputs are shown in Figure 4.3.

After incorporating Cu ions into the $BaWO_4$ lattice, no significant change in the XRD pattern is observed. It indicates that there is no change in the tetragonal structure of the lattice due to the incorporation of Cu ions. However, slight changes are found in the intensity of XRD peaks, lattice constants, unit cell volume, and structural parameters of the doped samples. The intensity of the XRD peaks is maximum for the sample **Cu3**, indicating the improved crystallinity of the sample [7]. In Table 4.1 and 4.2, the lattice constant **a** and the unit cell volume of the $BaWO_4$ samples decrease with an increase in the concentration of Cu, which is attributed to the doping of smaller Cu^{2+} ions (ionic radius = 0.73 Å) at larger Ba^{2+} (ionic radius = 1.42 Å) sites in the tetragonal structure of $BaWO_4$ [8]. The decrease in unit cell volume with an increase in Cu^{2+} dopant concentrations is due to an increase in CuO_8 clusters, which have smaller volume compared to BaO_8 clusters. The lattice constant **c** of the Cu doped $BaWO_4$ samples changes in an irregular manner. The small variations in these parameters can be associated with the lattice distortions.

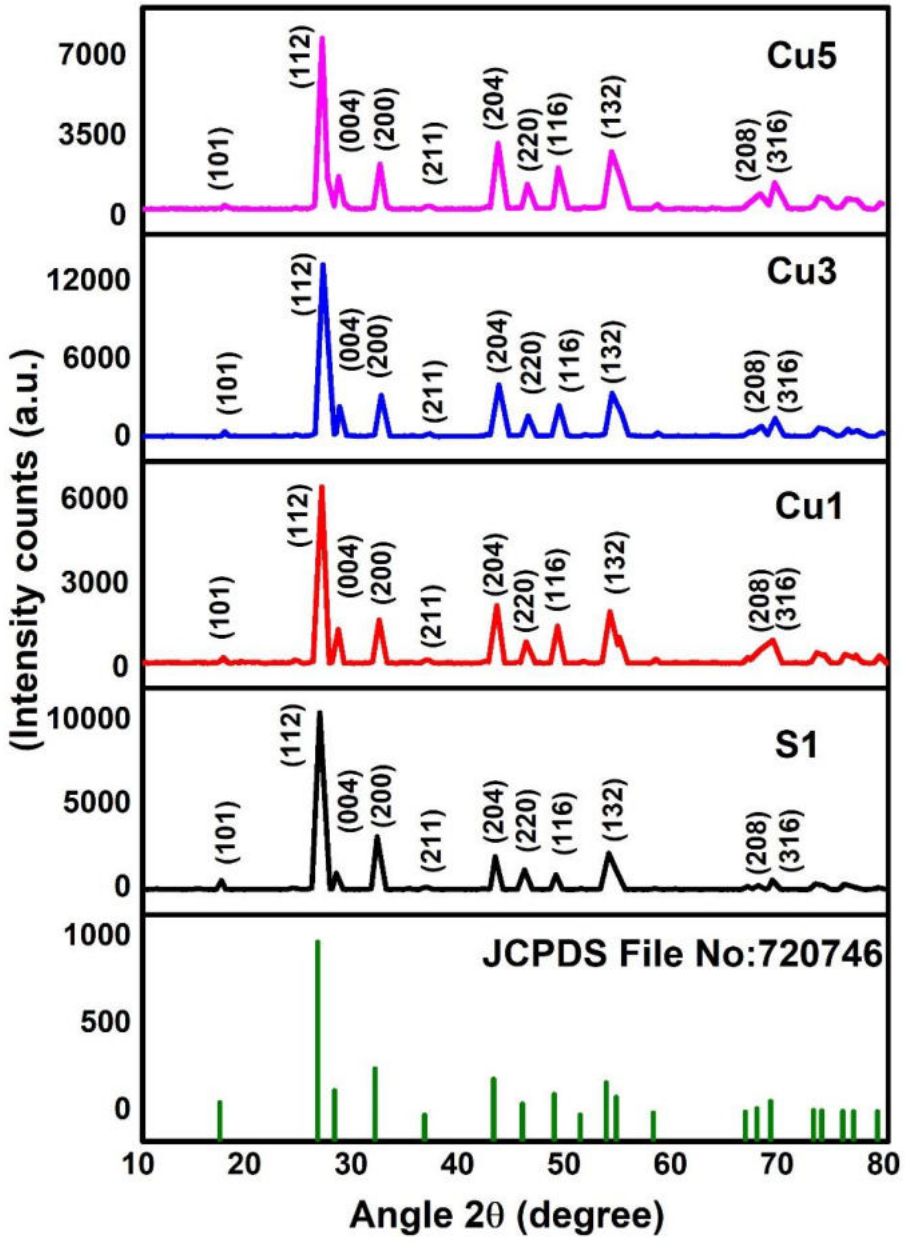

Figure 4.1 The XRD patterns of pristine and Cu doped $BaWO_4$ samples

Table 4.1 Geometric parameters of pristine and Cu doped $BaWO_4$ samples

Sample	a = b (Å)	c (Å)	Unit cell volume ($Å^3$)	Crystallite size in nm		Micro-strain $\times10^{-3}$
				Scherrer method	W-H method	
S1	5.589	12.658	395.450	13.15	14.56	0.149
Cu1	5.573	12.615	391.800	11.77	12.48	0.207
Cu3	5.551	12.576	387.512	11.01	12. 27	0.187
Cu5	5.536	12.598	386.095	11.31	12.31	0.202

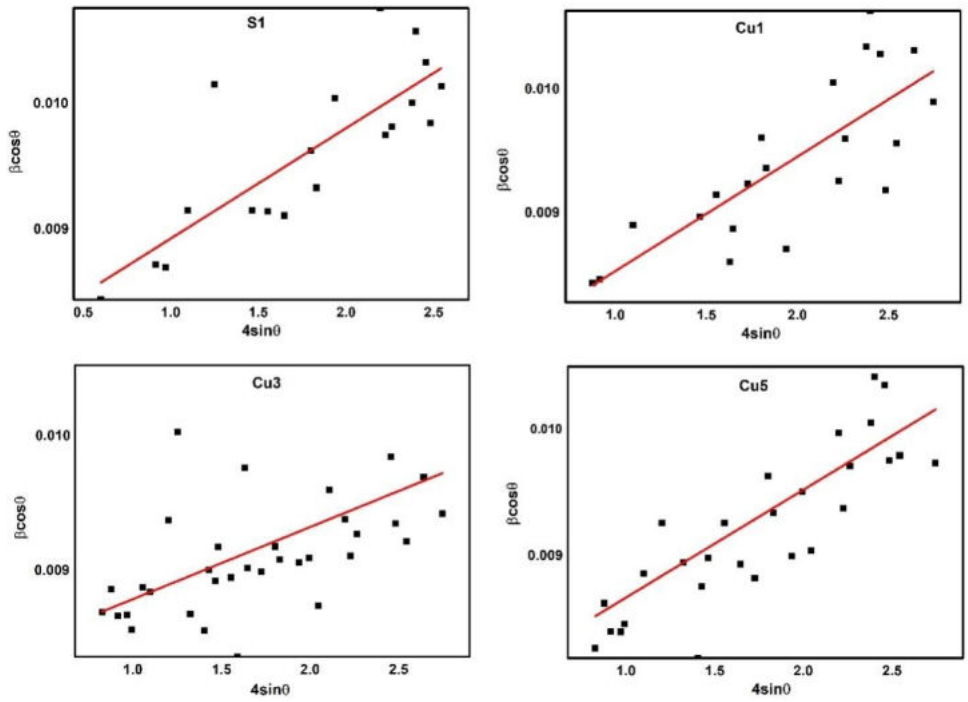

Figure 4.2 W-H plots of pristine and Cu doped $BaWO_4$ samples

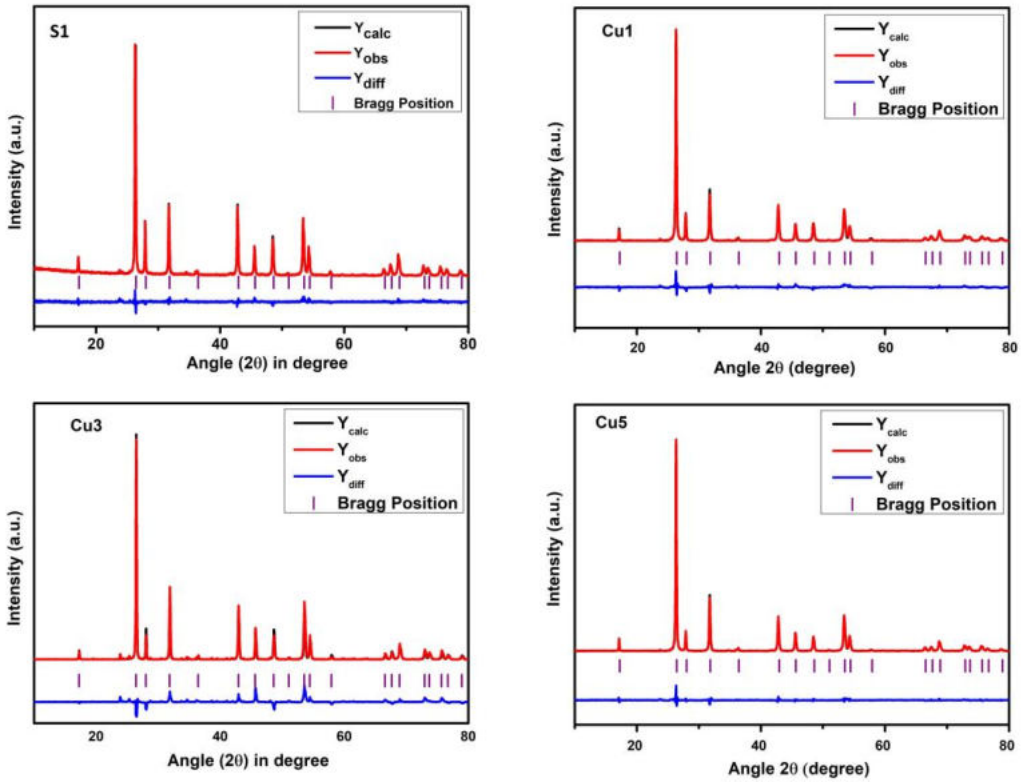

Figure 4.3 Observed, calculated and difference pattern of pristine and Cu doped $BaWO_4$ samples

Table 4.2 Structural parameters of pristine and Cu doped $BaWO_4$ samples

sample	Atom	Site	x	y	z	a=b (Å)	c (Å)	Unit cell volume (Å^3)	R_{wp}	R_p	R_e	GOF
S1	Ba	4b	0.0000	0.2500	0.6250	5.621	12.741	402.62	9.71	7.38	6.66	1.45
	W	4a	0.0000	0.2500	0.1250							
	O	16f	0.1259	0.0056	0.2097							
Cu1	Ba	4b	0.0000	0.2500	0.6250	5.612	12.727	400.80	7.86	5.92	6.98	1.13
	W	4a	0.0000	0.2500	0.1250							
	O	16f	0.1439	0.0248	0.2226							
Cu3	Ba	4b	0.0000	0.2500	0.6250	5.591	12.737	398.20	8.52	6.51	6.31	1.35
	W	4a	0.0000	0.2500	0.1250							
	O	16f	0.1639	0.0360	0.2188							
Cu5	Ba	4b	0.0000	0.2500	0.6250	5.589	12.688	396.33	9.21	6.89	6.65	1.38
	W	4a	0.0000	0.2500	0.1250							
	O	16f	0.2145	0.0086	0.2126							

4.3.1.2 SEM and EDX Analysis

The microstructural characterization of the pristine and doped $BaWO_4$ samples is performed using a scanning electron microscope JOEL model JEK-6390 LV, resolution 3 nm (Acc. V 20 kV, WD 14 mm, SEI), 8 nm (Acc V 3 kV, WD 6 mm), 15 nm (Acc V 1.0 kV, WD 6 mm). Figure 4.4 depicts the SEM images of the pristine and Cu doped $BaWO_4$ samples. The SEM photograph represents the topography and surface morphology of the highly agglomerated particles with many voids. The morphology of the samples changes to a flower-like structure with the incorporation of Cu atoms into it. As shown in the Figure 4.4, sample **S1** is found to be highly porous. The microstructures are not in uniform size and shape. As the quantity of Cu in the sample increases the porosity decreases, and the surface becomes smooth. The changes in the topography of the samples may have a significant effect on the electrical and optical properties of the material.

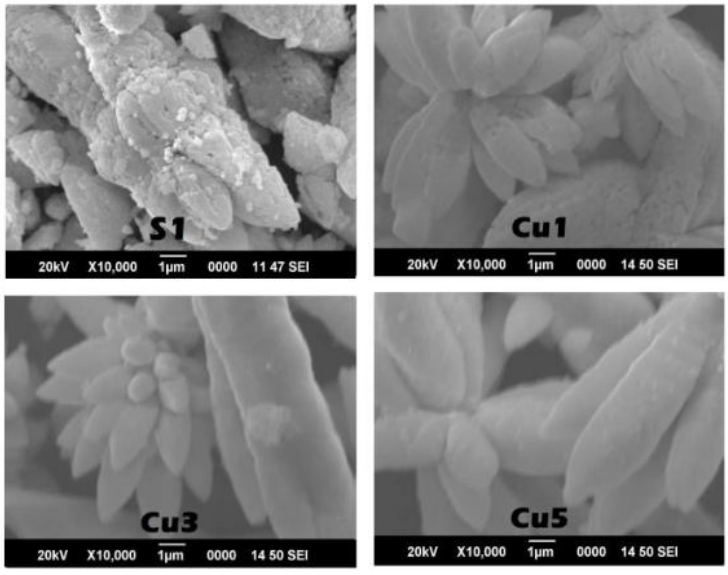

Figure 4.4 SEM images of pristine and Cu doped $BaWO_4$ samples

The EDX spectra (Figure 4.5) of the pristine and Cu doped $BaWO_4$ samples are taken for elemental analysis or chemical characterization. The existence of elements Ba, W, O, and Cu in the samples is confirmed by energy dispersive X-ray analysis. The elemental composition of the pristine and Cu doped $BaWO_4$ samples are presented in Table 4.3. The presence of Cu in the EDX spectra confirms the successful formation of Cu doped $BaWO_4$. No impurities are observed in the EDX spectra (Figure 4.5 and Table 4.3) that reveal the purity of the prepared samples.

Table 4.3 Elemental composition of pristine and Cu doped $BaWO_4$ samples

sample	Element	Line Type	Mass %	Atomic %
S1	O	K series	18.92	70.43
	Ba	L series	30.05	13.03
	W	L series	51.03	16.53
	Cu	-	0	0
Cu1	O	K series	16.15	64.84
	Ba	L series	39.59	18.52
	W	M series	43.57	15.84
	Cu	K series	0.69	0.81
Cu3	O	K series	16.01	63.3
	Ba	L series	44.09	20.59
	W	M series	38.06	14.3
	Cu	K series	1.85	1.8
Cu5	O	K series	16.66	65.5
	Ba	L series	35.02	16.03
	W	M series	45.31	15.5
	Cu	K series	3.01	2.97

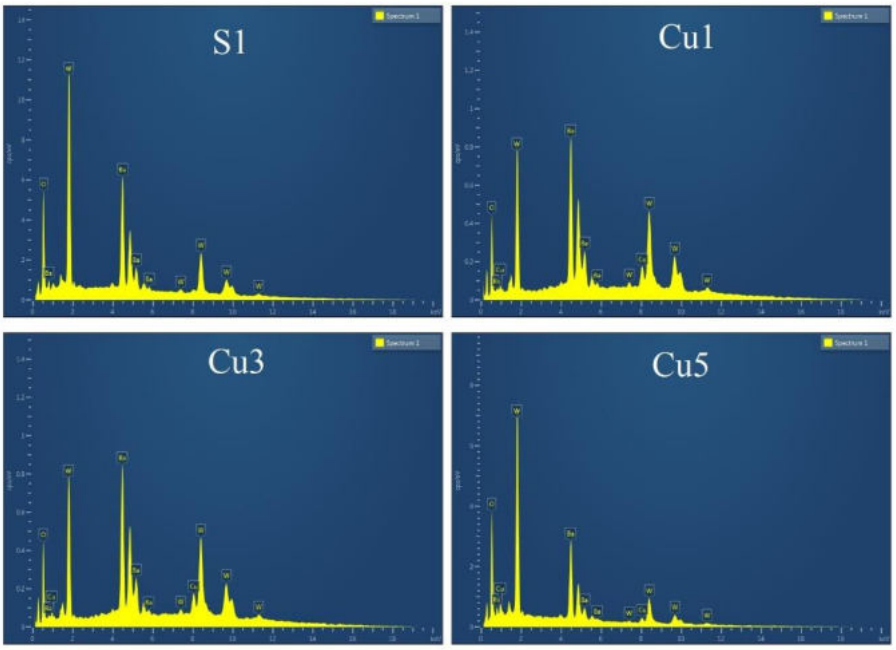

Figure 4.5 EDX spectra of pristine and Cu doped $BaWO_4$ samples

4.3.1.3 TEM Analysis

TEM images, HRTEM images, and SAED patterns are recorded using JEOL JEM 2100 at an accelerating voltage of 200 kV. Figure 4.6 shows the TEM bright field images, HRTEM images and SAED patterns of the pristine and Cu doped $BaWO_4$ samples. TEM images reveal that the morphology and particle sizes of the Cu doped $BaWO_4$ samples changes with the amount of Cu content in the sample. The particles of the sample **S1** is fully agglomerated and is of irregular size, only a few boundaries are visible in the focused range. For the sample **Cu1**, particles are agglomerated, but particle boundaries are clearly visible. For the samples **Cu3** and **Cu5**, the size of the particles reduced considerably and the particle boundaries are visible. Since the atomic radius of Cu

is smaller than that of Ba, stress or strain is developed in the lattices which disturb the grain growth process causing it to act as a grain growth inhibitor.

The particle sizes of the Cu doped $BaWO_4$ samples are measured using Image J software. The average particle sizes of the $BaWO_4$ samples are presented in Table 4.4. For sample **S1**, the particles are highly agglomerated, and hence only one particle is visible, the size of that particle is given as the average particle size. The degree of agglomeration and hence the average particle size of the Cu doped $BaWO_4$ samples decreases greatly with the introduction of Cu atoms into the $BaWO_4$ lattice (Figure 4.6 and Table 4.4). The particle size distribution of the samples **Cu3** and **Cu5** is depicted in Figure 4.7.

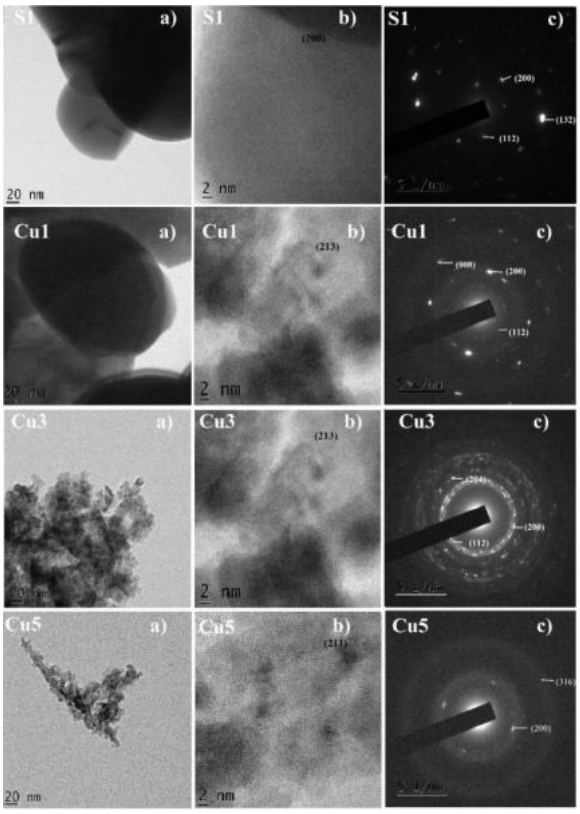

Figure 4.6 a) TEM bright field images, (b) HRTEM images and (c) SAED patterns of pristine and Cu doped $BaWO_4$ samples

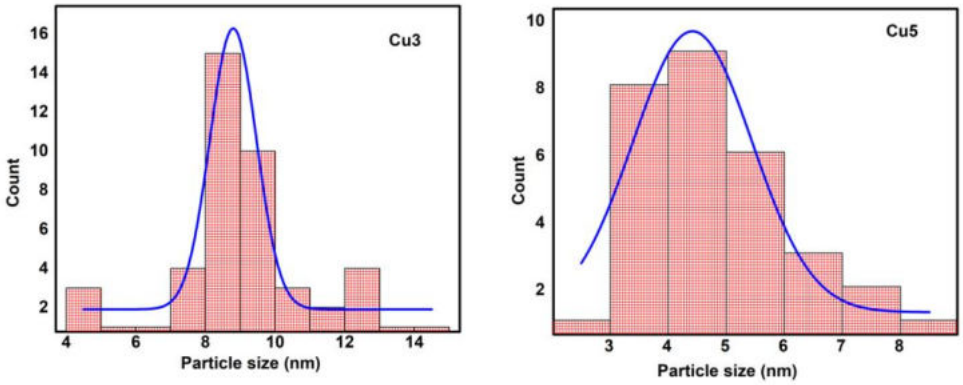

Figure 4.7 Particle size distribution of the samples **Cu3** and **Cu5**

The interplanar distances measured from HRTEM images match with the planes (200), (213), (213), and (211) for the $BaWO_4$ samples **S1**, **Cu1**, **Cu3,** and **Cu5** respectively (Figure 4.6(b)). The crystal lattice fringes observed in HRTEM images, and the bright spots observed in SAED patterns reveal the crystalline nature of the samples [9]. These bright spots are produced by the electrons reflected and diffracted from the different crystallographic planes of unit cells of $BaWO_4$ samples. The SAED pattern of sample **Cu3** (Figure 4.6(c)) consists of a number of diffused rings indicating the presence of nanocrystals with different orientations [10]. The highly polycrystalline nature of the sample **Cu3** is due to the twinning effect caused by the strain developed in the crystals by the doping of the smaller atomic-sized Cu [11].

Table 4.4 Average particle sizes of pristine and Cu doped $BaWO_4$ samples

Sample	Average particle size (nm)	Sample	Average particle size (nm)
S1	108	**Cu3**	9.09
Cu1	104	**Cu5**	4.92

4.3.1.4 FTIR Analysis

The FTIR spectra of the pristine and Cu doped $BaWO_4$ samples in the transmitted mode are recorded using Thermo Nicolet, Avatar 370, and are shown in Figure 4.8. A broad intense peak centred around 820 cm^{-1} is observed, which corresponds to the antisymmetric stretching vibration F2(v3) originating from the W-O in the WO_4^{2-} tetrahedron [12]. As the quantity of Cu in the $BaWO_4$ sample increases, the shapes of the peaks get distorted. This may be due to the distortion or deviation of the tetrahedral shape due to the presence of Cu in the $BaWO_4$ lattice. The bands around 606 cm^{-1} confirm the presence of Cu in the sample, which corresponds to the stretching vibrations of $CuWO_4$ [13,14]. It is also reported that the peak around 600 cm^{-1} correspond to the O-Cu-O antisymmetric vibration [15].

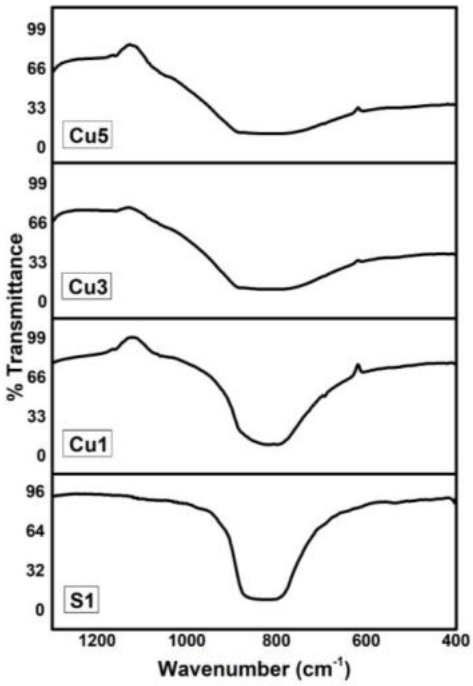

Figure 4.8 FTIR spectra of pristine and Cu doped $BaWO_4$ samples

4.3.1.5 Raman Analysis

Raman spectra of the pristine and Cu doped $BaWO_4$ samples are recorded using Confocal Raman Microscope with AFM to verify the rotational, vibrational and other low-frequency modes of the system, and are depicted in Figure 4.9. A laser beam of wavelength 633 nm is used to excite the samples. The structural order at a short range of a material can be estimated by using Raman active phonon modes. Various Raman modes of $BaWO_4$ are discussed in *Section 3.5*.

As can be seen from Table 4.5, all the Raman modes observed for the pristine and Cu doped $BaWO_4$ samples are characteristics of a tetragonal structure in agreement with the literature available for $BaWO_4$ [16–18]. The small differences obtained for the Raman active modes are due to the changes in crystallite size, and the structural deviations in the lattice caused by the dopant [19]. All the stretching modes are shifted towards the lower frequency side, hence W-O bond length increases and experience a tensile strain due to the substitution of Cu^{2+} ions into the lattice [20,21]. There is a shift in bending modes, which also indicates the change in the W-O coordination. The shift in the external modes confirms the substitution of Ba^{2+} cation by the Cu^{2+} ion in the lattice [22]. The A_g rotational mode is found to decrease due to the introduction of a smaller ionic radius Cu^{2+} ions into the lattice [22]. Raman intensity is found to decrease, and the peaks become broader with the increase in the amount of Cu^{2+} ions in the $BaWO_4$ lattice. The Raman spectra also confirmed that all the Cu doped $BaWO_4$ samples are of scheelite tetragonal structure. Furthermore, all the structural characterization studies confirmed significant variation of structural parameters due to the introduction of Cu^{2+} ions in the $BaWO_4$ lattice.

Table 4.5 Comparison of Raman active modes of pristine and Cu doped $BaWO_4$ samples with theoretical values

Peak/ mode	Value of ω in cm^{-1}				
	Theoretical [17]	Present values of $BaWO_4$ samples			
		S1	**Cu1**	**Cu3**	**Cu5**
$T(B_g)$	55	-	-	-	-
$T(E_g)$	81	75.83	93.118	92.27	90.59
$T(E_g)$	110	101.70	111.40	119.00	110.56
$T(B_g)$	145	-	-	-	-
$R(A_g)$	149	150.60	162.27	162.60	160.07
$R(E_g)$	209	191.13	-	-	-
$\nu_2(A_g)$	328	331.14	327.18	326.34	326.34
$\nu_2(B_g)$	329	332.65	-	-	-
$\nu_4((B_g)$	339	345.60	343.22	343.22	343.22
$\nu_4(E_g)$	348	354.90	388.51	389.35	385.13
$\nu_3(E_g)$	797	795.51	785.46	784.61	782.92
$\nu_3(B_g)$	823	832.03	823.99	823.16	821.47
$\nu_1(A_g)$	928	928.11	917.39	916.27	915.43

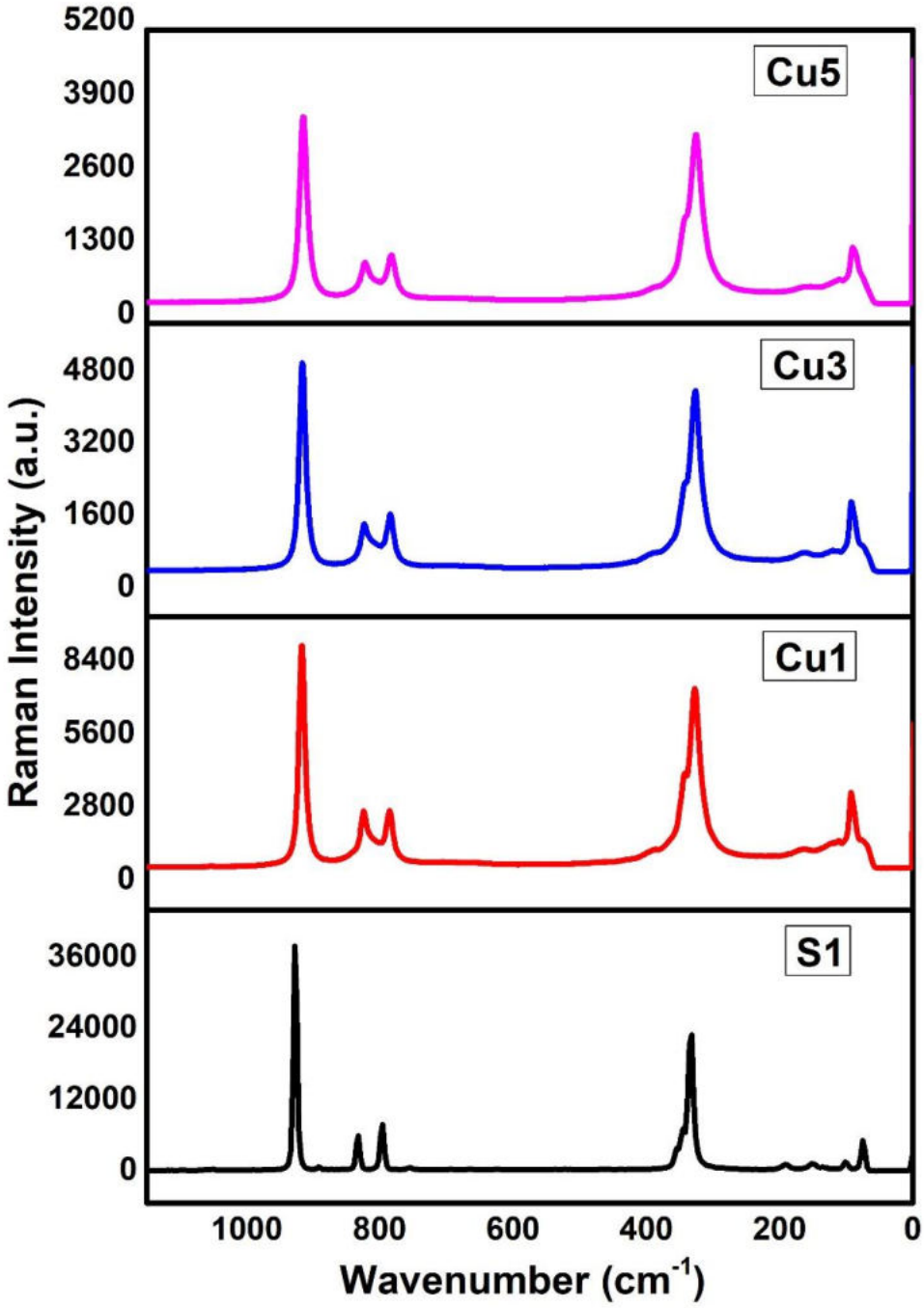

Figure 4.9 Raman spectra of pristine and Cu doped $BaWO_4$ samples

4.3.2 Optical Properties

UV visible absorption spectra and photoluminescence spectra of pristine and Cu doped $BaWO_4$ samples at room temperature are presented here. The analysis of the samples are carried out by following the procedure discussed in *Section 2.5*.

4.3.2.1 UV-visible Analysis

Diffuse reflectance spectra of the pristine and Cu doped $BaWO_4$ samples are taken using Shimadzu 2600 UV- visible spectrophotometer in a wavelength range of 200 to 800 nm. The optical absorption spectra of the pristine and Cu doped $BaWO_4$ samples are obtained by using the Kubelka-Munk transformation equation. The absorbance spectra of the samples are shown in Figure 4.10. Pristine $BaWO_4$ sample shows absorption only in the ultraviolet region (220 nm) corresponding to the ligand to metal charge transfer transition inside the WO_4^{2-} anion [23]. By absorbing the ultraviolet radiation, the excitation from O_{2p} to W_{t2g} in the $(WO_4)^{2-}$ group takes place. Because of the strong interaction between the hole on the oxygen and the electron on the tungsten, they remain together as an exciton in the excited state [23]. For the Cu doped samples, another absorption peak centred at 290 nm appears, which extends to the visible region and the intensity of this additional peak increases with an increase in the concentration of Cu in the sample. In short, the substitution of Cu^{2+} ions in the $BaWO_4$ lattice can influence the bandwidth as well as the optical absorption properties of the sample. This may be due to lattice distortions in the WO_4 tetrahedron as a result of the substitution of Cu^{2+} ions in the $BaWO_4$ lattice resulting in the creation of intermediary energy levels in the sample. A small shift in absorption peak can also be seen in Figure 4.10, which corresponds to the quantum size effect.

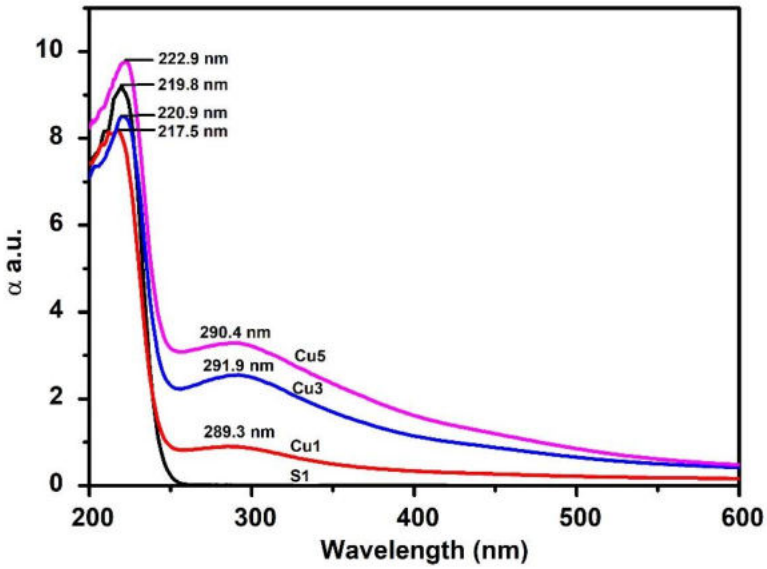

Figure 4.10 Optical absorption spectra of pristine and Cu doped $BaWO_4$ samples

The optical bandgap of the prepared $BaWO_4$ samples is calculated from the optical absorption using the Tauc relation [24]. Figure 4.11 shows the plot of $(\alpha h\upsilon)^2$ versus $h\upsilon$ for the pristine and doped $BaWO_4$ samples. The optical bandgap of the $BaWO_4$ samples is obtained by extrapolating the straight-line portion to the energy axis at zero absorption coefficient. The optical bandgap values obtained for the samples **S1**, **Cu1**, **Cu3** and **Cu5** are 5.25, 5.24, 5.15 and 5.14 eV, respectively. The slight decrease in bandgap with the introduction of Cu in the sample confirms the creation of an energy level or band between the valence and conduction band of the $BaWO_4$ sample (intermediate level). Literature indicated that barium has no significant effect on the optical bandgap of the $BaWO_4$ sample [25]. They only possess a single ligand to metal charge transfer band in the region 218 −274 nm, with a band maximum occurring at 220 − 250 nm. The exact location of this maximum depends on the extend of distortion of the WO_4

tetragonal structure [26]. The electronegativity of Cu lies close to that of W than Ba atom, it can distort the WO_4 tetrahedral structure, and hence the bandgap decreases. Interestingly, the optical bandgap of $BaWO_4$ nanoparticles can be tuned by doping a suitable concentration of Cu.

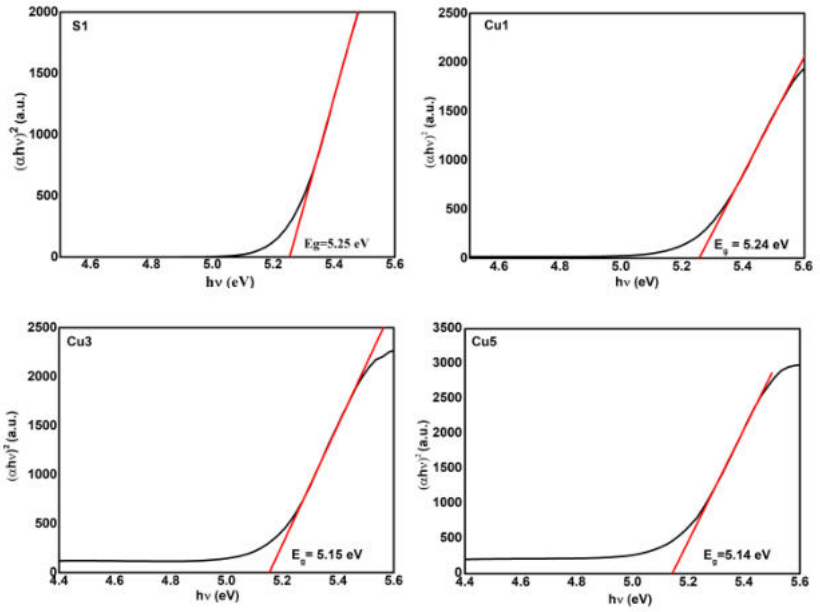

Figure 4.11 Tauc plots of pristine and Cu doped $BaWO_4$ samples

4.3.2.2 Photoluminescence Studies

The photoluminescence spectra of the pristine and Cu doped $BaWO_4$ samples are recorded using Horiba Fluorolog 3 with a Xe- lamp for excitation. Figure 4.12 shows the room-temperature photoluminescence emission spectra of the pristine and Cu doped $BaWO_4$ samples with an excitation wavelength of 350 nm. The broad photoluminescence spectra of the $BaWO_4$ samples indicate that the emission involves a multiphonon process, i.e., a system in which the relaxation occurs by various paths, involving the participation of numerous states. PL emission spectrum is an effective tool in determining the charge separation and

recombination rate of photo-generated electron-hole pairs. It is reported that the blue luminescence in metal tungstate is due to the radiative transition of self-trapped excitons within the $(WO_4)^{2-}$ tetrahedral group [27]. It can be seen from Figure 4.12 that the PL intensity decreases as the percentage of Cu in the sample increases, indicating a decrease in the recombination rate. Thus, the PL spectra also confirm the introduction of intermediate energy levels on Cu doping. This property reveals the enhanced photocatalytic potential of the Cu doped $BaWO_4$ samples.

The PL spectrum of the sample **S1** shows a broad luminescence spectrum with a peak around 435 nm while the doped samples show double peaks. The observed peaks are at 415 and 422 nm for the sample **Cu1**, 415 and 437 nm for samples **Cu3** and **Cu5**. The broad emission peaks correspond to the transition from the degenerate $^3T_1$ ($4d/5d^0$ – $W^{6+}/2p^6$- O^{2-} state) excited state to the $^1A_1$ ($4d/5d^1$- $W^{5+}/2p^5$- O^- state) ground state [28,29]. The splitting of $^3T_1$ is due to the lowering of crystal field symmetry from T_d and the inclusion of spin-orbit interaction. The transition $^3T_1$ to $^1A_1$ is spin forbidden, but it is made allowed by the spin-orbit interaction. The corresponding absorption transition is not observed in the excitation spectrum due to the strong spin selection rule [30]. The quenching of photoluminescence on increasing the content of Cu in the doped $BaWO_4$ samples may be due to the influence of Cu in the spin-orbit interaction. It is also reported that photoluminescence in tungstates is due to the only one allowed transition $^1T_2$ to $^1A_1$ transition [31].

Figure 4.13 shows the fitted curve plots of the photoluminescence spectra of the pristine and doped $BaWO_4$ samples. It can be seen that the relative intensity of emission peak around 412 nm decreases with the increase in the percentage of Cu atoms in the sample.

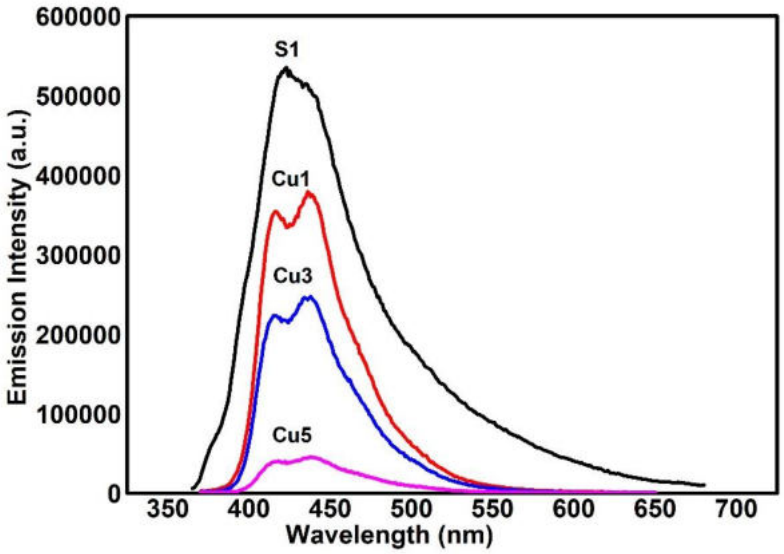

Figure 4.12 PL spectra of pristine and Cu doped $BaWO_4$ samples

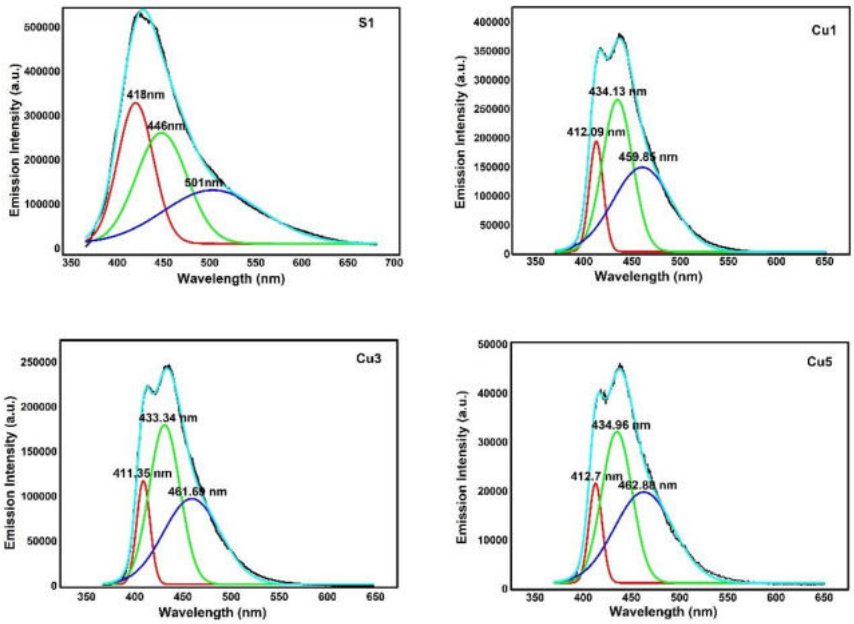

Figure 4.13 Fitted curve plots of the PL spectra of pristine and Cu doped $BaWO_4$ samples

CIE chromaticity coordinate graph and phosphor triangle of the pristine and Cu doped $BaWO_4$ samples are plotted in Figure 4.14. The CIE chromaticity coordinates serve as a standard reference against which many other colour spaces are defined [32]. The obtained CIE chromaticity coordinates of the pristine and Cu doped $BaWO_4$ samples under an excitation wavelength of 350 nm are presented in Table 4.6. The chromaticity coordinates of the sample **S1** lies within the phosphor triangle. The chromaticity coordinates of all the samples indicate unique blue emission with varying intensity. The pristine $BaWO_4$ gives light blue emission, while the Cu doped $BaWO_4$ samples emit dark blue radiation. Thus, Cu doped $BaWO_4$ nanoparticle samples can be used to construct near-ultraviolet light (NUV) excited blue light-emitting diodes. In short, the optical absorption and emission properties of the $BaWO_4$ sample can be tuned by varying the percentage of Cu in the $BaWO_4$ sample.

Table 4.6 CIE chromaticity coordinates of pristine and Cu doped $BaWO_4$ Samples

$BaWO_4$ samples	CIE coordinates	
	x	y
S1	0.191	0.181
Cu1	0.154	0.073
Cu3	0.154	0.075
Cu5	0.167	0.094

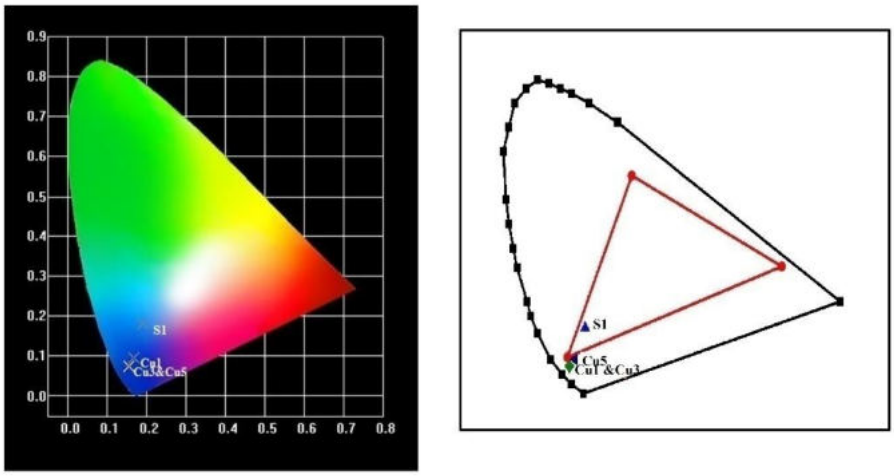

Figure 4.14 CIE chromaticity diagram and phosphor triangle of pristine and Cu doped $BaWO_4$ samples

4.3.3 Magnetic Studies

The magnetic behaviour of the pristine and Cu doped $BaWO_4$ samples is drawn by taking measurements with a vibrating sample magnetometer (Lakeshore VSM 7410) at room temperature in an applied magnetic field sweeping between ± 15000 Oe. The magnetic hysteresis loops of the samples are plotted by taking the variation of magnetization (M) in emu/gm as a function of the applied magnetic field and is shown in Figure 4.15. The magnetic properties of the sample strongly depend on the synthesis route, calcination temperature, and the substitution of metal ions in the crystal lattice. The saturation magnetization, coercivity, retentivity, and squareness ratio R of the pristine and Cu doped $BaWO_4$ samples obtained from the hysteresis loop are presented in Table 4.7. It can be seen that pristine $BaWO_4$ is ferromagnetic in nature and as the amount of Cu in the sample increases, its magnetic behaviour changes appreciably (Figure 4.15 and Table 4.7). As seen from the figure, $BaWO_4$ samples **S1** and **Cu1** exhibit weak

ferromagnetic behaviour, whereas samples **Cu3** and **Cu5** do not exhibit hysteresis showing the property of superparamagnetism. Superparamgnetism is a property exhibited by sufficiently small ferromagnetic single domain nanoparticles in which the magnetization can randomly flip direction within the Neel relaxation time under the influence of temperature. In the absence of an external magnetic field, their average value of magnetization appears to be zero. Since the size of the nanoparticles reduces considerably on doping as evident from the TEM images, the magnetic property of the samples changes from ferromagnetic to superparamagnetic [33]. Superparamagnetic particle is preferred in biomedical applications, because of the zero magnetization at room temperature and the sizes are comparable to the targeted entities [34–36]. In short, the ferromagnetic nature of the $BaWO_4$ sample changes to superparamagnetic when doped with higher concentrations of Cu, which makes them useful for various biomedical applications such as drug delivery, MRI contrast agents and biosensors [34,36].

The magneto crystalline anisotropy constant and the magnetic moment in Bohr magneton are calculated using the following equations [37][38].

$$Anisotropy\ constant = \frac{Hc \times Ms}{0.96} \tag{4.1}$$

$$Magnetic\ moment\ in\ Bohr\ magneton = \frac{M \times Ms}{5585} \tag{4.2}$$

Where M is the molecular weight of the samples, Ms the saturation magnetization, and Hc the coercivity of the samples calculated from the M-H loop. The saturation magnetization, coercivity, retentivity, squareness ratio R, anisotropy constant, and magnetic moment of the pristine and Cu doped $BaWO_4$ samples varies in an irregular manner with the increase of the percentage of Cu, as evident from the comparison Table 4.7. As the squareness ratios of the samples are less than 0.5, the $BaWO_4$ nanoparticles are single domain magnetic particles [39].

Table 4.7 Comparison of magnetic properties of pristine and Cu doped $BaWO_4$ samples

Sample	Saturation magnetization(Ms) (emu/gm)	Coercivity (Oe)	Retentivity (Mr) (emu/gm)	Squareness ratio R=Mr/Ms	Anisotropy constant (ergs/Oe)	Magnetic moment (Bohr Magneton)
S1	25.776×10^{-3}	52.583	0.539×10^{-3}	0.02109	1.41185	1.777×10^{-3}
Cu1	31.102×10^{-3}	29.067	0.552×10^{-3}	0.01775	0.94171	2.141×10^{-3}
Cu3	17.135×10^{-3}	8.673	0.83×10^{-3}	0.04844	0.15480	1.175×10^{-3}
Cu5	34.742×10^{-3}	-8.32	0.313×10^{-3}	0.00901	-0.301097	2.373×10^{-3}

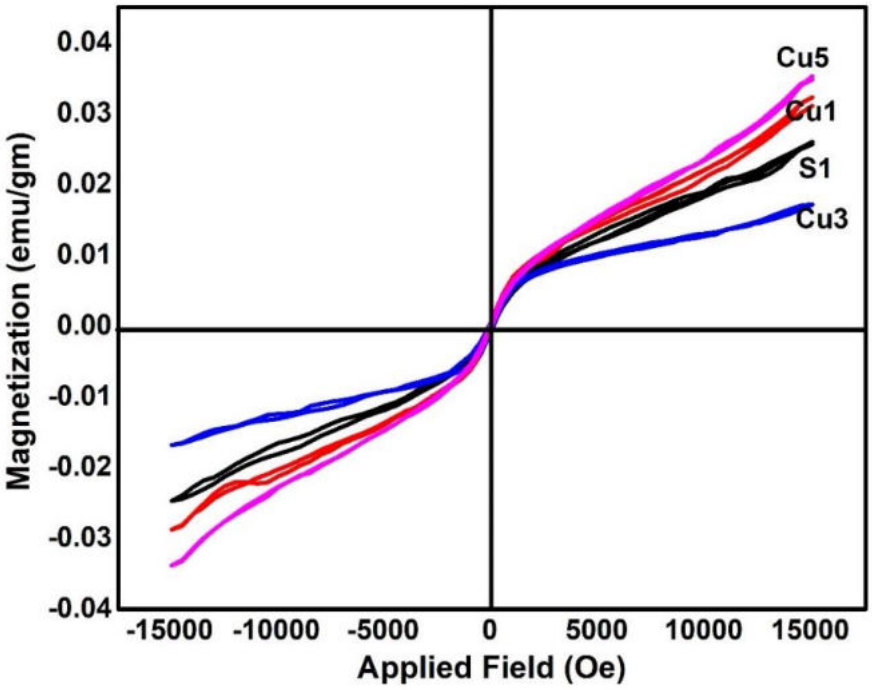

Figure 4.15 M H loop of pristine and Cu doped $BaWO_4$ samples

4.4 Conclusion

- The pristine and Cu substituted nanocrystalline barium tungstate nanoparticles are prepared by a simple chemical precipitation route.
- A systematic study is conducted on the effect of Cu doping on the structural, optical, and magnetic properties of crystalline $BaWO_4$.
- The XRD and Raman spectral studies confirm the scheelite tetrahedral structure for the Cu doped $BaWO_4$ samples with a space group $I4_1/a$.
- A dramatic change in the morphology of the $BaWO_4$ sample is observed when doped with Cu atoms.
- The optical absorption extends to the visible region and hence the optical bandgap energy of the samples decreases with the introduction of Cu atoms into the $BaWO_4$ samples. The intensity of absorption increases with the increase in the concentration of the dopant.
- The PL emission spectra with significant modifications are observed for Cu doped $BaWO_4$ nanoparticles. The PL emission spectra along with the CIE chromaticity diagram confirm the use of the prepared samples for fluorescent applications.
- The VSM studies confirm significant deviations of magnetic parameters for the Cu doped $BaWO_4$ samples from the pristine sample. As the doping concentration of Cu increases, the ferromagnetic nature of $BaWO_4$ samples changes to paramagnetic behaviour.

References

[1] M. Nikl, P. Bohacek, E. Mihokova, M. Kobayashi, M. Ishii, Y. Usuki, V. Babin, A. Stolovich, S. Zazubovich, M. Bacci, Excitonic emission of scheelite tungstates AWO_4 (A = Pb, Ca, Ba, Sr), J. Lumin. 87 (2000) 1136–1139.

[2] P. Černý, P.G. Zverev, H. Jelínková, T.T. Basiev, Efficient Raman shifting of picosecond pulses using $BaWO_4$ crystal, Opt. Commun. 177 (2000) 397–404.

[3] Y. Wang, W. Duan, B. Liu, X. Chen, F. Yang, J. Guo, The effects of doping copper and mesoporous structure on photocatalytic properties of TiO, J. Nanomater. 2014 (2014) 1–7.

[4] S.K. Stephen, T. Varghese, Structural modifications and extended spectral response of nanocrystalline $Ba_{1-x}Cu_xWO_4$ samples, Mater. Chem. Phys. 258 (2021) 123901 1–13.

[5] C. Suryanarayana, M.G. Norton, X-ray diffraction : A Practical Approach, Plenum Press, 1998.

[6] G.K. Williamson, W.H. Hall, X-Ray broadening from filed aluminium and tungsten, Acta Metall. 1 (1953) 22–31.

[7] A.K. Ambast, A.K. Kunti, S. Som, S.K. Sharma, Near-white-emitting phosphors based on tungstate for phosphor-converted light-emitting diodes, Appl. Opt. 52 (2013) 8424–8431.

[8] P. Jena, S.K. Gupta, N.K. Verma, A.K. Singh, R.M. Kadam, Energy transfer dynamics and time resolved photoluminescence in $BaWO_4:Eu^{3+}$

nanophosphors synthesized by mechanical activation, New J. Chem. 41 (2017) 8947–8958.

[9] X. Liu, W. Hou, X. Yang, Q. Shen, Pure-phase $La_2(WO_4)_3:Eu^{3+}$ nanocrystals and spindle-like $NaLa(WO_4)_2:Yb^{3+}/Er^{3+}$ nano/microcrystals: Selective synthesis, morphologies and photoluminescent properties, Dalt. Trans. 42 (2013) 11445–11454.

[10] S. Vidya, S. Solomon, J.K. Thomas, Synthesis, characterization, and low temperature sintering of nanostructured $BaWO_4$ for optical and LTCC applications, Adv. Condens. Matter Phys. 2013 (2013) 1–11.

[11] G. Yang, S.J. Park, Deformation of single crystals, polycrystalline materials, and thin films: A review, Materials (Basel). 12 (2019) 1–18.

[12] S. Khademolhoseini, S. Ali Zarkar, Preparation and characterization of barium tungstate nanoparticles via a new simple surfactant-free route, J. Mater. Sci. Mater. Electron. 27 (2016) 9605–9609.

[13] S.M. Pourmortazavi, M. Rahimi-Nasrabadi, M. Khalilian-Shalamzari, H.R. Ghaeni, S.S. Hajimirsadeghi, Facile chemical synthesis and characterization of copper tungstate nanoparticles, J. Inorg. Organomet. Polym. Mater. 24 (2014) 333–339.

[14] M. Mohammadikish, M. Masteri-Farahani, T. Mahdian, Optical properties of copper tungstate nanoparticles prepared by microemulsion method, Inorg. Nano-Metal Chem. 49 (2019) 63–68.

[15] I. V Olivante, Materials science Research trends, Nova Science Publishers Inc, 2008.

[16] F.J. Manjón, D. Errandonea, N. Garro, J. Pellicer-Porres, P. Rodríguez-Hernández, S. Radescu, J. López-Solano, A. Mujica, A. Muñoz, Lattice dynamics study of scheelite tungstates under high pressure I. $BaWO_4$, Phys. Rev. B - Condens. Matter Mater. Phys. 74 (2006) 1–17.

[17] T.T. Basiev, A.A. Sobol, Y.K. Voronko, P.G. Zverev, Spontaneous Raman spectroscopy of tungstate and molybdate crystals for Raman lasers, Opt. Mater. (Amst). 15 (2000) 205–216.

[18] S.P.S. Porto, J.F. Scott, Raman spectra of $CaWO_4$, $SrWO_4$, $CaMoO_4$, and $SrMoO_4$, Phys. Rev. 157 (1967) 716–719.

[19] D. Rangappa, T. Fujiwara, M. Yoshimura, Synthesis of highly crystallized $BaWO_4$ film by chemical reaction method at room temperature, Solid State Sci. 8 (2006) 1074–1078.

[20] S. Liang, M.N. Hasan, J.H. Seo, Direct observation of raman spectra in black phosphorus under uniaxial strain conditions, Nanomaterials. 9 (2019) 1–8.

[21] A. Jayaraman, B. Batlogg, L.G. Vanuitert, High-pressure Raman study of alkaline-earth tungstates and a new pressure-induced phase transition in $BaWO_4$, Phys. Rev. B. 28 (1983) 4774–4777.

[22] P. Tarte, M. Liegeois-Duyckaerts, Vibrational studies of molybdates, tungstates and related compounds-I. New infrared data and assignments for the scheelite-type compounds $XIIMoO_4$ and $XIIWO_4$, Spectrochim. Acta Part A Mol. Spectrosc. 28 (1972) 2029–2036.

[23] S.M. Zawawi, R. Yahya, A. Hassan, H.E. Mahmud, M.N. Daud, Structural and optical characterization of metal tungstates (MWO_4; M = Ni, Ba, Bi) synthesized by a sucrose-templated method, Chem. Cent. J. 7 (2013) 1–10.

[24] D.L. Wood, J. Tauc, Weak absorption tails in amorphous semiconductors, Phys. Rev. B. 5 (1972) 3144–3151.

[25] M. Tyagi, S.G. Singh, A.K. Chauhan, S.C. Gadkari, First principles calculation of optical properties of $BaWO_4$: A study by full potential method, Phys. B Condens. Matter. 405 (2010) 4530–4535.

[26] E.I. Ross-Medgaarden, I.E. Wachs, Structural determination of bulk and surface tungsten oxides with UV-vis diffuse reflectance spectroscopy and raman spectroscopy, J. Phys. Chem. C. 111 (2007) 15089–15099.

[27] G. Blasse, Classical phosphors: A Pandora's box, J. Lumin. 72–74 (1997) 129–134.

[28] A. Phuruangrat, T. Thongtem, S. Thongtem, Barium molybdate and barium tungstate nanocrystals synthesized by a cyclic microwave irradiation, J. Phys. Chem. Solids. 70 (2009) 955–959.

[29] G. Benoît, J. Véronique, A. Arnaud, G. Alain, Luminescence properties of tungstates and molybdates phosphors: Illustration on $ALn(MO_4)_2$ compounds (A = alikaline cation, Ln = lanthanides, M = W, Mo), Solid State Sci. 13 (2011) 460–467.

[30] S. Shigeo, W. M. Yen, H. Yamamoto, Phosphor Handbook, CRC Press, Taylor and Francis Group, 2007.

[31] A. Phuruangrat, T. Thongtem, S. Thongtem, Synthesis, characterisation and photoluminescence of nanocrystalline calcium tungstate, J. Exp. Nanosci. 5 (2010) 263–270.

[32] N. Kohei, S. Suekokanaya, Color Vision, in: S. Shigeo, Y.M. William, Yamamoto Hajime (Eds.), Phosphor Handb., 2nd ed., CRC Press, Taylor and Francis Group, 2007.

[33] V. Marghussian, Magnetic properties of nano-glass ceramics, Nano-Glass Ceramics (2015) 181–223.

[34] J.S. Lee, J.M. Cha, H.Y. Yoon, J.K. Lee, Y.K. Kim, Magnetic multi-granule nanoclusters: A model system that exhibits universal size effect of magnetic coercivity, Sci. Rep. 5 (2015) 1–7.

[35] Wahajuddin, S. Arora, Superparamagnetic iron oxide nanoparticles: Magnetic nanoplatforms as drug carriers, Int. J. Nanomedicine. 7 (2012) 3445–3471.

[36] Y. Xiao, J. Du, Superparamagnetic nanoparticles for biomedical applications, J Mater Chem B. (2020) 354–367.

[37] R.C. Kambale, P.A. Shaikh, S.S. Kamble, Y.D. Kolekar, Effect of cobalt substitution on structural, magnetic and electric properties of nickel ferrite, J. Alloys Compd. 478 (2009) 599–603.

[38] M. Ahmad, M. Ahmad, I. Ali, W. Ahmad, G. Mustafa, M.N. Akhtar, A. Ali, G. Abbas, M.U.D. Rana, Temperature dependent structural and magnetic behavior of Y-type hexagonal ferrites synthesized by sol-gel autocombustion, J. Alloys Compd. 651 (2015) 749–755.

[39] Y. Slimani, H. Güngüneş, M. Nawaz, A. Manikandan, H.S. El Sayed, M.A. Almessiere, H. Sözeri, S.E. Shirsath, I. Ercan, A. Baykal, Magneto-optical and microstructural properties of spinel cubic copper ferrites with Li-Al co-substitution, Ceram. Int. 44 (2018) 14242–14250.

Chapter 5

EFFECT OF YTTERBIUM DOPING ON THE PROPERTIES OF NANOCRYSTALLINE $BaWO_4$

The effect of ytterbium (Yb) doping on the structural, optical, and magnetic properties of nanocrystalline $BaWO_4$ is dealt with in this chapter. 1, 3, and 5 mol % of Yb doped $BaWO_4$ are synthesized by the chemical precipitation method and characterized using various characterization techniques.

5.1 Introduction

Alkaline metal tungstates AWO_4 (A = Ca^{2+}, Ba^{2+}, and Sr^{2+}) doped/co-doped with rare earth ions are interesting host materials among researchers due to their strong thermal and chemical stability, and good nonlinear optical properties [1–3]. The doping will also have resulted in a change in size, optical bandgap, emission colour, and lattice variations yielding new applications. Rare earth activated tungstate materials have excellent photo-stabilities, large Stokes/anti-Stokes shifts, long luminescence life times, and sharp band emissions [4].

Among rare earth elements, Yb^{3+} ion is obtaining a lot of attention as an active dopant ion for wavelength tunable solid-state laser materials, high power lasers, scintillators or as a structural probe in solids [5]. Yb^{3+} has a strong absorption peak at 980 nm, at the same wavelength of the light emitted from InGaAs laser, with no absorption in the visible range. Thus, it is a promising material for producing a non-Nd lasing centre in the same range of emission wavelength [6]. The transition between energy levels of ytterbium leads to an intense and broad emission in the IR region with a longer life time than the Nd^{3+} doped materials [7]. The Yb^{3+} has also been investigated as a sensitizer to activate other lanthanide ions for up-conversion luminescence by absorbing 980 nm photons [8–10] and as the spectral converter in Ln^{3+}-Yb^{3+} doubly doped quantum cutting phosphors for high-efficiency Si photovoltaics (the emission of Yb^{3+} at ~ 1000 nm perfectly matches the maximum spectral response of Si solar cells) [11]. It has a simple electronic structure with two states, $^2F_{7/2}$ fundamental and $^2F_{5/2}$ excited, separated by energy of about 10000 cm^{-1}. Since the 4*f* electrons of Yb^{3+} are less shielded than other ions of the lanthanide series, these electrons show a higher tendency to interact with the lattice and the neighbouring atoms. Cooperative interactions with the lattice and neighbouring atoms and the vibronic broadening are observed in a variety of Yb^{3+} activated systems [4,12]. Such types of interactions can be between two Yb atoms, and it is reported that Yb-Yb pair interaction produces visible emission [13].

The simple energy level structure of Yb^{3+} prevents the existence of several de-excitation processes that influence the dynamics of populations of the energy levels in other rare earth laser ions with more complex electronic structure, such as the excited state absorption or the concentration quenching by down-conversion cross-relaxation or up-conversion inside the system of active ions [5].

In addition to the unique energy-level structure, Yb^{3+} also has a unique $4f^{13}$ electronic configuration, which can easily gain one electron to reach the more stabilized $4f^{14}$ configuration of the full shell. This tendency of reduction to Yb^{2+} enables the Yb^{3+} ion in some hosts, such as oxides [14], fluorides, nitrides [15], and oxysulfides [16], to receive an electron from the host's anion under high-energy external excitation (ultraviolet light), forming a charge transfer state. The charge transfer state of Yb^{3+} can transfer the excitation energy to the $^2F_{5/2}$ emitting state via a non-radiative relaxation process giving NIR photoluminescence at around 1000 nm.

This chapter deals with the effect of Yb^{3+} doping on the structural, morphological, optical absorption and bandgap, near infrared (NIR) photoluminescence emission, and magnetic properties of $BaWO_4$ nanostructures prepared by chemical precipitation route.

5.2 Synthesis of Ytterbium Doped $BaWO_4$

Barium nitrate ($Ba(NO_3)_2$) (99%, Merk), ytterbium nitrate ($Yb(NO_3)_3.5H_2O$) (99.9%, Sigma Aldrich), and sodium tungstate ($Na_2WO_4.2H_2O$) (98%, Merk) were used without further purification for the synthesis of Yb doped $BaWO_4$ sample. Chemical precipitation was performed without using any capping agents or surfactants. 0.1 M solutions of barium nitrate and ytterbium nitrate were mixed together in the desired ratios, (1, 3, and 5% ytterbium nitrate). 0.1 M solution of sodium tungstate was slowly added to the mixture by continuously stirring at room temperature for half an hour with the help of a magnetic stirrer apparatus. The white precipitate obtained was washed well and dried for 24 h in a hot air oven at 80 $^{\circ}$C. The dried powder of Yb doped $BaWO_4$ was pulverized well and calcined at 400 $^{\circ}$C in the presence of air for 3 h. The $BaWO_4$ samples doped

with 1, 3, and 5 mol% ytterbium are denoted as **Yb1**, **Yb3,** and **Yb5** respectively. Synthesis of pristine $BaWO_4$ sample **S1** is described in *Section 3.2*.

5.3 Results and Discussion

The structural, optical and magnetic characterizations of the Yb doped $BaWO_4$ samples are carried out using various techniques described in *Chapter 2*. The data for the pristine $BaWO_4$ sample **S1** is taken from *Chapter 3*.

5.3.1 Structural Characterization

The structural characterization of the synthesized Yb doped $BaWO_4$ samples is carried out using powder X-ray diffraction, scanning electron microscopy, energy dispersive X-ray analysis, transmission electron microscopy, Fourier transform infrared spectroscopy and Raman spectroscopy by following the procedure adopted in *Section 2.4*.

5.3.1.1 Powder XRD Analysis

The Powder XRD patterns of the pristine and Yb doped $BaWO_4$ samples for different concentrations of Yb are shown in Figure 5.1. The diffraction peaks of all the Yb doped $BaWO_4$ samples match with the peaks in the JCPDS Card no. 72-0746 of $BaWO_4$. It can be seen that all the $BaWO_4$ samples crystallize in a body-centred tetragonal structure of scheelite type with space group $I4_1/a$. The intensities corresponding to the different planes are compared to the JCPDS values. The preferential orientation for all the Yb doped $BaWO_4$ samples is (1 1 2), similar to the pristine $BaWO_4$ sample. The intensity of the peaks observed decreases with an increase in the percentage of Yb and the FWHM increases with an increase in the percentage of Yb up to 3% and then vice-versa. The well-defined sharp diffraction peaks of the pristine and Yb doped $BaWO_4$ samples

indicate their purity and crystallinity. No glimpse of any extra-phase in any of the doped samples indicating that the doped Yb^{3+} ions can be diffused into the $BaWO_4$ host lattice without significant changes to the host structure. Lattice parameters of the pristine and doped $BaWO_4$ samples are calculated using the plane spacing equation for tetragonal structure as described in *Section 2.4.1*.

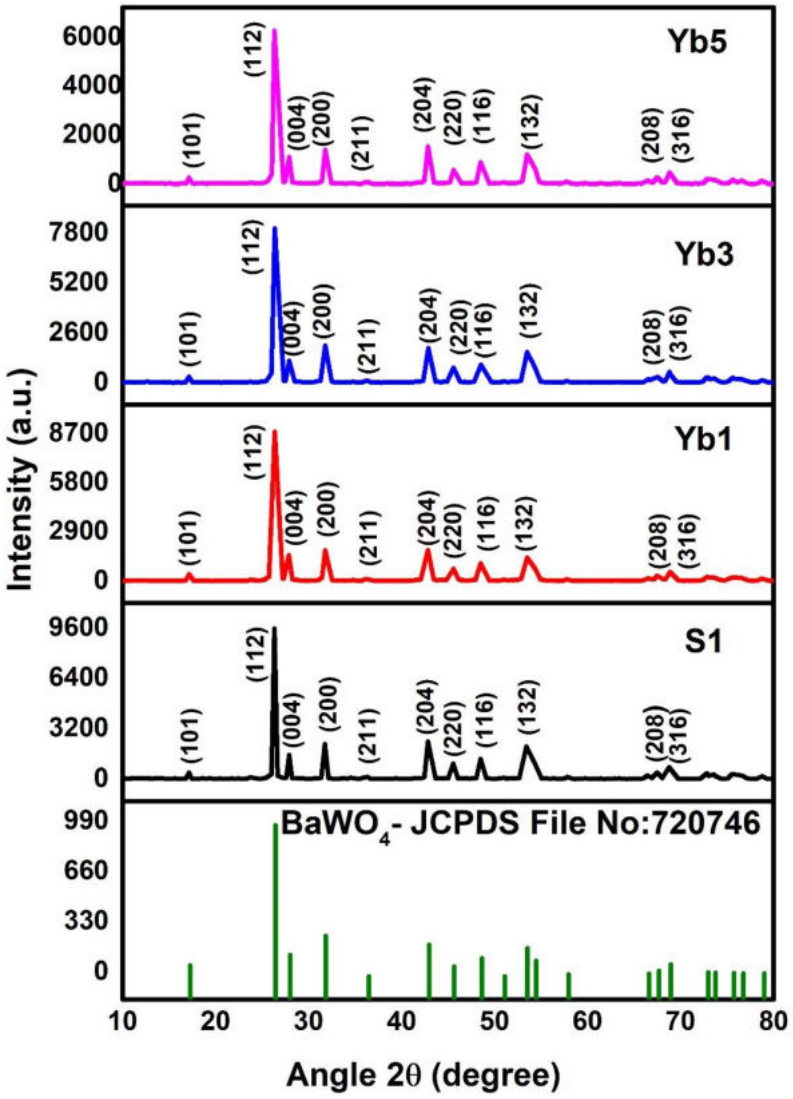

Figure 5.1 XRD patterns of pristine and Yb doped $BaWO_4$ samples

The crystallite sizes of the pristine and Yb doped $BaWO_4$ samples are estimated using the Scherrer equation, as described in *Section 2.4.1*. The crystallite size and micro-strain of the pristine and Yb doped samples are also estimated by Williamson-Hall analysis (Figure 5.2). The obtained lattice parameters, unit cell volume, and crystallite size of the pristine and Yb^{3+} doped $BaWO_4$ samples are tabulated in Table 5.1. The results agree with the JCPDS Card no. 72-0746. The (h k l) values of the protruding peaks are shown in the XRD patterns. The Yb^{3+} doped $BaWO_4$ samples show no significant change in the XRD patterns. Hence, there is no change in the tetragonal structure of the $BaWO_4$ lattice due to the incorporation of Yb^{3+} ions. When Yb^{3+} ions are substituted into the $BaWO_4$ host lattice, as the ionic radius of Yb^{3+} ion (0.985 Å) is slightly smaller than the ionic radius of Ba^{2+} ion (1.42 Å) with eight coordination numbers, they could adapt to the S_4 site symmetry environment of Ba^{2+} ions and occupy the Ba^{2+} site in the $BaWO_4$ lattice. Slight variations in lattice parameters is observed, which can be due to the lattice distortions that occurred when doped with Yb^{3+} ions [17]. Most of the peaks are shifted towards the higher angle side on increasing the amount of Yb in the sample. However, the peaks are slightly shifted towards the lower angle side for the sample **Yb5,** which indicates the presence of a strain in the sample. In short, the trivalent lanthanide ion Yb^{3+} provides a particularly favourable situation for substitution in the Ba^{2+} site with isostructural replacement.

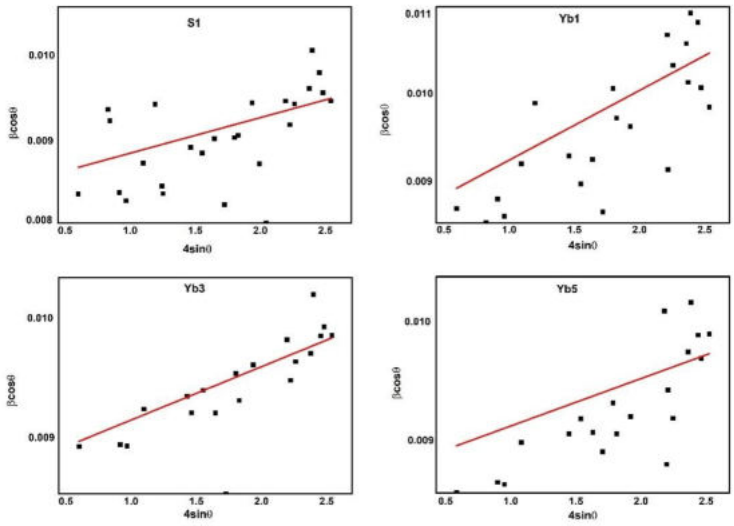

Figure 5.2 Williamson-Hall plots of pristine and Yb doped $BaWO_4$ samples

Table 5.1 Geometric parameters of pristine and Yb doped $BaWO_4$ samples

Sample	a = b (Å)	c (Å)	Unit cell volume (Å^3)	Crystallite size (nm)		Micro-strain $\times10^{-3}$
				Scherrer method	W-H method	
S1	5.589	12.66	395.45	13.15	14.56	0.149
Yb1	5.622	12.79	404.13	11.19	12.23	0.246
Yb3	5.622	12.77	403.89	11.11	11.88	0.211
Yb5	5.621	12.78	403.93	13.31	13.34	0.189

Rietveld refinement of the samples is performed to investigate the effect of Yb doping on the structural parameters of the $BaWO_4$ lattice. Double Voigt is used for peak profile fitting. All the refinement results indicated that the samples displayed a pure scheelite-type tetragonal phase with space group I41/a (88) and point group symmetry C_{4h}^6. Refined parameters of the pristine and Yb doped $BaWO_4$ samples are shown in Table 5.2. The refinement output is displayed in Figure 5.3.

Table 5.2 Structural parameters and refined data of pristine and Yb doped $BaWO_4$ samples

Sample	Atoms	x	y	z	a=b Å	c Å	Unit cell volume Å^3	R_{wp}	R_p	R_e	GOF
S1	Ba	0.0000	0.2500	0.6250	5.621	12.741	402.62	9.71	7.38	6.66	1.45
	W	0.0000	0.2500	0.1250							
	O	0.1259	0.0056	0.2097							
Yb1	Ba	0.0000	0.2500	0.6250	5.616	12.754	402.27	8.57	6.54	6.42	1.33
	W	0.0000	0.2500	0.1250							
	O	0.1239	0.0138	0.2075							
Yb3	Ba	0.0000	0.2500	0.6250	5.616	12.746	402.08	9.2	6.96	6.45	1.42
	W	0.0000	0.2500	0.1250							
	O	0.1160	0.0120	0.2188							
Yb5	Ba	0.0000	0.2500	0.6250	5.617	12.749	402.31	7.85	5.86	6.9	1.13
	W	0.0000	0.2500	0.1250							
	O	0.1263	0.0000	0.2080							

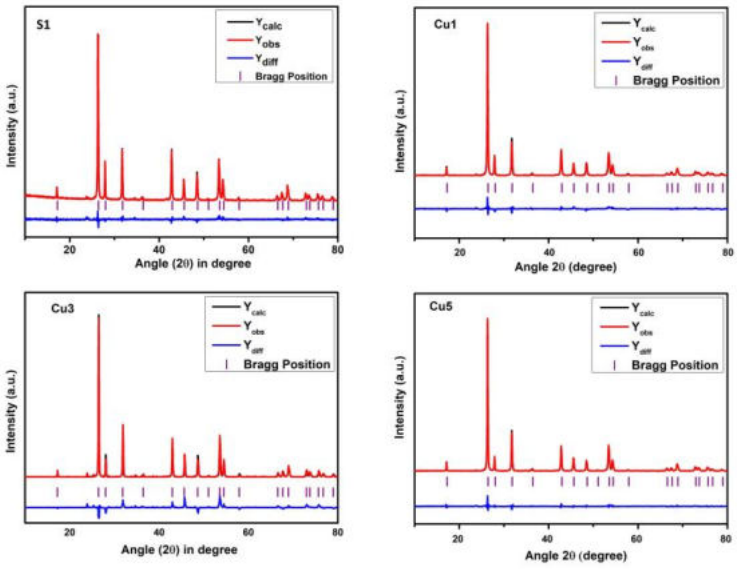

Figure 5.3 Observed, calculated and the difference XRD patterns of the pristine and Yb doped $BaWO_4$ samples

5.3.1.2 SEM and EDX Analysis

Figure 5.4 depicts the SEM images of the pristine and Yb doped $BaWO_4$ samples. The SEM micrographs show a number of bipyramidal and flower-like structures. The SEM photograph represents the topography and surface morphology of the highly agglomerated $BaWO_4$ particles with voids. The morphology of the sample changes to a flower-like structure with the incorporation of Yb atoms into it. Pristine $BaWO_4$ sample is found to be highly porous or spongy nature. The obtained $BaWO_4$ microstructures have non-uniform sizes and shapes. By the substitution of Ba^{2+} ions by Yb^{3+} ions in the $BaWO_4$ lattice, the porosity or the size of the pores found to decrease. Small floccules are found on the surface of the images, and it increases with the quantity of Yb in the samples. The change in the topography and surface morphology of the Yb doped $BaWO_4$ samples may have a significant effect on the electrical and optical properties of the material.

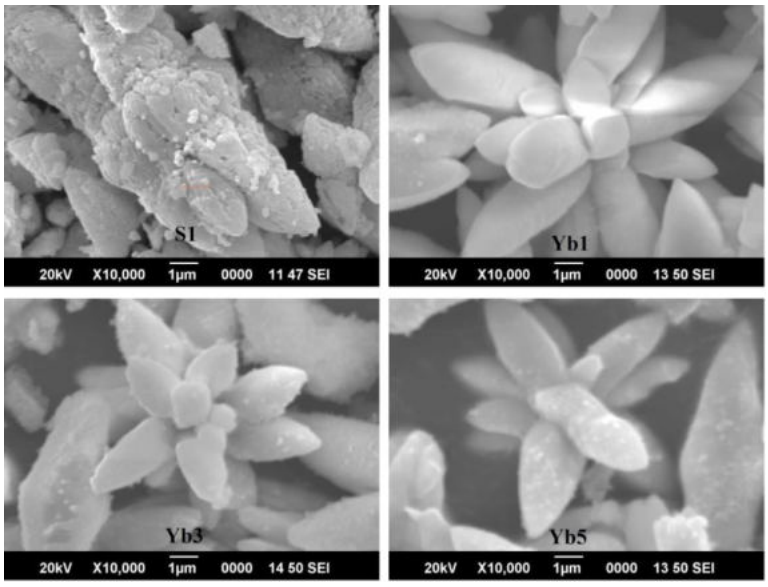

Figure 5.4 SEM images of pristine and Yb doped $BaWO_4$ samples

The EDX spectra (Figure 5.5) of the pristine and Yb doped $BaWO_4$ samples are taken for elemental analysis. The existence of elements Ba, W, O, and Yb in the samples are confirmed by the energy dispersive X-ray analysis. The elemental composition of the pristine and Yb doped $BaWO_4$ samples is presented in Table 5.3. The presence of Yb in the EDX spectra confirms the successful incorporation of Yb atoms into the $BaWO_4$ lattice. The absence of other elemental peaks in the EDX spectra (Figure 5.5 and Table 5.3) reveals the purity of the prepared samples.

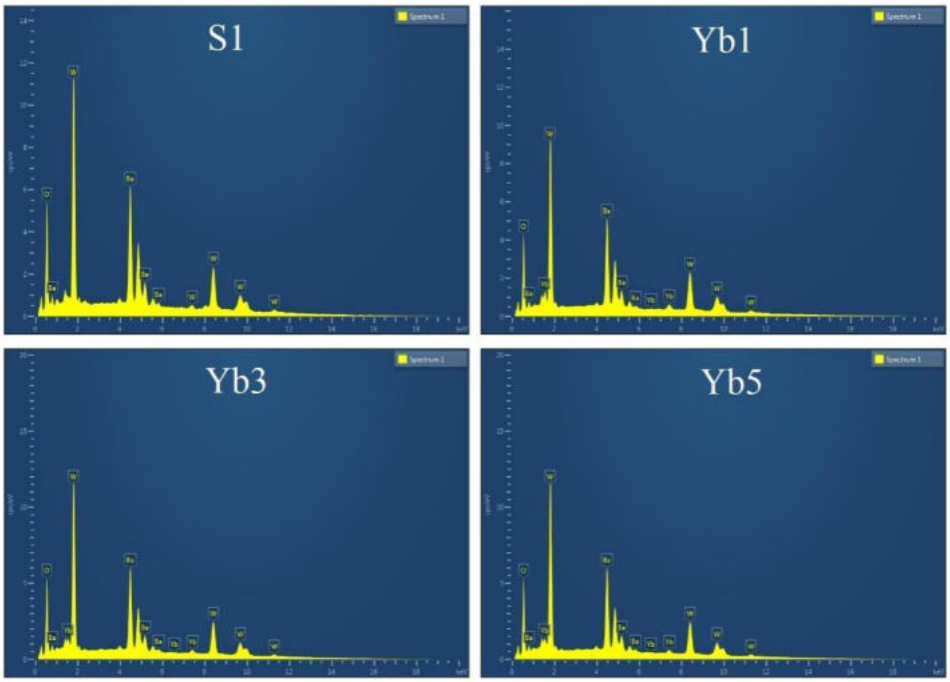

Figure 5.5 EDX spectra of pristine and Yb doped $BaWO_4$ samples

Table 5.3 Elemental composition of pristine and Yb doped $BaWO_4$ samples

sample	Element	Line Type	Mass %	Atomic %
S1	O	K series	18.92	70.43
	Ba	L series	30.05	13.03
	W	L series	51.03	16.53
	Yb	-	0	0
Yb1	O	K series	15.89	64.49
	Ba	L series	41.23	20.05
	W	M series	41.87	14.90
	Yb	L series	1.01	0.56
Yb3	O	K series	15.59	64.62
	Ba	L series	39.92	19.28
	W	M series	42.07	15.17
	Yb	L series	2.42	0.93
Yb5	O	K series	14.84	63.23
	Ba	L series	40.71	20.21
	W	M series	40.86	15.15
	Yb	L series	3.6	1.42

5.3.1.3 TEM Analysis

TEM bright-field images, HRTEM images and SAED patterns of pristine and Yb doped $BaWO_4$ samples are shown in Figure 5.6. TEM images reveal that the size and morphology of the $BaWO_4$ samples changes with the introduction of Yb^{3+} ions into the $BaWO_4$ lattice. In the TEM bright-field image (Fig. 5.6a), the pristine and the Yb doped $BaWO_4$ nanoparticles have spherical or oval like morphology. The spherical phosphors have a minimum surface area which helps

to minimize the light scattering on the surface and thus improve the efficiency of light emission and the brightness of such a phosphor [17–19]. In the doped samples, the particles get agglomerated, but the size of the nanoparticles is small compared to the pristine $BaWO_4$ sample. In doped $BaWO_4$ samples, the stress or strain caused due to the doping of Yb atoms with a smaller atomic radius inhibits the grain growth. TEM images also clearly reveal the voids and the porous nature of the samples.

The average particle sizes of the pristine and doped $BaWO_4$ samples are measured using Image J software and are presented in Table 5.4. The particle size distribution of Yb doped $BaWO_4$ samples is shown in Figure 5.7. The interplanar distances measured from HRTEM images match with the planes (200), (200), (204) and (213) respectively for the samples **S1**, **Yb1**, **Yb3**, and **Yb5**. The bright rings observed in the SAED pattern reveal the polycrystalline nature of the samples.

Table 5.4 Particle size of pristine and Yb doped $BaWO_4$ samples

Sample	Average particle size (nm)	Sample	Average particle size (nm)
S1	108	**Yb3**	12.85
Yb1	15.21	**Yb5**	11.21

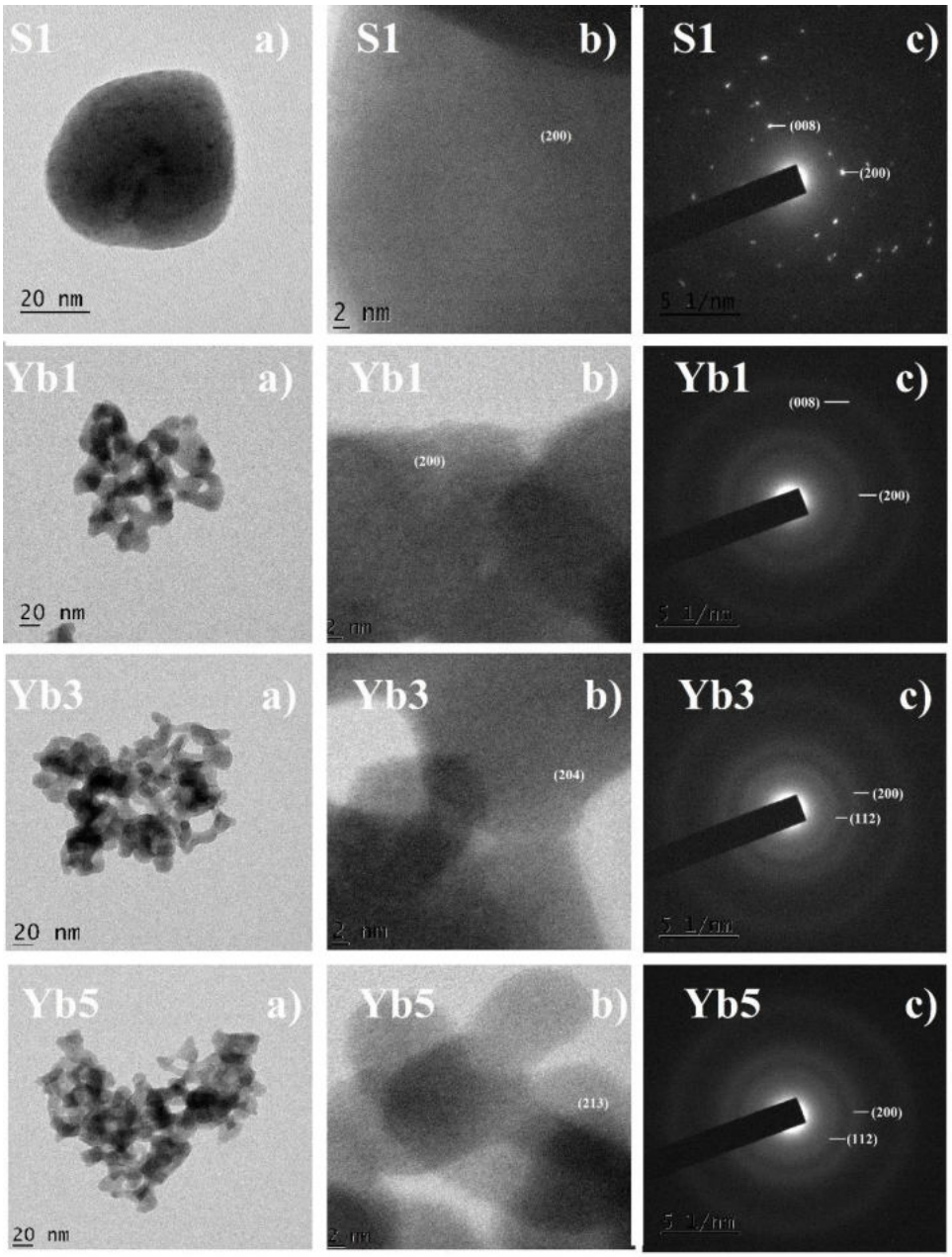

Figure 5.6 a) TEM bright field images b) HRTEM images and c) SAED patterns of pristine and Yb doped $BaWO_4$ samples

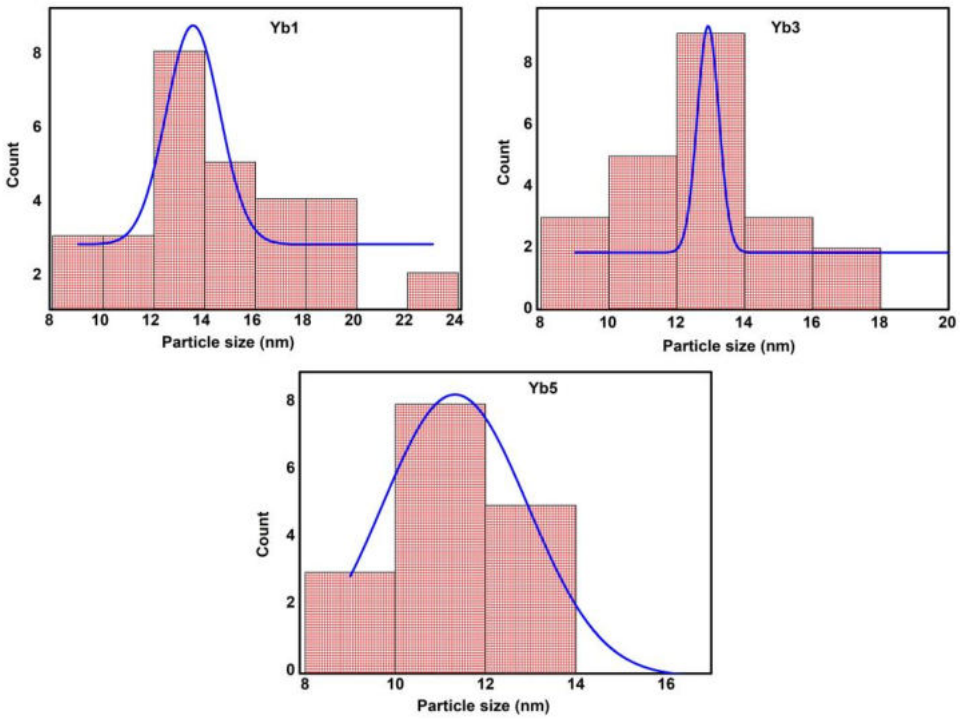

Figure 5.7 Particle size distribution of Yb doped $BaWO_4$ samples

5.3.1.4 FTIR Analysis

The FTIR spectra of the pristine and Yb doped $BaWO_4$ samples in the transmitted mode are recorded at room temperature to confirm the phase formation and purity of the samples. In Figure 5.8, a strong transmittance peak centred around 820 cm^{-1} is obtained for all the samples. The peak corresponds to the antisymmetric stretching vibration $F_2(v3)$, which is originating from the W-O in the WO_4^{2-} tetrahedron [20]. FTIR spectra of all the samples are almost the same indicating that Yb doping has no effect on the transmittance in the measured region. Like powder XRD studies, FTIR analysis also confirms the absence of any secondary phases or any variation in the tetragonal structure of the lattice due to the incorporation of Yb^{3+} ions [21].

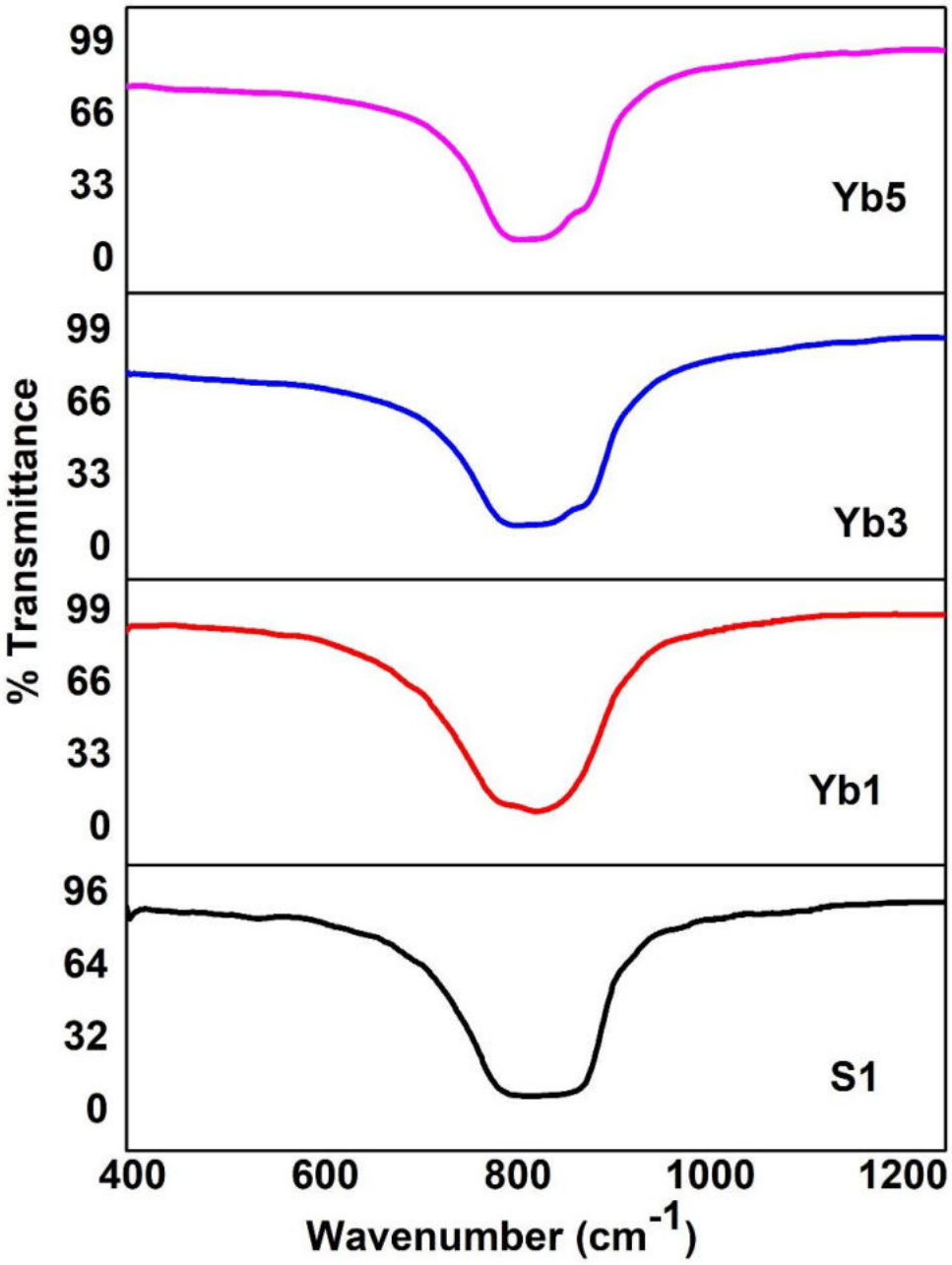

Figure 5.8 FTIR spectra of pristine and Yb doped $BaWO_4$ samples

5.3.1.5 Raman Analysis

Raman spectra of the pristine and Yb doped $BaWO_4$ samples recorded in the spectral range 0 to 1200 cm^{-1} to verify the rotational, vibrational, and other low-frequency modes of the system are depicted in Figure 5.9. Details of the various Raman modes of the tetragonal scheelite $BaWO_4$ are discussed in *Section 3.3.2.5.*

As can be seen from Table 5.5, all the Raman modes observed for the pristine and Yb doped $BaWO_4$ samples are characteristics of a tetragonal structure in agreement with the literature values available for $BaWO_4$ [22–24]. The small differences obtained for the Raman active modes are due to the variations in synthesis routes, average crystallite size, and the structural deviations in the lattice caused by the doping [25]. The bending vibrations $v_2(B_g)$, $v_4(B_g)$ and $v_4(E_g)$ merged to $v_2(A_g)$, and cannot be distinguished in the doped samples. In the doped samples, the bending mode $v_2(A_g)$ is shifted toward the lower wavenumber side indicating a change in the W-O coordination. All the stretching modes $v_1(A_g)$, $v_3(B_g)$, and $v_3(E_g)$ are also shifted towards the lower wavenumber side. Hence the W-O bond length increases or it experiences a tensile strain due to the substitution of Yb^{3+} ions into the $BaWO_4$ lattice [26,27]. There is also a shift in the external modes which confirms the substitution of Ba^{2+} cation by the Yb^{3+} ion in the lattice [28]. The A_g rotational mode is shifted towards the high-frequency side (low wavenumber side), and the Raman mode is found to decrease, due to the introduction of smaller ionic radius Yb^{3+} ions into the $BaWO_4$ lattice [28,29]. In short, Raman spectra studies also confirmed that the pristine and Yb doped $BaWO_4$ samples formed are of scheelite tetragonal structure.

Table 5.5 Comparison of Raman active modes of the pristine and Yb doped $BaWO_4$ samples with theoretical values

Peak/ mode	Value of ω in cm^{-1}				
	Theoretical [22]	Present values of the $BaWO_4$ samples			
		S1	**Yb1**	**Yb3**	**Yb5**
$T(B_g)$	55	-	-	-	-
$T(E_g)$	81	75.05	68.81	71.41	69.07
$T(E_g)$	110	102.06	95.30	96.86	96.08
$T(B_g)$	145	132.44	130.88	129.32	129.58
$R(A_g)$	149	150.09	144.90	145.68	144.91
$R(E_g)$	209	191.13	186.71	186.71	186.71
$\nu_2(A_g)$	328	332.14	328.50	328.5	327.72
$\nu_2(B_g)$	329	332.65	-	-	-
$\nu_4((B_g)$	339	345.38	-	-	-
$\nu_4(E_g)$	348	354.20	-	-	-
$\nu_3(E_g)$	797	795.41	792.55	791.77	791.78
$\nu_3(B_g)$	823	832.03	828.39	828.39	827.35
$\nu_1(A_g)$	928	928.11	923.69	923.69	924.22

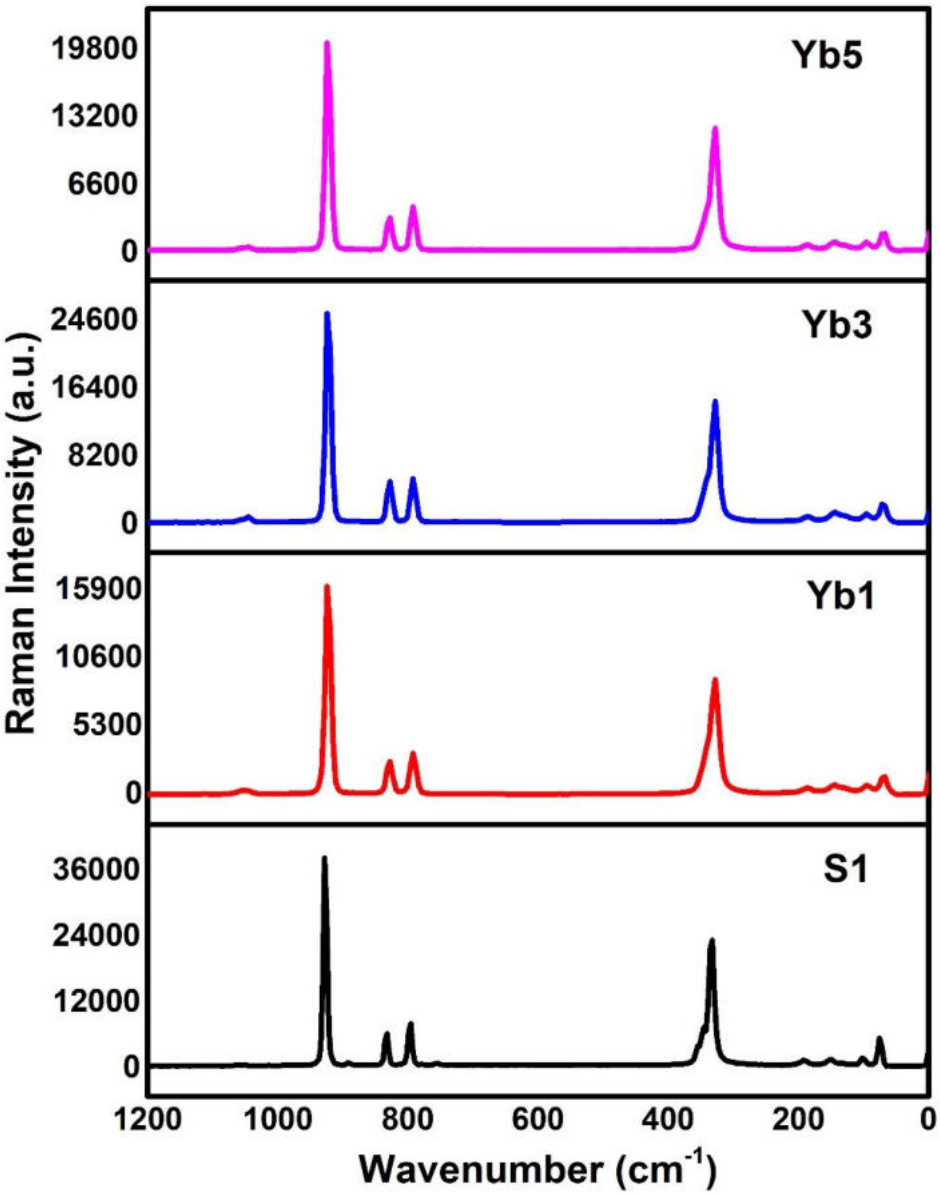

Figure 5.9 Raman spectra of pristine and Yb doped $BaWO_4$ samples

5.3.2 Optical Properties

UV-visible absorption and photoluminescence studies of the Yb doped $BaWO_4$ samples are described here. The analyses are carried out as described in *Section 2.5*.

5.3.2.1 UV-visible Analysis

Diffuse reflectance spectra of the pristine and Yb doped $BaWO_4$ powder samples are taken to study the optical absorption properties of the sample. The optical absorption coefficient is obtained from the diffuse reflectance spectra by Kubelka-Munk transformation equation. The absorbance spectra of the pristine and Yb doped $BaWO_4$ samples are shown in Figure 5.10. All the samples show absorption in the ultraviolet region with a maximum at 220.39 nm for the pristine sample and a maximum at 220.74 nm for the doped samples corresponding to the ligand to metal charge transfer transition inside the WO_4^{2-} anion [30]. By absorbing the ultraviolet radiation, the excitation from O_{2p} to W_{t2g} in the $(WO_4)^{2-}$ group takes place. Because of the strong interactions between the hole on the oxygen and the electron on the tungsten, they remain together as an exciton in the excited state [30]. The absorption cross-section of the Yb doped $BaWO_4$ samples are found to increase with an increase in the amount of Yb in the sample. A slight red shift in the absorption peak is observed for the Yb doped $BaWO_4$ samples.

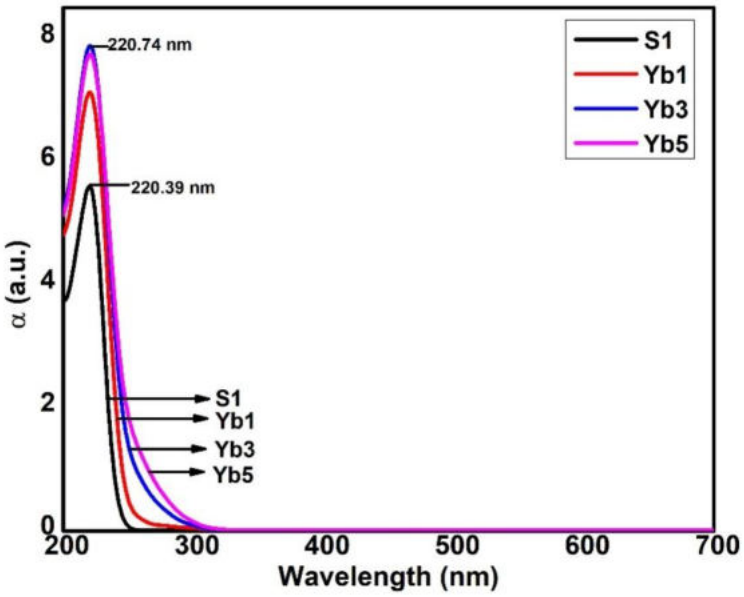

Figure 5.10 Optical absorption spectra of pristine and Yb doped $BaWO_4$ samples

The optical bandgap of the pristine and Yb doped $BaWO_4$ samples is calculated from the optical absorption using the Tauc relation [31]. Figure 5.11 shows the plot of $(\alpha h\upsilon)^2$ versus $h\upsilon$ for the $BaWO_4$ samples. The optical bandgap values obtained for the samples **S1**, **Yb1**, **Yb3** and **Yb5** are 5.26, 5.22, 5.20 and 5.16 eV, respectively. The results confirm a decrease in bandgap with an increase in the quantity of Yb. The reason may be that the Pauling electronegativity of ytterbium (1.1) is closer to tungsten (2.36) than barium (0.89). As a result, Yb ions in the lattice can influence the energy levels of W atoms in the WO_4 tetrahedral structure than Ba, and hence the bandgap decreases [32]. It can be concluded that the introduction of Yb in the sample creates an energy level or band in between the valence and conduction band of the $BaWO_4$ sample (intermediate levels). Literature reports that barium has no significant effect on

the optical bandgap of the $BaWO_4$ sample [33]. They only possess a single ligand to metal charge transfer band in the region 218 − 274 nm, with a band maximum occurring at 220 −250 nm. The exact location of this maximum depends on the extend of distortion of the WO_4 tetragonal structure [34].

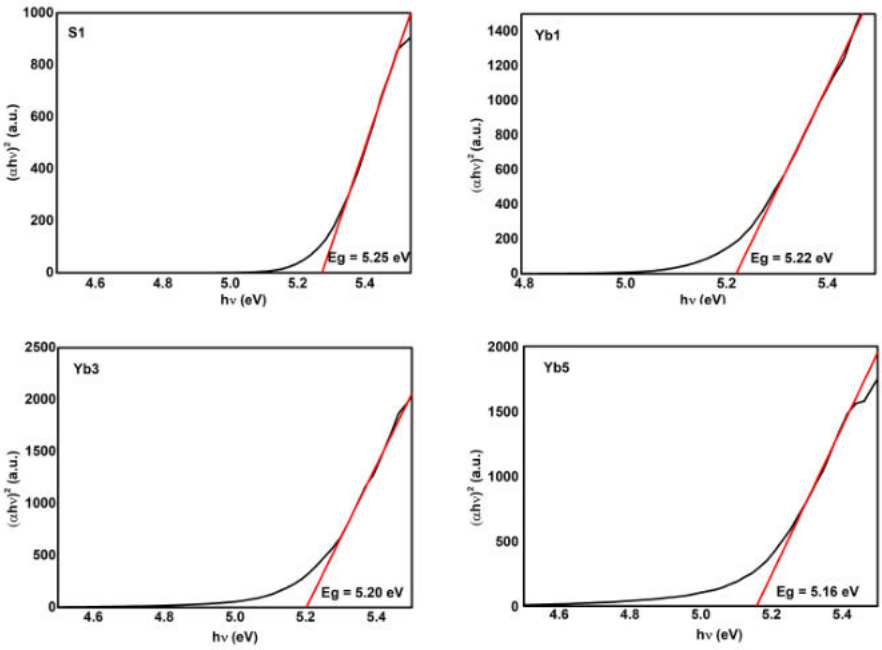

Figure 5.11 Tauc plots of pristine and Yb doped $BaWO_4$ samples

5.3.2.2 Photoluminescence Studies

The photoluminescence emission properties of the Yb doped $BaWO_4$ samples are investigated by PL measurements in the NIR range. The emission spectra of the Yb doped $BaWO_4$ samples excited by 275 nm are shown in Figure 5.12. The NIR emission spectra of the Yb doped $BaWO_4$ samples are assigned to the $^2F_{5/2} \rightarrow {}^2F_{7/2}$ transition of the Yb^{3+} ion [35]. The emission is not a single sharp line, but it is an envelope of lines ranging from 900 to 1090 nm. There are many reasons for the broadening of the emission spectrum; one of them is the stark

splitting, the splitting of Yb^{3+} energy levels due to crystal field effects. In a crystal field of D_{2d} or lower symmetry, stark splitting occurs. The excited state $^2F_{5/2}$ of Yb^{3+} ion is split into three components, and the ground state $^2F_{7/2}$ is split into four components [36], as shown in Figure 5.13. The NIR emission of the Yb doped $BaWO_4$ nanoparticles can find suitable potential applications such as optical fiber communication, lasers, efficient solar cells, bioanalyses, and bioimaging [37].

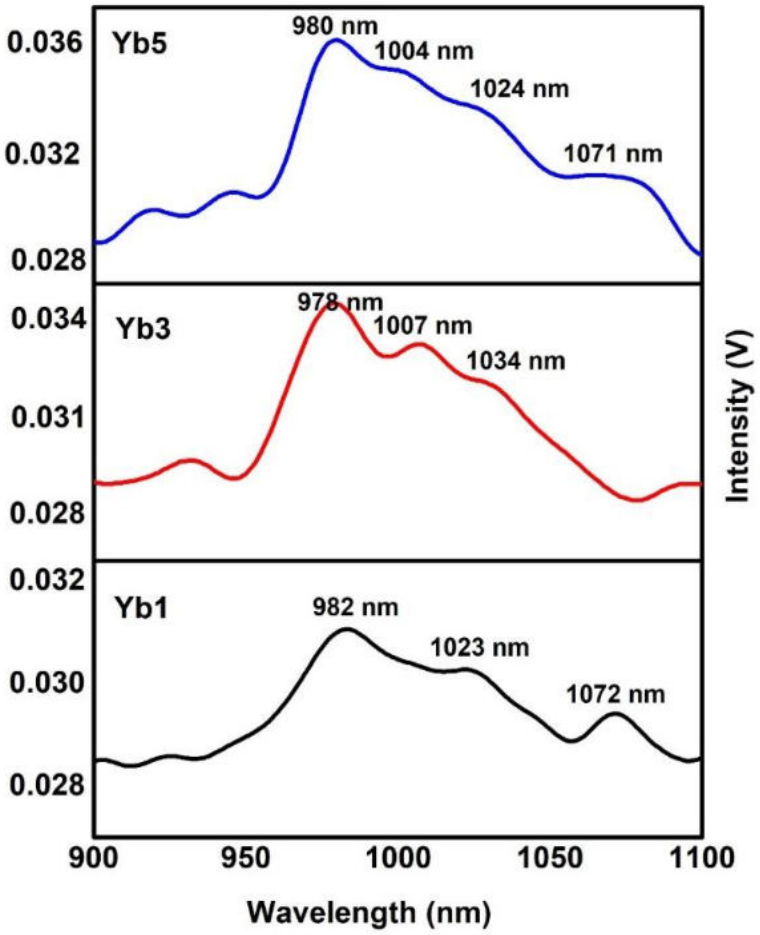

Figure 5.12 NIR PL emission spectra of the Yb doped $BaWO_4$ samples

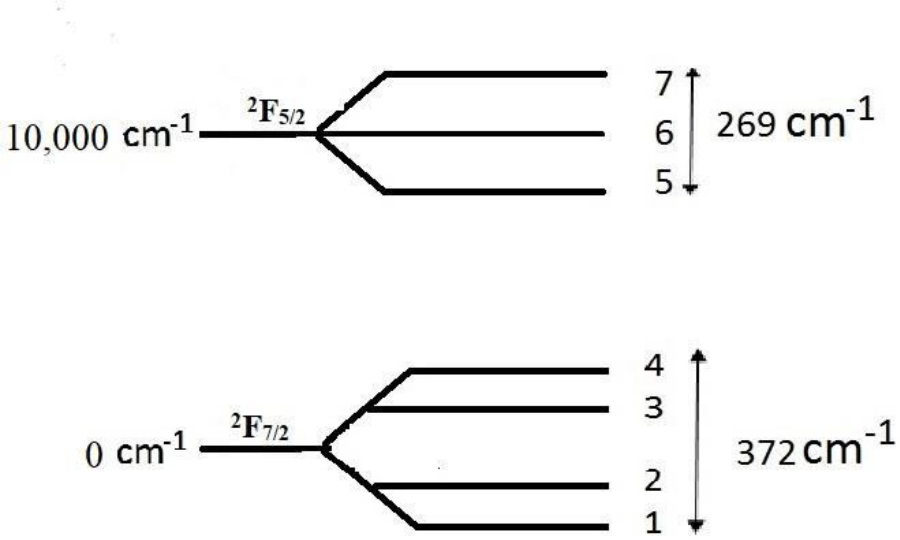

Figure 5.13 Stark splitting of Yb^{3+} ions

Laporte's parity selection rule implies that the electron dipole transition between the $^2F_{5/2}$ and $^2F_{7/2}$ states of Yb^{3+} is forbidden and the magnetic dipole transitions should play an important role in the de-excitation of the $^2F_{5/2}$ state. However, it is partially allowed when the dopant Yb^{3+} ion undergoes the influence of a ligand field; non-centrosymmetric interactions mix electronic states of opposite parity (even parity) into 4f states. The mixing of the $4f^{13}$ configuration with the opposite parity $4f^{12}5d^1$ configuration, the ligand to metal charge transfer states, and the vibrational levels will contribute to the intensity of these induced transitions [6,38]. The positions of the peaks provide information on the barycenter of the $^2F_{5/2}$ excited state multiplet and the $^2F_{7/2}$ ground state multiplet. The peaks width is determined by the crystal field splitting of the multiplets and the coupling strength of the 5d electrons [39]. Since the 5d orbitals are less effectively shielded than the 4f ones, their energy depends on the crystal

environment, and hence it may vary from one compound to another [12]. The peaks around 980, 1005, 1024 and 1071 nm correspond to the transitions 5 →1, 5→2, 5→3 and 5→4 respectively. It can be seen that the emission intensity of the samples increases with the amount of Yb in the sample. A slight change in the output is observed for sample **Yb3**, which has minimum crystallite size and crystallite volume. A schematic representation of the Yb^{3+} luminescence in the Yb doped $BaWO_4$ samples is shown in Figure 5.14. In short, the results of PL emission of the Yb doped $BaWO_4$ samples confirm emission spectra in the NIR range, which proposes its use in potential applications.

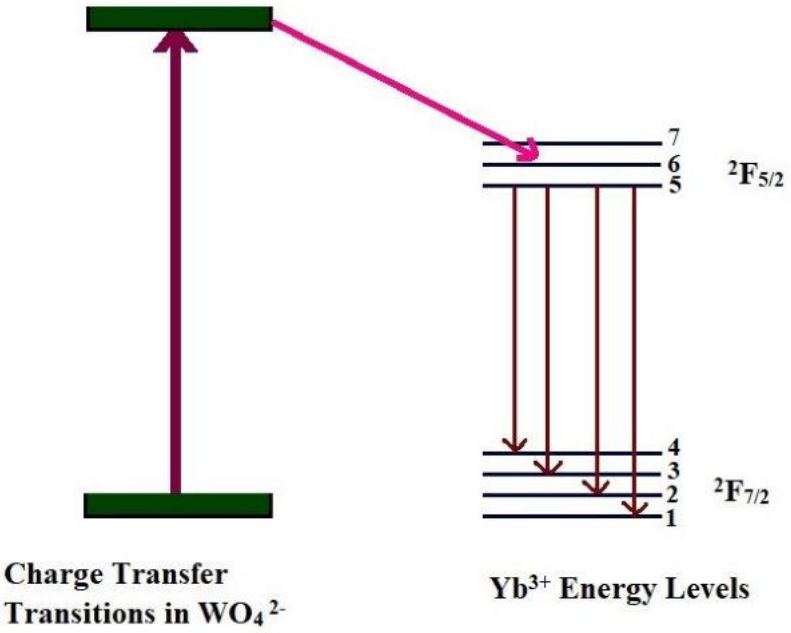

Figure 5.14 Schematic representation of Yb^{3+} luminescence in Yb doped $BaWO_4$ samples

5.3.3 Magnetic studies

The magnetic behaviour of the pristine and Yb doped $BaWO_4$ samples is investigated by the VSM technique with an externally applied magnetic field varying between -15 and +15 kOe. Figure 5.15 displays the hysteresis loop (magnetization against field) of the samples at room temperature. The magnetic properties of the sample firmly depend on the synthesis route, calcination temperature, morphology, particle size, and the substitution of metal ions in the crystal lattice. The saturation magnetization, coercivity, retentivity, and squareness ratio R of the pristine and Yb doped $BaWO_4$ samples are directly obtained from the hysteresis loop. The magnetocrystalline anisotropy constant and the magnetic moment in the Bohr magneton of the pristine and Yb doped $BaWO_4$ samples are calculated as explained in *Section 4.3.3*.

The saturation magnetization, coercivity, retentivity, squareness ratio R, anisotropy constant, and magnetic moment of the Yb doped $BaWO_4$ samples varies in an irregular manner with the increase of Yb content as evident from the comparison Table 5.6. Interestingly, all the magnetic parameters show a maximum value for the sample **Yb3**. As the squareness ratio of the pristine and Yb doped $BaWO_4$ samples are less than 0.5, these particles are single-domain magnetic particles [40].

Table 5.6 Comparison of magnetic properties of pristine and Yb doped $BaWO_4$ samples

Sample	Saturation magnetization (Ms) (emu/gm)	Coercivity Oe	Retentivity (Mr) (emu/gm)	Squareness ratio R=Mr/Ms	Anisotropy constant (ergs/Oe)	Magnetic moment (Bohr Magneton)
S1	25.776×10^{-3}	52.583	0.539×10^{-3}	0.02109	1.41185	1.777×10^{-3}
Yb1	27.081×10^{-3}	21.164	0.273×10^{-3}	0.01775	0.59702	1.869×10^{-3}
Yb3	32.600×10^{-3}	37.232	0.652×10^{-3}	0.04844	1.2643	2.254×10^{-3}
Yb5	27.072×10^{-3}	-10.923	0.147×10^{-3}	0.00901	0.3080	1.876×10^{-3}

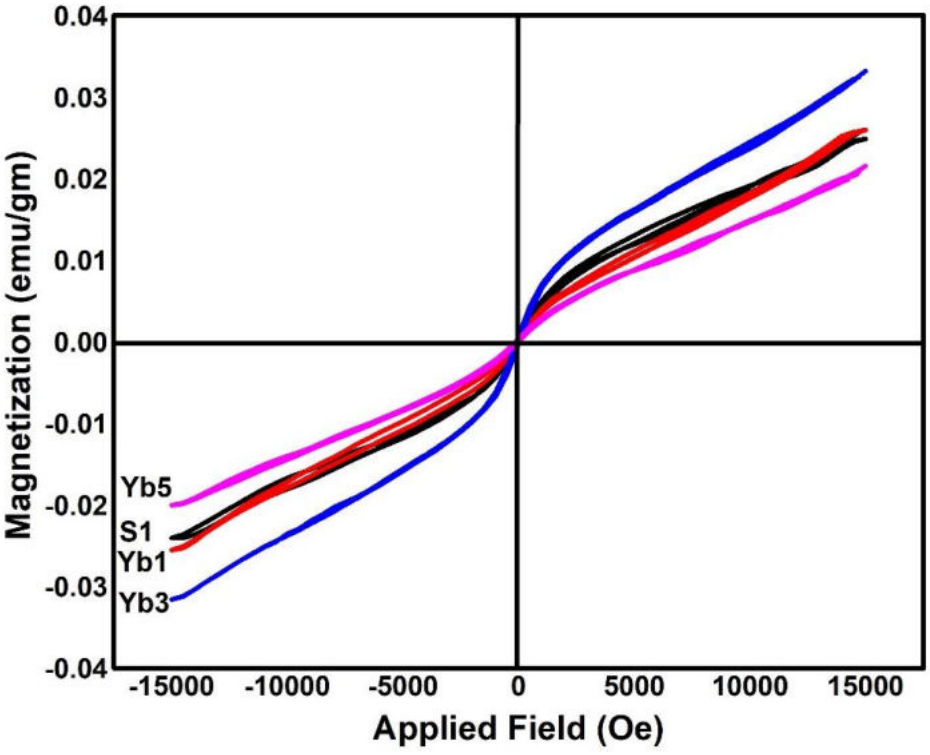

Figure 5.15 M-H loops of pristine and Yb doped $BaWO_4$ samples

As seen from Figure 5.15, the samples **S1** and **Yb1** exhibit weak ferromagnetic behaviour mixed with paramagnetic nature. However, the sample **Yb3** shows a ferromagnetic behaviour at lower applied magnetic fields. As the applied magnetic field is increased, saturation magnetization disappears completely and exhibits antiferromagnetic nature, and the magnetization increases with the increase in the applied field. This suggests that the ferromagnetic behaviour at the lower applied field is due to double exchange interaction and superexchange interaction [41]. The sample **Yb5** does not exhibit hysteresis showing superparamagnetic nature. In short, the magnetic properties of the Yb doped $BaWO_4$ nanoparticles strongly depend on the concentration of the Yb ions.

5.4 Conclusion

- A systematic study is conducted on the effect of Yb doping on the structural, optical, and magnetic properties of nanocrystalline $BaWO_4$ samples synthesized by the chemical precipitation route.
- The results of structural studies indicated a pure scheelite-type tetragonal phase with space group $I4_1/a$ (88) and point group symmetry C_{4h}^6 for the pristine and Yb doped $BaWO_4$ nanoparticles.
- TEM images confirmed the reduction in particle sizes of $BaWO_4$ nanoparticles due to the substitution of Yb^{3+} ions.
- Enhanced UV absorption and reduction in optical bandgap is observed on Yb doping.
- NIR luminescence emission is observed for the Yb doped $BaWO_4$ samples and the intensity of emission increases as the quantity of Yb in the sample increases. It confirms the interaction of the $BaWO_4$ lattice with the Yb^{3+}

ions and the energy transfer between the tungstate group and the Yb^{3+} ions. This property of the Yb doped $BaWO_4$ nanomaterial can be used in optical fiber communication, highly efficient solar cells, bioanalysis and imaging.

- The weak ferromagnetic nature of the pristine $BaWO_4$ sample changes with the increase of doping concentration of Yb^{3+} ions. The doped sample **Yb5** shows superparamagnetic behaviour. The VSM studies confirm that the magnetic parameters of $BaWO_4$ nanoparticles strongly depend on the concentration of Yb^{3+} ions.

References

[1] Y. Su, L. Li, G. Li, Self-assembly and multicolor emission of core/shell structured $CaWO_4:Na^+/Ln^{3+}$ spheres, Chem. Commun. (2008) 4004–4006.

[2] J. Liao, B. Qiu, H.R. Wen, Y. Li, R. Hong, H. You, Luminescence properties of monodispersed spherical $BaWO_4:Eu^{3+}$ microphosphors for white light-emitting diodes, J. Mater. Sci. 46 (2011) 1184–1189.

[3] Z.H. Ju, R.P. Wei, J.X. Ma, C.R. Pang, W.S. Liu, A novel orange emissive phosphor $SrWO_4:Sm^{3+}$ for white light-emitting diodes, J. Alloys Compd. 507 (2010) 133–136.

[4] I.M. Pinatti, P.F.S. Pereira, M. de Assis, E. Longo, I.L.V. Rosa, Rare earth doped silver tungstate for photoluminescent applications, J. Alloys Compd. 771 (2019) 433–447.

[5] G. Boulon, Why so deep research on Yb^{3+}-doped optical inorganic materials?, J. Alloys Compd. 451 (2008) 1–11.

[6] A. Kaminska, A. Duzynska, A. Suchocki, M. Bettinelli, Spectroscopy of f–f radiative transitions of Yb^{3+} ions in ytterbium doped orthophosphates at ambient and high hydrostatic pressures, J. Phys. Condens. Matter. 22 (2010) 225902, 1-8.

[7] M. Ferhi, K. Horchani-Naifer, S. Hraiech, M. Ferid, Y. Guyot, G. Boulon, Near infrared and charge transfer luminescence of Yb^{3+}-doped $LaPO_4$ at room temperature, Radiat. Meas. 46 (2011) 1033–1037.

[8] C.G. Dou, Q.H. Yang, X.M. Hu, J. Xu, Cooperative up-conversion luminescence of ytterbium doped yttrium lanthanum oxide transparent ceramic, Opt. Commun. 281 (2008) 692–695.

[9] S. Heer, K. Kömpe, H.U. Güdel, M. Haase, Highly efficient multicolour upconversion emission in transparent colloids of lanthanide-doped $NaYF_4$ nanocrystals, Adv. Mater. 16 (2004) 2102–2105.

[10] F. Wang, X. Liu, Upconversion multicolor fine-tuning: visible to near-infrared emission from lanthanide-doped $NaYF_4$ nanoparticles, J. Am. Chem. Soc. 130 (2008) 5642–5643.

[11] B.M. Van Der Ende, L. Aarts, A. Meijerink, Near-infrared quantum cutting for photovoltaics, Adv. Mater. 21 (2009) 3073–3077.

[12] M. Ramirez, L. Bausa, S.W. Biernacki, A. Kaminska, A. Suchocki, M. Grinberg, Influence of hydrostatic pressure on radiative transition probability of the intrashell 4f transitions in Yb^{3+} ions in lithium niobate crystals, Phys. Rev. B - Condens. Matter Mater. Phys. 72 (2005) 1–5.

[13] R.K. Tamrakar, N. Tiwari, V. Dubey, K. Upadhyay, Infrared spectroscopy and luminescence spectra of Yb^{3+} doped ZrO_2 nanophosphor , J. Radiat. Res. Appl. Sci. 8 (2015) 399–403.

[14] L. Van Pieterson, M. Heeroma, E. De Heer, A. Meijerink, Charge transfer luminescence of Yb^{3+}, J. Lumin. 91 (2000) 177–193.

[15] O.M. Ten Kate, H.T. Hintzen, P. Dorenbos, E. Van Der Kolk, Yb^{3+} doped $LaSi_3N_5$ and YSi_3N_5 with low energy charge transfer for near-infrared light-emitting diode and solar cell application, J. Mater. Chem. 21 (2011) 18289–18294.

[16] G. Zhang, C. Liu, J. Wang, X. Kuang, Q. Su, An intense charge transfer broadband sensitized phosphor suitable for solar spectral convertor, Opt. Express. 19 (2011) 24314–24319.

[17] P. Jena, S.K. Gupta, N.K. Verma, A.K. Singh, R.M. Kadam, Energy transfer dynamics and time resolved photoluminescence in $BaWO_4:Eu^{3+}$ nanophosphors synthesized by mechanical activation, New J. Chem. 41 (2017) 8947–8958.

[18] A. Boukerika, L. Guerbous, Annealing effects on structural and luminescence properties of red Eu^{3+}-doped Y_2O_3 nanophosphors prepared by sol-gel method, J. Lumin. 145 (2014) 148–153.

[19] M.K. Devaraju, S. Yin, T. Sato, Solvothermal synthesis, controlled morphology and optical properties of $Y_2O_3:Eu^{3+}$ nanocrystals, J. Cryst. Growth. 311 (2009) 580–584.

[20] S. Vidya, S. Solomon, J.K. Thomas, Synthesis, characterization, and low

temperature sintering of nanostructured $BaWO_4$ for optical and LTCC applications, Adv. Condens. Matter Phys. 2013 (2013) 1–11.

[21] B. Samanta, A.K. Dey, P. Bhaumik, S. Manna, A. Halder, D. Jana, K.K. Chattopadhyay, U.K. Ghorai, Controllable white light generation from novel $BaWO_4$: $Yb^{3+}/Ho^{3+}/Tm^{3+}$ nanophosphor by modulating sensitizer ion concentration, J. Mater. Sci. Mater. Electron. 30 (2019) 1068–1075.

[22] A. Phuruangrat, T. Thongtem, S. Thongtem, Cyclic microwave-assisted synthesis and characterization of nano-crystalline alkaline earth metal tungstates, J. Ceram. Soc. Japan. 116 (2008) 605–609.

[23] F.J. Manjón, D. Errandonea, N. Garro, J. Pellicer-Porres, P. Rodríguez-Hernández, S. Radescu, J. López-Solano, A. Mujica, A. Muñoz, Lattice dynamics study of scheelite tungstates under high pressure I. $BaWO_4$, Phys. Rev. B - Condens. Matter Mater. Phys. 74 (2006) 1–17.

[24] T.T. Basiev, A.A. Sobol, Y.K. Voronko, P.G. Zverev, Spontaneous Raman spectroscopy of tungstate and molybdate crystals for Raman lasers, Opt. Mater. (Amst). 15 (2000) 205–216.

[25] S.P.S. Porto, J.F. Scott, Raman spectra of $CaWO_4$, $SrWO_4$, $CaMoO_4$, and $SrMoO_4$, Phys. Rev. 157 (1967) 716–719.

[26] D. Rangappa, T. Fujiwara, M. Yoshimura, Synthesis of highly crystallized $BaWO_4$ film by chemical reaction method at room temperature, Solid State Sci. 8 (2006) 1074–1078.

[27] S. Liang, M.N. Hasan, J.H. Seo, Direct observation of raman spectra in black phosphorus under uniaxial strain conditions, Nanomaterials. 9 (2019) 1–8.

[28] A. Jayaraman, B. Batlogg, L.G. Vanuitert, High-pressure Raman study of alkaline-earth tungstates and a new pressure-induced phase transition in $BaWO_4$, Phys. Rev. B. 28 (1983) 4774–4777.

[29] P. Tarte, M. Liegeois-Duyckaerts, Vibrational studies of molybdates, tungstates and related compounds-I. New infrared data and assignments for the scheelite-type compounds $XIIMoO_4$ and $XIIWO_4$, Spectrochim. Acta Part A Mol. Spectrosc. 28 (1972) 2029–2036.

[30] S.M.M. Zawawi, R. Yahya, A. Hassan, H.N.M.E. Mahmud, M.N. Daud, Structural and optical characterization of metal tungstates (MWO_4; M=Ni, Ba, Bi) synthesized by a sucrose-templated method, Chem. Cent. J. 7 (2013) 1–10.

[31] D.L. Wood, J. Tauc, Weak absorption tails in amorphous semiconductors, Phys. Rev. B. 5 (1972) 3144–3151.

[32] M. Tyagi, S.G. Singh, A.K. Chauhan, S.C. Gadkari, First principles calculation of optical properties of $BaWO_4$: A study by full potential method, Phys. B Condens. Matter. 405 (2010) 4530–4535.

[33] W.M. Yen', S. Shionoya, H. Yamamoto, eds., Fundamentals of Phosphors, CRC Press, Taylor and Francis Group, 2007.

[34] E.I. Ross-Medgaarden, I.E. Wachs, Structural determination of bulk and surface tungsten oxides with UV-vis diffuse reflectance spectroscopy and raman spectroscopy, J. Phys. Chem. C. 111 (2007) 15089–15099.

[35] S. Hou, Y. Xing, H. Ding, X. Liu, B. Liu, X. Sun, Facile synthesis and photoluminescence properties of dumbbell-like Ln-doped $BaWO_4$ (Ln =

Nd, Er, Yb) microstructures, Mater. Lett. 64 (2010) 1503–1505.

[36] V.A. Volkovich, A.B. Ivanov, S.M. Yakimov, D. V. Tsarevskii, O.A. Golovanova, V. V. Sukhikh, T.R. Griffiths, Electronic absorption spectra of rare earth (III) species in NaCl-2CsCl eutectic based melts, AIP Conf. Proc. 1767 (2016) 020023.

[37] J.C.G. Bünzli, S. V. Eliseeva, Lanthanide NIR luminescence for telecommunications, bioanalyses and solar energy conversion, J. Rare Earths. 28 (2010) 824–842.

[38] J.C.G. Bünzli, S. V. Eliseeva, Intriguing aspects of lanthanide luminescence, Chem. Sci. 4 (2013) 1939–1949.

[39] P. Dorenbos, The 4fn↔4fn-1 5d transitions of the trivalent lanthanides in halogenides and chalcogenides, J. Lumin. 91 (2000) 91–106.

[40] Y. Slimani, H. Güngüneş, M. Nawaz, A. Manikandan, H.S. El Sayed, M.A. Almessiere, H. Sözeri, S.E. Shirsath, I. Ercan, A. Baykal, Magneto-optical and microstructural properties of spinel cubic copper ferrites with Li-Al co-substitution, Ceram. Int. 44 (2018) 14242–14250.

[41] D. Chakraborty, K. Shaik, Effect of doping concentration, temperature and magnetic field on magnetic properties of Mn doped ITO nanoparticles and thin films, J. Magn. Magn. Mater. 486 (2019) 165268.

Chapter 6

EFFECT OF 8 MeV ELECTRON BEAM IRRADIATION ON THE PROPERTIES OF NANOCRYSTALLINE $BaWO_4$

The dose dependent effect of 8 MeV electron beam irradiation on the structural and optical properties of the nanocrystalline $BaWO_4$ synthesized by the chemical precipitation method is discussed in this chapter.

6.1 Introduction

In recent years, the electron irradiation effects of nanoparticles became an important area of research because electron beam (EB) irradiation can be used to modify the structural and optical properties of nanoparticles. Electron beam irradiation results in small intrinsic defects in the material, re-growth, and crystallization of the materials. Hence, changes occur in material properties due to electron irradiation [1–7], which can be used for varied applications. The present chapter deals with the dose dependent effect of 8 MeV electron beam irradiation on the structural and optical properties of $BaWO_4$ nanoparticles fabricated by the chemical precipitation route.

6.2 Preparation of the Sample

The $BaWO_4$ powder samples calcined at 400 ºC are taken as the sample for electron beam irradiation study. The synthesis of the sample is described in *Section 3.2*. The powder samples taken in polythene covers are exposed to high energy electron beam (8 MeV) irradiation at a dose of 0, 2, 4, and 6 kGy and a dose rate of 300 Gy per minute in the presence of air, as described in *Section 2.8*. The dose and dose rate are calibrated to a current integrator using chemical dosimeters. The dose is uniform over an area of 8×8 cm^2, as determined from dosimetry. Temperature is maintained around 24 ºC using an air handling unit with an air exchanger. No rise in temperature inside the machine room and sample holder. $BaWO_4$ powder samples irradiated with a dose of 0, 2, 4, and 6 kGy are designated as **S1**, **R2**, **R4,** and **R6** respectively.

6.3 Results and Discussion

6.3.1 Structural Characterization

The structural characterization of the EB irradiated $BaWO_4$ samples are carried out by XRD, SEM, FTIR, and Raman analyses following the procedure described in *Section 2.4*. The data for sample **S1** is taken from Chapter 3.

6.3.1.1 Powder XRD Analysis

The structural characteristics of the electron beam irradiated barium tungstate nanoparticles are studied by using X-ray powder diffraction. Figure 6.1 shows the XRD patterns of the pristine and EB irradiated $BaWO_4$ powder samples. All diffraction peaks can be indexed with the body-centred scheelite tetragonal structure of $BaWO_4$ with a space group $I4_1/a$, which is consistent with the JCPDS Card no. 72-0746. The well defined sharp diffraction peaks indicate

the purity and crystallinity of the samples. The average crystallite sizes of the $BaWO_4$ samples are estimated using the Scherrer equation. The crystallite size and micro-strain of the pristine and EB irradiated samples are also estimated by Williamson-Hall analysis (Figure 6.2).

Lattice parameters of the samples are calculated using the plane spacing equation for tetragonal structure (space group $I4_1/a$) from XRD data. The lattice parameters and crystallite size of the pristine and electron beam irradiated $BaWO_4$ samples are presented in Table 6.1. The table shows the changes in lattice parameters ***a*** and ***c*** with the increase in EB irradiation dose.

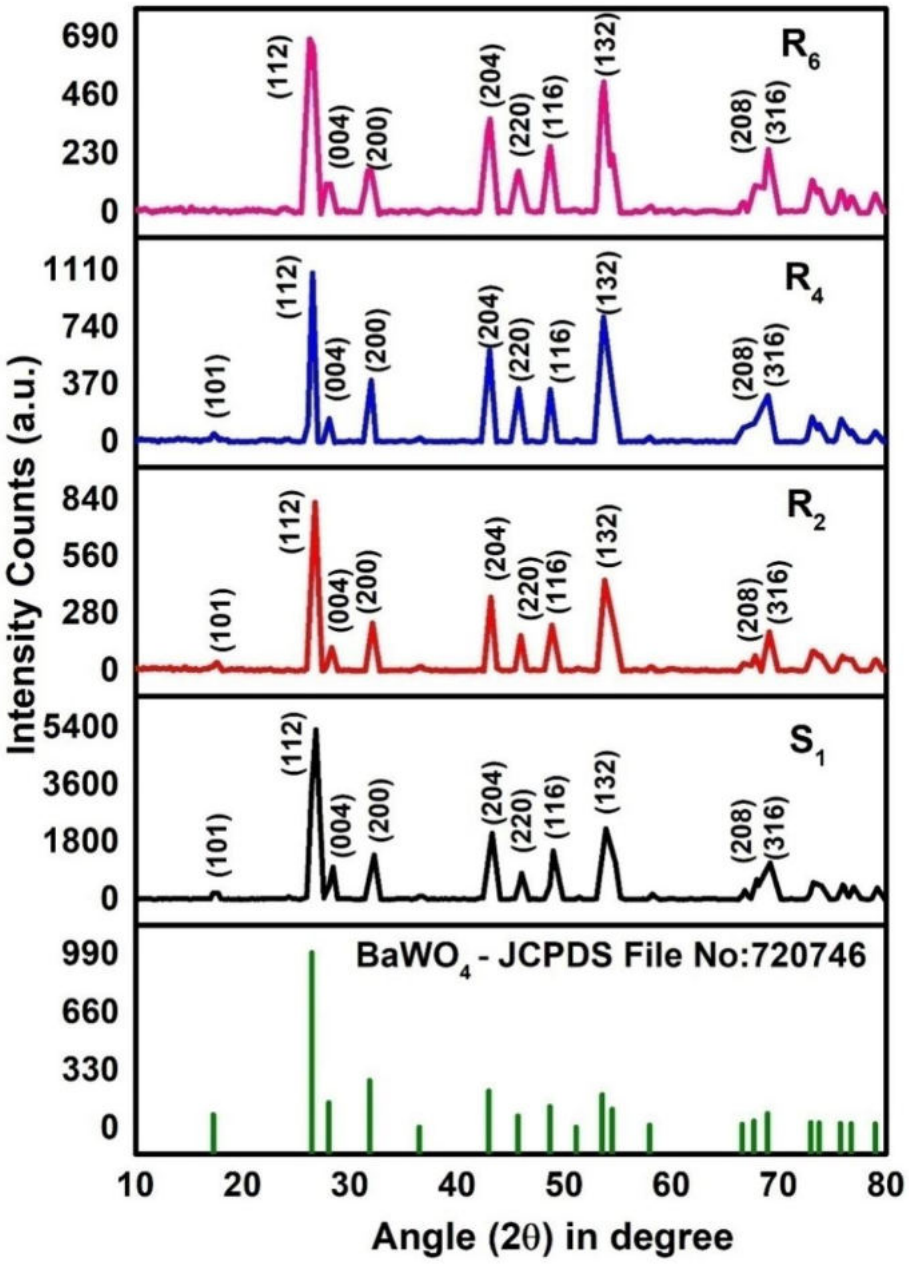

Figure 6.1 XRD patterns of pristine and EB irradiated $BaWO_4$ samples

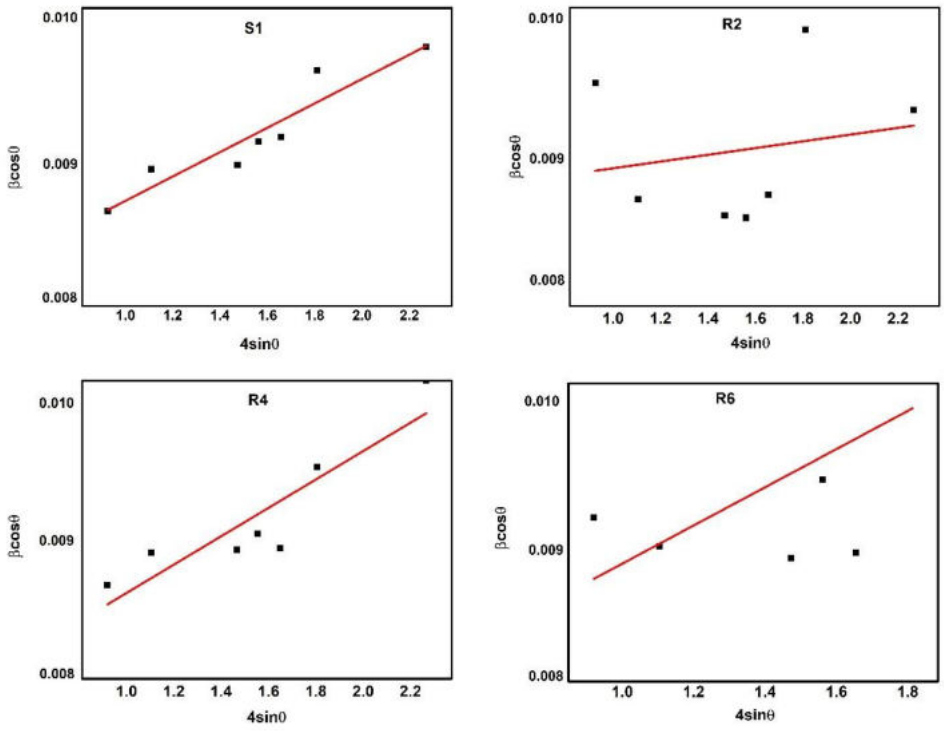

Figure 6.2 Williamson-Hall plots of pristine and EB irradiated $BaWO_4$ samples

Rietveld refinement of the samples is also performed to investigate the effect of electron beam irradiation on the structural parameters of the $BaWO_4$ lattice. Double Voigt is used for peak profile fitting. All the refinement results indicated that the samples displayed a pure scheelite-type tetragonal phase with space group $I4_1/a$ (88) and point group symmetry C_{4h}^6. Refined parameters of the pristine and EB irradiated $BaWO_4$ samples are shown in Table 6.2. The refinement output is displayed in Figure 6.3.

Table 6.1 Lattice parameters and crystallite size of pristine and EB irradiated $BaWO_4$ samples

Sample	a = b (Å)	c (Å)	Unit cell volume ($Å^3$)	Crystallite size (nm)		Micro-strain $\times 10^{-3}$
				Scherrer method	W-H method	
S1	5.589	12.66	395.45	13.15	14.56	0.149
R2	5.594	12.61	394.66	11.90	12.23	0.106
R4	5.603	12.69	398.63	12.02	13.82	0.213
R6	5.607	12.64	397.52	9.14	11.58	0.206

A slight variation in crystallite size is observed due to electron beam irradiation. A slight peak shift towards the lower angle side with an increase in dose is also observed for all the major peaks in the XRD patterns. The stretching or compressing of bonds between atoms due to the residual stress generates a strain in the crystalline materials. Hence, 'd' spacing of crystallographic planes as well as the Bragg angles could modify due to the EB irradiation effect [8]. Since almost all the major peaks shifted towards the lower angle side, tensile stress is developed in the sample [8], and it increases with the dose. However, some other peaks are shifted towards the higher angle side showing a compressive strain in that plane [9]. Interestingly, the EB irradiation offers some defects in the crystal lattice upon EB irradiation.

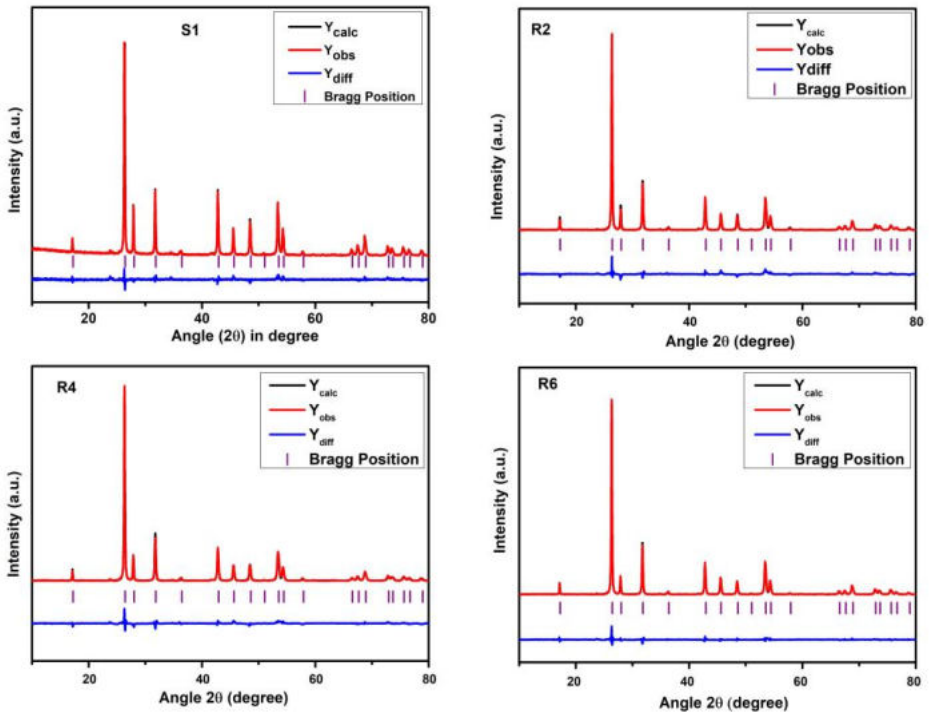

Figure 6.3 Observed, calculated and the difference XRD patterns of pristine and EB irradiated $BaWO_4$ samples

Table 6.2 Structural parameters and refined data of pristine and EB irradiated $BaWO_4$ samples

Sample	Atoms	x	y	z	a=b (Å)	c (Å)	Unit cell volume (Å^3)	R_{wp}	R_p	R_e	GOF
S1	Ba	0.0000	0.2500	0.6250	5.621	12.741	402.62	9.71	7.38	6.66	1.45
	W	0.0000	0.2500	0.1250							
	O	0.1259	0.0056	0.2097							
R2	Ba	0.0000	0.2500	0.6250	5.626	12.738	403.18	9.82	6.89	6.85	1.43
	W	0.0000	0.2500	0.1250							
	O	0.1239	0.0138	0.2075							
R4	Ba	0.0000	0.2500	0.6250	5.628	12.745	403.69	10.31	7.34	8.13	1.27
	W	0.0000	0.2500	0.1250							
	O	0.1160	0.0120	0.2188							
R6	Ba	0.0000	0.2500	0.6250	5.630	12.740	403.82	8.63	5.68	7.30	1.18
	W	0.0000	0.2500	0.1250							
	O	0.1263	0.0000	0.2080							

6.3.1.2 SEM Analysis

Figure 6.4 shows the SEM images of the pristine and EB irradiated $BaWO_4$ samples. The surface morphology of the samples is unveiled by the SEM micrographs.

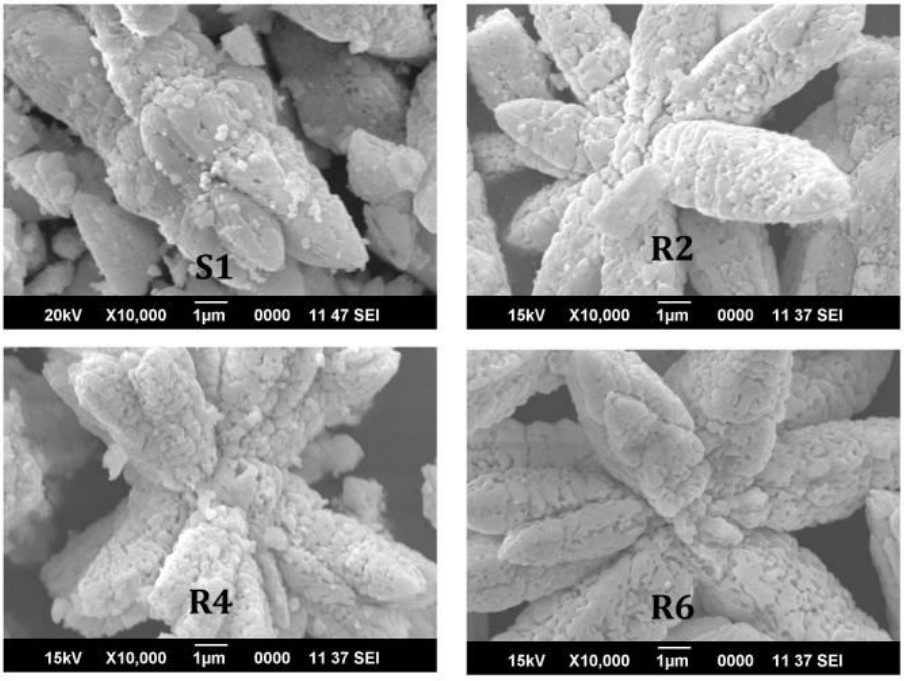

Figure 6.4 SEM images of pristine and EB irradiated $BaWO_4$ samples

As reported in the literature, scheelite type structures have many faces and they will undergo docking process with faces of lower surface energy and hence generate an extended morphology [10]. These extended morphologies are derived by oriented nanoparticles and are formed like a peanuts structure in a few micrometres (Sample **S1**). These peanut-shaped particles are joined together to form flower-like structures upon electron beam irradiation (Sample **R2** - **R6**). On beam irradiation, point defects are created within the particles and this will

annihilate at the particle surface due to the high energy collision. This can drastically alter the shape of the individual particles causing agglomeration of closely spaced particle groupings [11].

The surface morphology confirms the porous nature of the samples. The SEM micrographs demonstrate that the pores are mesoporous and distributed in an irregular manner, which is mainly due to the inter-particle separation [9]. The mesoporous materials have important applications in optics, catalysis, drug delivery systems, energy storage, sensors, coatings, cosmetics, bio-separation, diagnostics, gas-separation, and nanotechnology because of their narrow pore size distributions and high surface area [12].

6.3.1.3 FTIR Analysis

The FTIR spectra of $BaWO_4$ samples **S1**, **R2, R4,** and **R6** are recorded in the transmittance mode and are depicted in Figure 6.5. As $BaWO_4$ has tetrahedral symmetry, only F2(ν3, ν4) modes are infrared active. The intense peak at 820 cm^{-1} is due to the anti-symmetric stretching vibration F2(ν3) of the W-O bond in the WO_4^{2-} tetrahedron [13]. It is interesting that this peak becomes broader in irradiated samples. This broadening of the peak might occur due to the increase in strain caused by the EB irradiation.

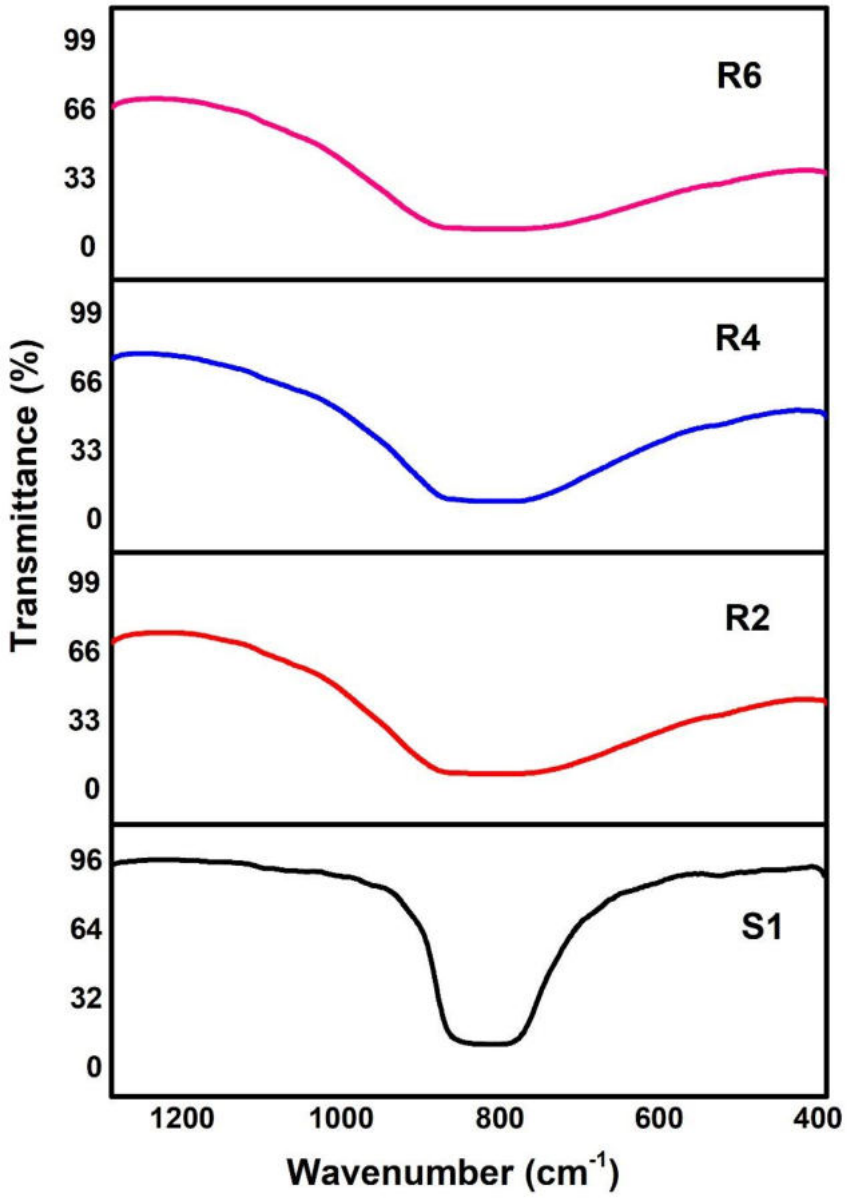

Figure 6.5 FTIR spectra of pristine and EB irradiated $BaWO_4$ samples

6.3.1.4 Raman Analysis

Raman spectra of the pristine and EB irradiated $BaWO_4$ samples are depicted in Figure 6.6. The theoretical and experimental Raman modes of $BaWO_4$ samples are presented in Table 6.3. The details of the Raman modes of scheelite tetragonal $BaWO_4$ are given in *Section 3.3.2.5*. The EB irradiated $BaWO_4$ samples **R4** and **R6** contain all the 13 Raman modes (Figure 6.6 and Table 6.3). Figure 6.6 confirms that the Raman bands of $BaWO_4$ nanoparticles samples are sharp and well defined because of the structure and electronic band structure properties of $BaWO_4$ crystals [14].

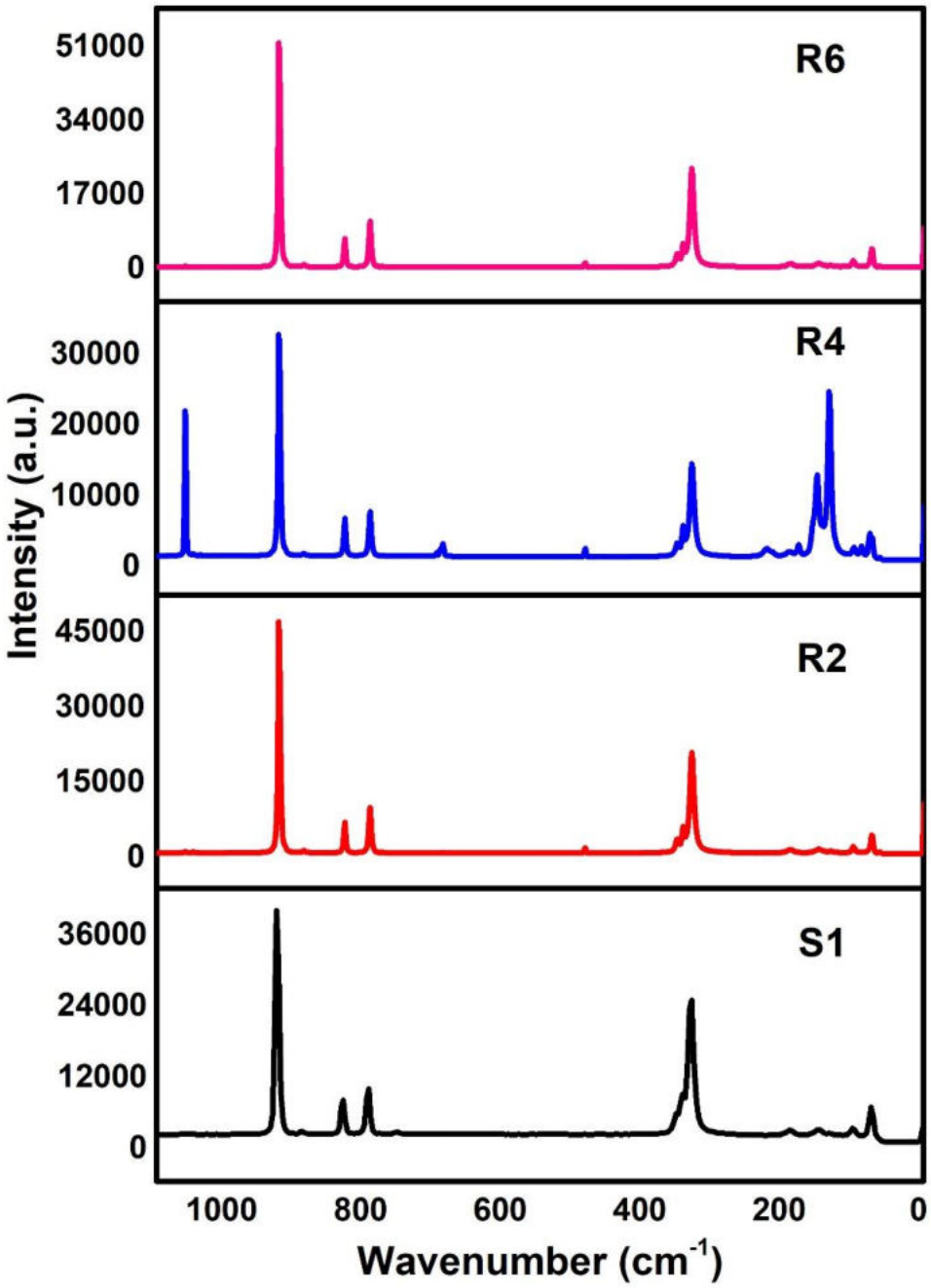

Figure 6.6 Raman spectra of pristine and EB irradiated $BaWO_4$ samples

Table 6.3 Raman active modes of pristine and EB irradiated $BaWO_4$ samples

Peak/mode	Value of ω in cm^{-1}				
	Theoretical [15]	Present values			
		S1	**R2**	**R4**	**R6**
T(Bg)	55	-	-	62.583	61.02
T(Eg)	81	75.56	75.04	76.86	74.26
T(Eg)	110	101.73	100.49	99.97	100.49
T(Bg)	145	-	-	135.81	132.95
R(Ag)	149	151.65	151.65	152.95	149
R(Eg)	209	191.91	191.91	191.91	191.91
ν2(Ag)	328	332.65	333.95	332.65	332.66
ν2(Bg)	329	332.65	332.65	332.65	332.65
ν4((Bg)	339	345.38	344.08	344.08	345.38
ν4(Eg)	348	354.21	353.94	353.94	353.94
ν3(Eg)	797	796.45	793.59	793.59	793.59
ν3(Bg)	823	832.54	829.69	829.69	829.69
ν1(Ag)	928	927.33	924.77	924.48	924.48

In the Raman modes, ν_1, ν_2, ν_3, and ν_4 represent the internal mode of vibrations, T and R represent the translational and rotational mode of vibrations respectively. It can be seen that the vibrations ν_1, ν_3, and ν_4 are red-shifted towards the shorter wavenumber side upon EB irradiation. As a result, the W-O bond undergoes a tensile strain [16] under beam irradiation, and hence the bond length may increase. The internal modes depend on lattice constants while the external modes depend on the cationic mass [17]. The translational modes [T(Bg)] are not observed in samples **S1** and **R2**, but they are visible in samples **R4** and **R6** due to the strain caused by EB irradiation of higher doses [18]. The strain is more for

sample **R4** as the intensity for translational modes is maximum for **R4**. The additional peak found at 891 cm^{-1} is due to the symmetric stretching vibration of the short W-O bond in the WO_2 group [19]. The peak at 891 cm^{-1} is also red shifted upon beam irradiation. New peaks are observed at 88, 178.9, 688, and 1056 cm^{-1} for the sample **R4**, which has the maximum crystallite size and unit cell volume. Ba^{2+} ion vacancy created during the electron beam irradiation of 4 kGy doses may be the reason for the formation of new peaks. In this case, two oxygen atoms may share a hole and becomes O_2^{3-} [20]. The vibrational mode at 1056 cm^{-1} corresponds to the O-O stretching vibration [21], and an irregular variation is observed in the external mode of vibration. These results confirm some significant strain or structural changes upon EB irradiation on $BaWO_4$ samples. Moreover, all the structural studies illustrate that EB irradiation results in structural modification for $BaWO_4$ nanoparticles, and is dose depended.

6.3.2 Optical Properties

UV-visible absorption spectroscopy and photoluminescence spectroscopy are the techniques used to explore the optical properties of the EB irradiated $BaWO_4$ samples. Optical analyses are carried out by following the procedure given in *Section 2.5.*

6.3.2.1 UV-visible Analysis

The optical absorption spectra of the pristine and EB irradiated $BaWO_4$ samples show that optical absorption is in the ultraviolet region (Figure 6.7). The optical absorption coefficients of the samples are obtained from the diffuse reflectance spectra by using the Kubelka-Munk transformation equation as described in *Section 2.5*. The optical absorption peaks corresponding to the ligand to metal charge transfer transition inside the WO_4^{2-} anion [22] of the samples **S1**,

R2, **R4,** and **R6** are at 220, 218, 216, and 219 nm respectively, which are close to the reported value (223 nm) [23]. In Figure 6.7, the optical absorption band is slightly blue-shifted for the irradiated samples, and the shift is more for the sample **R4**. The slight shift in absorption peak may be due to the distortions produced in the WO_4 tetrahedral structure upon EB irradiation [24].

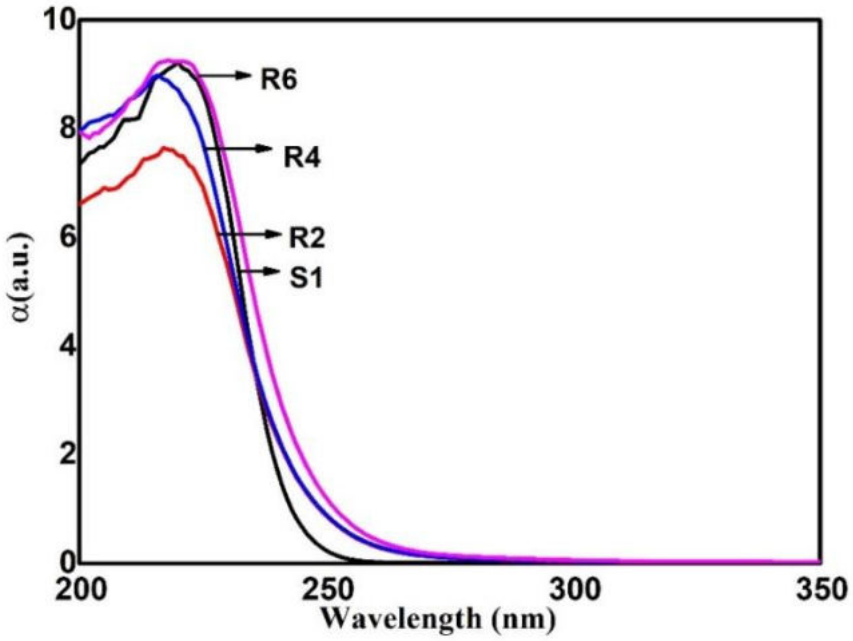

Figure 6.7 Optical absorption spectra of pristine and EB irradiated $BaWO_4$ samples

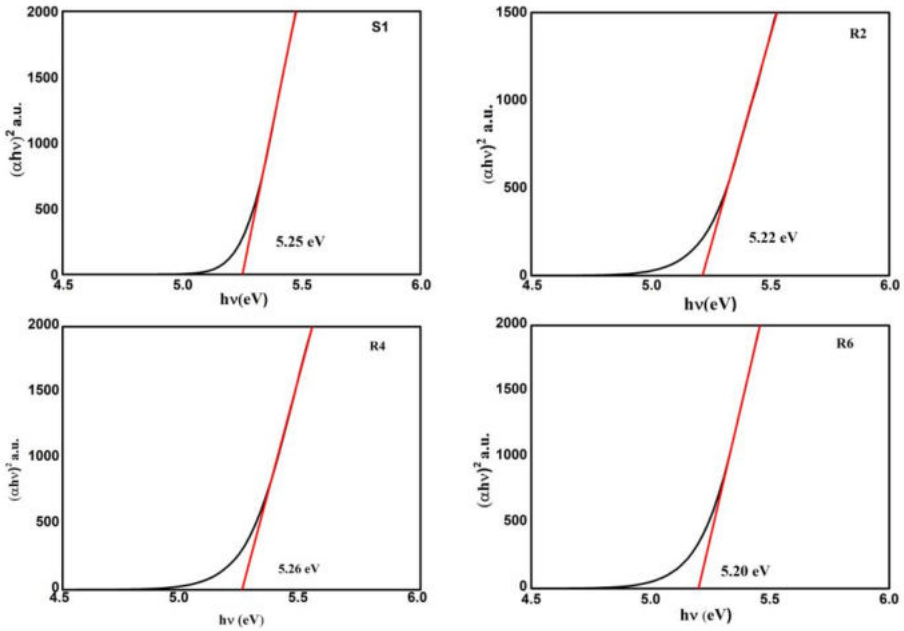

Figure 6.8 Tauc plots of pristine and EB irradiated $BaWO_4$ samples

The optical bandgap of the pristine and EB irradiated $BaWO_4$ samples are estimated by using the Tauc relation. Tauc plots, $(\alpha h\nu)^2$ *vs.* $h\nu$ of the $BaWO_4$ samples are depicted in Figure 6.8. The measured bandgap values are 5.25, 5.22, 5.26 and 5.20 eV for the samples **S1**, **R2**, **R4**, and **R6** respectively. Thus, the EB irradiation results in slight changes in optical bandgap values of $BaWO_4$. The results show that the optical bandgap is larger for sample **R4**, which is due to the presence of the V_F colour centre [20].

6.3.2.2 Photoluminescence Studies

Room temperature PL spectra of the EB irradiated $BaWO_4$ samples at an excitation wavelength of 350 nm are shown in Figure 6.9.

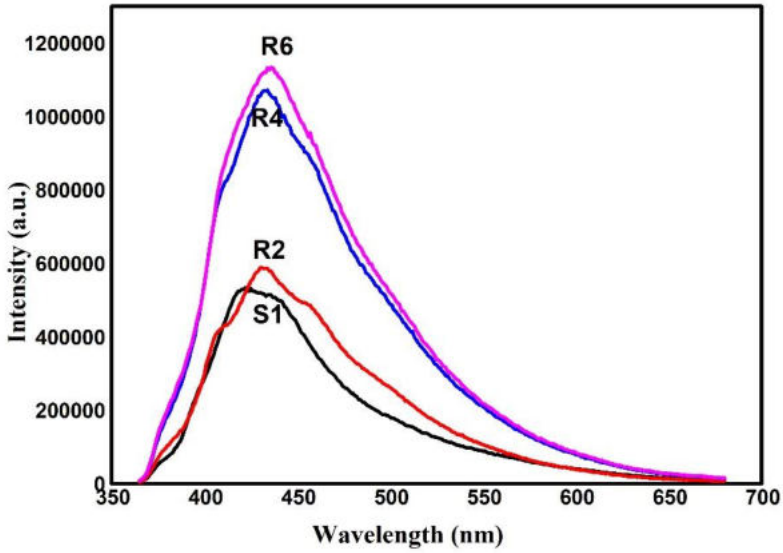

Figure 6.9 PL spectra of pristine and EB irradiated $BaWO_4$ samples

A broad emission band is observed around 430 nm, indicating that the relaxation occurs by various paths, involving the participation of numerous states (multiphonon process) [25]. PL emission is a measure of the recombination rate of photogenerated electron-hole pairs. The blue luminescence in $BaWO_4$ is due to the radiative transition of self-trapped excitons within the $(WO_4)^{2-}$ group [26]. In Figure 6.9, the intensity of PL emission is dose dependent and is more for irradiated samples **R4** and **R6**. Besides, the PL spectra of electron irradiated samples of $BaWO_4$ are broadened, and the peaks are red-shifted. The emission peaks of samples **S1**, **R2**, **R4** and **R6** are 421, 431, 432 and 434 nm respectively. The increase in PL emission of the EB irradiated samples is related to the

structural defects caused by the distortions formed into the [WO_4] tetrahedron groups upon EB irradiation [27]. Hence, photoluminescence emission properties of the $BaWO_4$ nanoparticles can be tuned by EB irradiation. Moreover, the enhanced PL properties of the EB irradiated $BaWO_4$ phosphors can be used for optoelectronics applications.

The CIE chromaticity coordinates of the pure and EB irradiated $BaWO_4$ samples at an excitation of 350 nm are given in Table 6.4. The CIE chromaticity diagram and phosphor triangle for the pristine and EB irradiated $BaWO_4$ samples are depicted in Figure 6.10. The figure demonstrates that chromaticity coordinates are nearer to the edge of the phosphor triangle and the emission is blue. The purity of the blue emission is good for the irradiated sample **R2** (2 kGy). It can be seen that there are only slight changes for the chromaticity coordinates for $BaWO_4$ samples by EB irradiation. In short, the results of the PL and CIE chromaticity studies suggest that EB irradiation of suitable dose can be used to improve PL intensity of $BaWO_4$ phosphors for blue light emission.

Table 6.4 CIE chromaticity coordinates of pristine and EB irradiated $BaWO_4$ samples

Sample	CIE coordinates	
	x	y
S1	0.0191	0.1813
R2	0.1807	0.1886
R4	0.1837	0.1938
R6	0.1832	0.1929

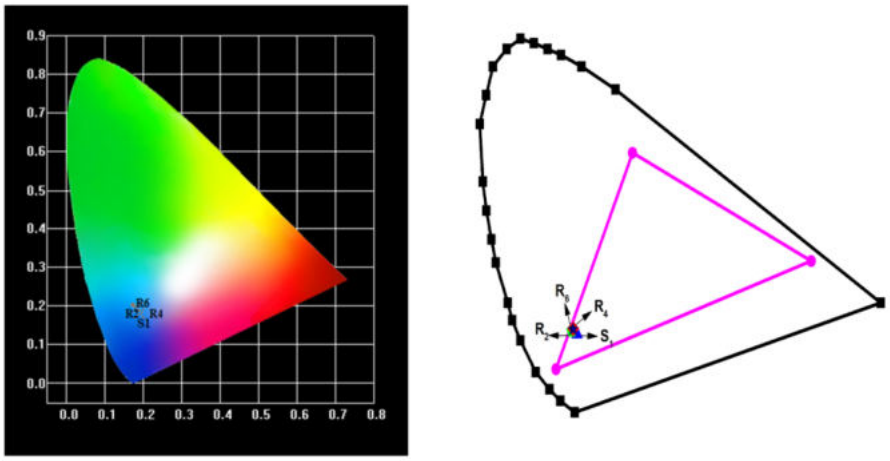

Figure 6.10 CIE chromaticity diagram and phosphor triangle of pristine and EB irradiated $BaWO_4$ samples

6.4 Conclusion

- A systematic study is conducted on the effect of EB irradiation on the structural and optical properties of nanocrystalline $BaWO_4$ synthesized by the chemical precipitation method.

- The results of structural studies indicated a pure scheelite-type tetragonal phase with space group $I4_1/a$ (88) and point group symmetry C_{4h}^6 for the pristine and EB irradiated $BaWO_4$ nanoparticles. The EB irradiation results in structural modification for $BaWO_4$ nanoparticles and is dose depended.
- SEM images revealed the change in surface morphology with EB irradiation. Peanut-shaped particles are joined together to form flower-like structures upon EB irradiation

- Slight changes in UV absorption and optical bandgap are observed on EB irradiation.
- An enhancement in PL emission intensity is observed on EB irradiated samples. PL and CIE chromaticity studies suggest that EB irradiation of suitable dose can be used to improve PL intensity of $BaWO_4$ phosphors for blue light emission.

References

[1] N. Aloysius Sabu, X. Francis, S. Ganesh, T. Varghese, Effect of 8 MeV electron beam irradiation on the structural, optical and electrical properties of a PANI-$MnWO_4$ nanocomposite, Eur. Phys. J. Plus. 134 (2019) 1–10.

[2] A. Sreedevi, K.P. Priyanka, K.K. Babitha, S. Ganesh, T. Varghese, Influence of electron beam irradiation on structural and optical properties of α-Ag_2WO_4 nanoparticles, Micron. 88 (2016) 1–6.

[3] K.P. Priyanka, N. Aloysius Sabu, A.T. Sunny, P.A. Sheena, T. Varghese, Effect of electron beam irradiation on optical properties of manganese tungstate nanoparticles, J. Nanotechnol. 2013 (2013) 1–7.

[4] K. Hareesh, G. Sanjeev, 8 MeV Electron induced changes in structural and thermal properties of Lexan Polycarbonate, Mater. Sci. Appl. 02 (2011) 1682–1687.

[5] K. Priya, G.K. Rao, V.K. Ashith, G. Sanjeev, V.P. Verma, V.C. Petwal, J. Dwivedi, The effect of 8 MeV electron beam irradiation on the structural, optical and photoluminescence properties of ZnS thin films, Ceram. Int. 45 (2019) 2576–2583.

[6] K.B. Sapnar, V.N. Bhoraskar, S.D. Dhole, Effects of 6 MeV electron irradiation on ZnO nanoparticles synthesized by microwave method, In proc. PAC 11, New York, USA (2011) 2166–2168.

[7] S. Chethan Pai, M.P. Joshi, S. Raj Mohan, T.S. Dhami, J. Khatei, K.S. Koteshwar Rao, L.M. Kukreja, G. Sanjeev, Effect of electron beam irradiation on photoluminescence properties of thioglycolic acid (TGA) capped CdTe nanoparticles, Adv. Mater. Lett. 4 (2013) 454–457.

[8] S. Kumar, K. Asokan, R.K. Singh, S. Chatterjee, D. Kanjilal, A.K. Ghosh, S. Kumar, K. Asokan, R.K. Singh, S. Chatterjee, D. Kanjilal, Structural and optical properties of ZnO and ZnO : Fe nanoparticles under dense electronic excitations J. Appl. Phys. 114 (2014) 164321-1–9.

[9] S.K. Stephen, S. Ganesh, T. Varghese, Modifications of structural and optical properties of nanophase $BaWO_4$ phosphors : Dose dependent effect of high energy electron beam irradiation, Radiat. Phys. Chem. 180 (2021) 109317 1–8.

[10] M. Longo, L. Gracia, D.G. Stroppa, S. Cavalcante, M. Orlandi, J. Ramirez, E.R. Leite, J. Andr, A. Beltr, A Joint Experimental and Theoretical Study on the Nanomorphology of $CaWO_4$ Crystals, The J. of Phys. Chem. C, (2011) 20113–20119.

[11] S. A. Briggs, K. Hattar, Evolution of Gold Nanoparticles in Radiation Environments, in: Gold Nanoparticles - Reach. New Height., (2019) 1–19.

[12] L. Wang, W. Ding, Y. Sun, The preparation and application of mesoporous materials for energy storage, Mater. Res. Bull. 83 (2016) 230-249.

[13] S. Vidya, S. Solomon, J.K. Thomas, Synthesis, characterization, and low temperature sintering of nanostructured $BaWO_4$ for optical and LTCC applications, Adv. Condens. Matter Phys. 2013 (2013) 1-11.

[14] M. Tyagi, S.G. Singh, A.K. Chauhan, S.C. Gadkari, First principles calculation of optical properties of $BaWO_4$: A study by full potential method, Phys. B Condens. Matter. 405 (2010) 4530–4535.

[15] F.J. Manjón, D. Errandonea, N. Garro, J. Pellicer-Porres, P. Rodríguez-Hernández, S. Radescu, J. López-Solano, A. Mujica, A. Muñoz, Lattice dynamics study of scheelite tungstates under high pressure I. $BaWO_4$, Phys. Rev. B - Condens. Matter Mater. Phys. 74 (2006) 1–17.

[16] S. Liang, M.N. Hasan, J.H. Seo, Direct observation of raman spectra in black phosphorus under uniaxial strain conditions, Nanomaterials. 9 (2019) 1–8.

[17] T.T. Basiev, A.A. Sobol, Y.K. Voronko, P.G. Zverev, Spontaneous Raman spectroscopy of tungstate and molybdate crystals for Raman lasers, Opt. Mater. (Amst). 15 (2000) 205–216.

[18] G. Kukucska, J. Koltai, Theoretical investigation of strain and doping on the Raman spectra of monolayer MoS_2, Phys. Status Solidi Basic Res. 254 (2017) 1–5.

[19] J. Anghel, A. Thurber, D.A. Tenne, C.B. Hanna, A. Punnoose, Correlation between saturation magnetization, bandgap, and lattice volume of transition metal (M= Cr, Mn, Fe, Co, or Ni) doped $Zn_{1-x}M_xO$ nanoparticles, J. Appl. Phys. 107 (2010) 09E314 1-3.

[20] H. Zhang, T. Liu, Q. Zhang, X. Wang, X. Guo, M. Song, J. Yin, First-principles study on electronic structures and absorption spectra for $BaWO_4$ crystal containing barium vacancy, Nucl. Instruments Methods Phys. Res. Sect. B Beam Interact. with Mater. Atoms. 267 (2009) 1056–1060.

[21] M. Tsubaki, N.T. Yu, Resonance Raman investigation of dioxygen bonding in oxycobaltmyoglobin and oxycobalthemoglobin: Structural implication of splittings of the bound O-O stretching vibration, Proc. Natl. Acad. Sci. U. S. A. 78 (1981) 3581–3585.

[22] S.M.M. Zawawi, R. Yahya, A. Hassan, H.N.M.E. Mahmud, M.N. Daud, Structural and optical characterization of metal tungstates (MWO_4; M=Ni, Ba, Bi) synthesized by a sucrose-templated method, Chem. Cent. J. 7 (2013) 1–10.

[23] M. Nikl, P. Bohacek, E. Mihokova, M. Kobayashi, M. Ishii, Y. Usuki, V. Babin, A. Stolovich, S. Zazubovich, M. Bacci, Excitonic emission of scheelite tungstates AWO_4 (A = Pb, Ca, Ba, Sr), J. Lumin. 87 (2000) 1136–1139.

[24] E.I. Ross-Medgaarden, I.E. Wachs, Structural determination of bulk and surface tungsten oxides with UV-vis diffuse reflectance spectroscopy and raman spectroscopy, J. Phys. Chem. C. 111 (2007) 15089–15099.

[25] G.K. Sahu, S. Behera, Investigation of optical and structural properties of scheelite-type barium tungstate ceramic, Int. J. Manag. Technol. Eng. 8 (2018) 2314–2320.

[26] G. Blasse, Classical phosphors: A Pandora's box, J. Lumin. 72–74 (1997) 129–134.

[27] L.S. Cavalcante, J.C. Sczancoski, J.W.M. Espinosa, J.A. Varela, P.S. Pizani, E. Longo, Photoluminescent behavior of $BaWO_4$ powders processed in microwave-hydrothermal, J. Alloys Compd. 474 (2009) 195–200.

Chapter 7

SUMMARY AND SCOPE FOR FUTURE WORK

This chapter provides a brief summary of the observations made during the investigation and scope for future work. The significant results of the investigation are also highlighted in this chapter.

The present study describes the synthesis and characterization of nanocrystalline $BaWO_4$. The effects of calcination temperature, the influence of dopants Cu and Yb and the impact of 8 MeV electron beam irradiation on the properties of nanocrystalline $BaWO_4$ are discussed in various chapters. The research work is systematically presented in six chapters. The structure and fundamental properties of $BaWO_4$, and a brief review on the synthesis and properties of pristine and doped $BaWO_4$ are presented in Chapter 1. Chapter 2 deals with a brief description of various characterization techniques used for the characterization of the prepared samples. The effect of calcination temperature on structural, optical, magnetic and electrical properties of nanocrystalline $BaWO_4$ are described in Chapter 3. The modifications of the structural, optical, and magnetic properties of the $BaWO_4$ samples due to Cu and Yb doping are elucidated in Chapter 4 and 5, respectively. Chapter 6 gives a detailed discussion

of the impact of 8 MeV electron beam irradiation on the structural and optical properties of nanocrystalline $BaWO_4$.

A summary of the synthesis and characterization of $BaWO_4$ nanocrystals, and Cu and Yb doped $BaWO_4$ and the impact of high energy electron beam irradiation on the properties of $BaWO_4$ are presented in the current chapter. The important outcomes and the scope for future work are also mentioned in this concluding chapter.

7.1 Summary of the Present Work

Nanocrystalline $BaWO_4$ powder samples are successfully synthesized by the chemical precipitation method. The effects of calcination temperature on the structural, optical, magnetic and electrical properties of the synthesized $BaWO_4$ samples are studied. The average crystallite size of the $BaWO_4$ nanoparticles is found to increase with the increase in calcination temperature. The surface morphology of the samples is found to vary with change in calcination temperature. The structural characterization, such as XRD, FTIR, and Raman analyses, confirm the scheelite tetragonal nature of the calcined samples of $BaWO_4$ with a space group $I4_1/a$. The Rietveld, analyses validated the scheelite tetragonal structure. The SEM images of the $BaWO_4$ samples show changes in the microstructure, granular to flower like structure, with the increase in calcination temperature. The average particle sizes and spherical shape of the nanoparticles are obtained from the TEM images of the $BaWO_4$ samples.

The samples show an absorption spectrum in the ultraviolet region. The optical bandgap of the $BaWO_4$ samples is found to decrease with an increase in calcination temperature. A broad photoluminescence emission spectrum is obtained, and the intensity of emission is found to increase with calcination

temperature. The chromaticity coordinates of the calcined samples of $BaWO_4$ indicate unique blue emission with varying intensity. This property of the nanomaterials can be used for the construction of NUV light excited blue LEDs. The ferromagnetic nature of the $BaWO_4$ sample is revealed from VSM measurements. The VSM results confirm that the magnetic properties such as ferromagnetic behaviour, saturation magnetization and the coercivity of $BaWO_4$ nanoparticles varies with the increase in calcination temperature. A slight variation in the dielectric constant is observed with the calcination temperature. The high and steady value of ε' of $BaWO_4$ sample calcined at 700 °C makes it suitable for dielectric layer in field-effect transistors. In addition, the low and steady value of dissipation factor, and an almost steady value of dielectric constant of $BaWO_4$ samples over a wide range of frequencies suggest their suitability in LTCC applications. At low frequencies, AC conductivity of $BaWO_4$ samples is very low and almost steady, and as the frequency increases the conductivity also increases obeying Jonscher's power law. In short, the dielectric properties and AC conductivity of $BaWO_4$ nanoparticles show a significant dependence on the calcination temperature.

Doping of a transition metal ion Cu^{2+} results in the modifications of structural, optical and magnetic properties of the $BaWO_4$ sample. Slight variations in structural parameters and average crystallite size are observed with the percentage increase of Cu in the sample. XRD, FTIR, and Raman analyses confirm the successful incorporation of Cu atoms into the $BaWO_4$ lattice. The surface morphology of the sample shows significant variations on Cu doping. TEM images reveal the reduction in particle size, and the highly polycrystalline nature of the Cu doped $BaWO_4$ sample. The absorption spectrum extends from UV to the visible region, and absorption in the visible region increases with the

concentration of Cu in the sample. The optical bandgap of the Cu doped $BaWO_4$ sample is found to slightly decrease with the increase in the percentage of Cu in the sample. The intensity of photoluminescence emission is found to decrease with the increase in doping concentration. Interestingly, the results of the optical studies confirm that the optical absorption and emission properties of the $BaWO_4$ nanoparticles can be tuned for potential applications by varying the percentage of Cu in the $BaWO_4$ sample. When doping of Cu increases to 5%, the size of the $BaWO_4$ nanoparticles reduces considerably. As a result, the magnetic property of the $BaWO_4$ nanoparticles changes from weak ferromagnetic to the superparamagnetic state. Hence, this material can be used to explore biomedical applications.

The rare earth ion Yb^{3+} doped $BaWO_4$ nanoparticles show variations in structural, optical and magnetic properties from the pristine $BaWO_4$ sample. The XRD, Rietveld, FTIR, and Raman analyses reveal the successful substitution of Yb^{3+} ions in the Ba^{2+} site. Slight variations in lattice parameters is observed due to the lattice distortions caused by the doping. Surface morphology of the $BaWO_4$ sample changes on doping. TEM images reveal the polycrystalline nature of the samples. The particle size is found to decrease considerably on Yb doping. UV visible absorption spectrum indicates a slight red shift in the absorption peak for the Yb doped samples. The absorption coefficient of the sample increases and the optical bandgap decreases with the concentration of the dopant. NIR photoluminescence emission in the range 900 −1090 nm is observed by exciting the sample with 275 nm. The broadening of the luminescence spectra is due to the stark splitting of the energy levels of Yb^{3+} ions. The emission intensity is found to increase with the percentage of Yb in the sample. NIR luminescence of the Yb doped $BaWO_4$ sample proposes its use in applications such as optical fiber

communication, efficient solar cells, bioanalyses, and bioimaging. An irregular variation in magnetic properties is observed for the Yb doped $BaWO_4$ samples. The 5% doped $BaWO_4$ sample does not exhibit any hysteresis showing superparamagnetic nature. In short, the magnetic properties of the Yb doped $BaWO_4$ nanoparticles strongly depend on the concentration of the Yb^{3+} ions.

The dose dependent effect of 8 MeV electron-beam irradiation on the structural and optical properties of the sample is studied. The structural studies such as XRD, SEM, FTIR and Raman analyses illustrate that EB irradiation results in structural modification for $BaWO_4$ nanoparticles and is dose depended. The SEM images confirm that surface morphology of the $BaWO_4$ sample is modified on EB irradiation. The irradiation of the electron beam also creates slight modifications in the optical bandgap of the $BaWO_4$ sample. The irradiated samples show a considerable increase in the PL emission intensity with the EB irradiation dose. The enhanced PL emission properties of the EB irradiated $BaWO_4$ nano-phosphors can be used for optoelectronics applications. In short, the electron beam irradiation technique can be used for the modifications of structural, optical absorption and PL emission properties of $BaWO_4$ nanoparticles for potential optoelectronics and biomedical applications.

7.2 Key Findings of the Study

The major outcomes of the present investigation are listed below.

- The $BaWO_4$ nanoparticles prepared by direct chemical precipitation route can be used as a potential candidate for solid state lighting applications such as, NUV light excited light emitting diodes and other optoelectronic devices.
- The structural, optical, magnetic and electrical properties of the $BaWO_4$ samples exhibit a significant dependence on the calcination temperature. The

Cu doping creates substantial modifications on the structural, optical and magnetic properties of $BaWO_4$ nanoparticles for various potential applications such as optoelectronics, biomedical and photocatalysis.

- The weak ferromagnetic behavior of $BaWO_4$ nanoparticles changes to superparamagnetic nature when doped with higher concentration of Cu (3 and 5%), which make them useful for various biomedical applications such as drug delivery, MRI contrast agents and biosensors

- The PL studies authenticate NIR emission for Yb doped $BaWO_4$ nanoparticles, the interaction of the $BaWO_4$ lattice with the Yb^{3+} ions, and the energy transfer between the tungstate group and the Yb^{3+} ions. This property of the Yb doped $BaWO_4$ nanomaterial can find its use in optical fiber communication, highly efficient solar cells, bioanalyses and bioimaging.

- The high energy electron beam irradiation of suitable dose can be used to make structural changes, and modifies optical absorption and emission properties of $BaWO_4$ nanocrystals for potential optoelectronics applications.

7.3 Scope for Future Work

The work presented in this dissertation can be extended in several directions and are briefly presented as follows:

- Phtocatalytic potential of $BaWO_4$ nanoparticles could be explored for pristine and doped samples. The porous nature of the $BaWO_4$ material could be used to investigate useful application of the sample in a new regime.
- More investigations could be needed in the Yb doped $BaWO_4$ sample to increase the efficiency of NIR luminescence.

- White light luminescence for $BaWO_4$ could be achieved by doping and co-doping with rare-earth ions.
- Up conversion lasers could be achieved by selecting suitable rare-earth co-dopants for $BaWO_4$.
- The dielectric study could be extended to the doped samples to find potential electronics applications.